Society for Science and Education
United Kingdom

ISSN: 2055 - 1266
Volume 3 No 1
February 2016

Journal of Biomedical Engineering and Medical Imaging

TABLE OF CONTENTS

EDITORIAL ADVISORY BOARD

DISCLAIMER

All the contributions are published in good faith and intentions to promote and encourage research activities around the globe. The contributions are property of their respective authors/owners and the journal is not responsible for any content that hurts someone's views or feelings etc.

SOCIETY FOR SCIENCE AND EDUCATION UNITED KINGDOM

JBEMi JOURNAL OF BIOMEDICAL ENGINEERING AND MEDICAL IMAGING

ISSN: 2055-1266
VOLUME 3 ISSUE 1

Multiple Hand Gesture Recognition using Surface EMG Signals

Nazo Haroon[1]and Anjum Naeem Malik[2]
National University of Sciences & Technology, Islamabad, Pakistan.
[1]nazoharoon78@mts.ceme.edu.pk; [2]anjum.naeem78@mts.ceme.edu.pk

ABSTRACT

Significance of robotics in serving the human being is increasing day by day. A large number of impairments and disabilities in human body force the researchers to think on the necessity of simple and natural human-machine control interface. The idea of the project is the acquisition of SEMG (Surface Electromyographic) signals from the forearm and to recognize the various hand gestures. The resulting classification is then used to control a two degree of freedom (DOF) robotic gripper.

Muscular activity is sensed by placing the EMG sensors/electrodes on the skin. The acquired signal from these electrodes is very small in amplitude and corrupted by different artifacts due to positioning and pasting of electrodes, transmission line and crosstalk with other biological signals. Pre-amplification is required to boost up the signal and then filtration is required to get the desired usable band of frequency. After that artifact-free EMG signal is further amplified, which can be fed to the control circuitry (microcontroller) to control the Hobby Servo motor of the robotic gripper hand. All the process is implemented for the real time scenario.

Keywords: Human-machine control interface, SEMG (Surface Electromyographic) signals, classification, degree of freedom (DOF), crosstalk biological signals.

1 Introduction

Electromyographic (EMG) signals provide a very useful means of control of robotic prosthetics. Research in the field of biomedical engineering, wearable robotics supported by electro mechanics, has led to the creation of advanced and accurate active prosthetics. The foremost problem encountered while dealing with physiological signals is isolating the desired signal from that of its like counterparts. When measuring motor unit action potentials, it can be hard to assure that the acquired signal is that of the muscle under examination [3].

Once obtained the EMG signal can be used for several applications. In applications such as determining muscle fatigue, the frequency spectrum of the signal possesses the desired information, whereas, for control applications the overall energy of the signal provides the preferred control parameter. The goal for this paper is to use EMG signals obtained from the forearm to control a mechanical gripper which not only focus on obtaining an accurate signal from the muscle, but also creating an easily controllable servo mechanism that will provide user feedback. For gripping tasks, a drawback for the user can be

DOI: 10.14738/jbemi.31.1738
Publication Date: 11th January 2016
URL: http://dx.doi.org/10.14738/jbemi. 31.1738

their inability to identify grip strength. The goal of this paper is to provide the user with a vibration sensation to indicate gripper strength, while allowing the user to vary this strength accordingly [1] & [2].

The objectives of this paper are to give the user motor control and sensory feedback information using a simple non-invasive interface method. A non-invasive method allows the user to wear the bionic hand only when they feel it's appropriate. The ease of use comes with the control system we have used, that how to control robotic gripper. Flexion and extension of the users' muscles must be recorded and sent to the electrical system which gives the output and direction on how to flex or extend the mechanical joints to the specified hand position. The last objective of this paper is to develop some sensory feedback to the user so that they have an idea of how much pressure the hand is on an object.

It is important for a user to have this sensory information because it allows them to go beyond simple interaction with the physical world, but to understand their own interaction and the ability to make adjustments. The Objectives for the paper are defined as the ability to control the robotic gripper using electromyography, the ability of the robotic hand to perform up to a maximum of five hand positions that will assist the user in easing daily actions and the ability to display sensory feedback information to the user. The bock diagram is shown in figure 1.

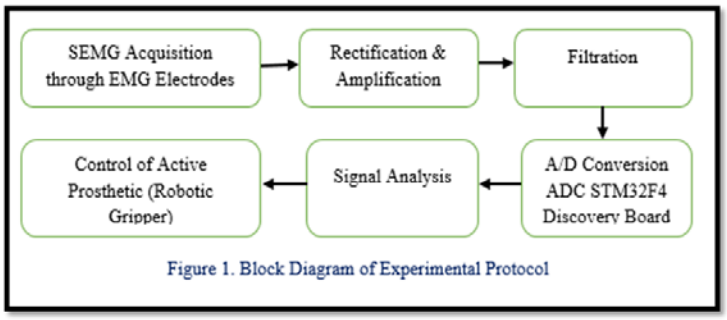

Figure 1. Block Diagram and Experimental Protocol

First of all muscular activity is sensed by placing the EMG sensors/electrodes on the skin [4]. The acquired signal from these electrodes is very small in amplitude and corrupted by different artifacts. Pre-amplification is required to boost up the signal and then filtration is required to get the desired usable band of frequency. After doing all this, the artifact-free EMG signal is further amplified up to some volts which is fed to STM32F4 discovery board to control the Hobby Servo motor of the robotic hand gripper for practicing different hand gestures. Different gestures are as shown in figure 2. The STM32F4 discovery board is based on the high-performance ARM® Cortex™-M4 32-bit RISC core operating at a frequency of up to 168 MHz The Cortex-M4 core features a Floating point unit (FPU) single precision which supports all ARM single precision data-processing instructions and data types [11].

Figure 2. Different Hand Gestures

2 Surface EMG Signal Detection and Pre Amplification Circuitry

The EMG signal is the electrical manifestation of the neuromuscular activation which represents the current generated by the ionic flow across the membrane of the muscle fibers that propagates through the intervening tissues to reach the detection surface of an electrode located in the environment. The EMG measures the amount of electrical discharge in the muscle fibers and therefore it quantifies muscle contraction and relaxation. This electrical discharge is translated into auditory and visual displays and the person can begin to notice and bring about changes in muscle tension which he/she was previously unable to do. An EMG is the summation of action potentials from the muscle fibers under the electrodes placed on the skin [5] & [1].

The EMG signal is recorded by using an electrode placed on the muscle. The quality of an EMG signal measurement strongly depends on a proper skin preparation and electrode positioning. This is needed to improve the adhesion of the electrodes, especially under humid conditions or for sweaty skin types and/or dynamic movement conditions. Special abrasive and conductive cleaning pastes/gels are available which remove dead skin cells and clean the skin from dirt and sweat. The electrodes we have used are pre gelled surface electrodes.

2.1 Pre Amplification and Body Reference Circuit

Since the EMG signal is low in amplitude with respect to other ambient signals on the surface of the skin, it is necessary and convenient to detect it with a differential configuration. That is, two detection surfaces are used and the two detected signals are subtracted prior to being amplified. In this differential configuration, the shape and area of the detection surfaces and the distance between the detection surfaces are important factors because they affect the amplitude and the frequency content of the signal. That is why two channel data is acquired.

The differential arrangement acts as a comb band-pass filter to the electrical signal seen by the detection surfaces. (In actuality, if the inter-detection surface spacing is set so as not to alias the EMG signal, the spectrum of the EMG signal should fit in the low end of the band-pass filter. Thus for practical purposes, the differential electrode behaves as a high-pass filter.) The distribution of the frequencies in the spectrum as well as the bandwidth is affected by the distance between the detection surfaces [].

At least one neutral reference electrode per subject has to be positioned. Typically an electrically unaffected but nearby area is selected, such as joints, bony area, frontal head etc. we did prepare the skin for the reference electrode too and use electrode diameters of at least 1 cm. The EMG signal is recorded by using an electrode placed on the muscle. The electrical activity measured by each muscle electrode and the ground electrode are sent to an amplifier. The pre amplifier circuitry is as follows.

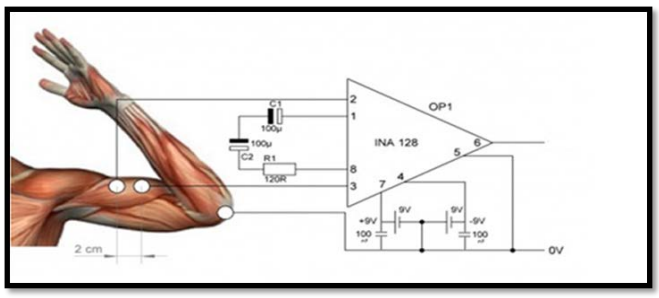

Figure 3. Pre Amplification and Body Reference Circuitry for surface EMG Signal

As explained earlier, EMG signal is so small that it is not suitable for further processing. While the amplitude of the signal is between 0 to 10 millivolts (peak-to-peak), or 0 to 1.5 millivolts (rms), the usable frequency of an EMG signal is ranging between 0-500 Hz. At this state, we need a huge gain to boost the EMG signal without changing phase or frequency of the signal so the gain is set to 500. To get the right level of the input signal, we need a body reference circuit which works as a feedback from the inputs. Whenever the body temperature changes or signal changes due to noise introduced by the body, this body reference will help in maintaining the correct level of signal. In each input channel, there is one body reference feedback [9] & [10].

The amplifier eliminates random voltages caused by electrical noise by subtracting the signal from the ground electrode from the muscle electrode, producing the raw EMG. Noise is being eliminated in LabVIEW software by using moving average filter [5] & [6] and finally a noise free signal is obtained. This can be made pretty clear by seeing the difference between Raw and Filtered EMG signal of open and close gesture as well as wrist movement gesture respectively in the figures shown below.

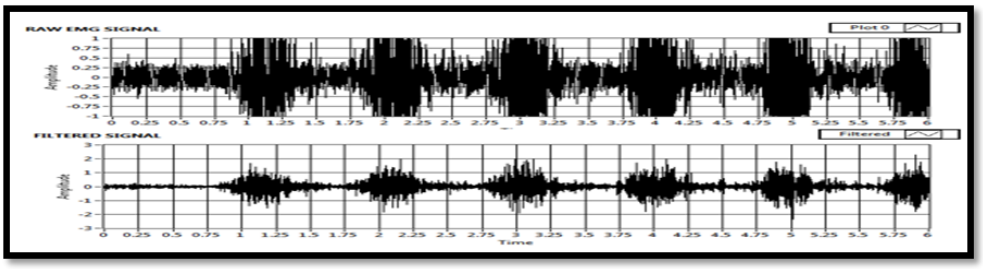

Figure 4. Samples of Hand Open and Close

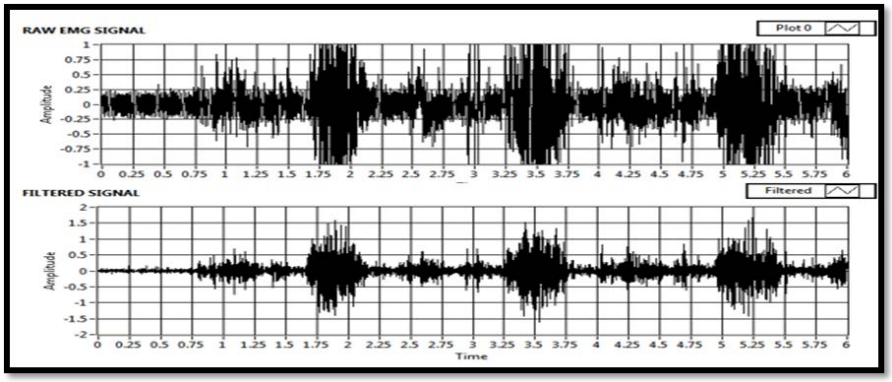

Figure 5. Samples of Wrist Movement

3 Filtration and Rectification

The high pass filter is applied at the Gain resister, so that they help to prevent noise that has been amplified by the amplifier. The filter also helped to sink any DC current that could cause bias for the signal. As described earlier, the usable frequency of the signal lies between 20 to 500Hertz. Majority is concentrated in 50 – 150 Hz. So, we used a High pass filter to remove the low frequency components in the signal and distortions occurred due to electricity wires and mobile phone signals that may affect our required signal.

In the amplifier section we have gain and bias adjustment circuit. The amplifier and bias adjustment provide an ability to adjust or correct the output signals in some circumstances. For example, the amplitude of amplified signal from the preamplifier is not high enough for the control circuitry or the amplified signal still has a bias or offset. Therefore, these problems can be resolved by using of the gain and bias adjustment.

There is a limitation of the gain and the bias adjustment. The amplifier in our EMG device can amplify about 1 to 1000 times. The bias adjustment can adjust the signal up or down by the level of positive nine volts, or negative nine volts. However, by the nature of op-amp, the output from the op-amp cannot be more or less than the power supply voltage. The output of the pre amplification and reference body circuit, for both channels goes to rectification circuit. Rectification is done to convert AC signal into a DC signal. Since the diode has unidirectional property hence suitable for rectifier. The schematic diagram for the rectification circuit made on Proteus Software can be seen in the figure below.

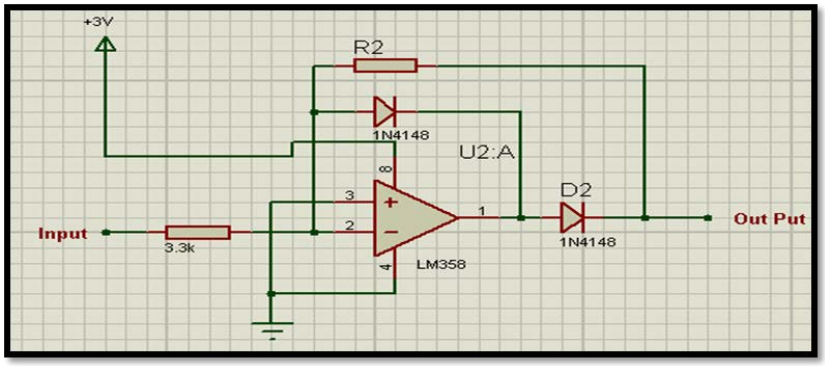

Figure 6. Schematic Diagram of Rectification Circuit

4 The Control Circuitry (Stm32F Discovery Board, Servo Motors and Robotic Gripper Interface)

After acquiring artifact free EMG signal next and most important part of this project is to make use of this signal to control the hobby servo motor of the robotic gripper hand. Servo motors have been around for a long time and are utilized in many applications. They are small in size but pack a big punch and are very energy efficient. These motors are capable of operating remote-controlled or radio-controlled toy cars, robots and airplanes. Servo motors are also used in industrial applications, robotics, in-line manufacturing, pharmaceutics and food services.

Our aim is to control the robotic gripper hand using the Stm32F407VG discovery board. By using the ADC module and controller of the discovery board we controlled the hobby servo motors to actuate the robotic gripper hand.

4.1 Analog to Digital Converter Module (ADC)

The 12-bit ADC is a successive approximation analog-to-digital converter. It has up to 19 multiplexed channels allowing it to measure signals from 16 external sources, two internal sources. The A/D conversion of the channels can be performed in single, continuous, scan or discontinuous mode. The result of the ADC is stored into a left or right-aligned 16-bit data register. The analog watchdog feature

allows the application to detect if the input voltage goes beyond the user-defined, higher or lower thresholds.

5 Experimental Setup and Results

Experimental setup mainly comprised of a circuit box consisting of pre amplification circuits for both surface EMG channels, rectification circuit, servo motors circuit and stm34F discover board interface and a robotic gripper. The complete experimental setup is as shown in the figure below.

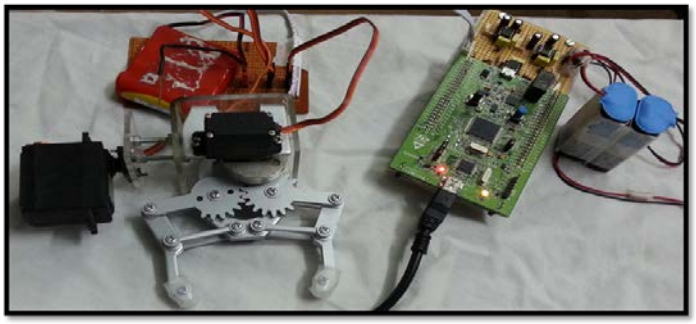

Figure 7. Experimental Setup

We have divided the main circuit in 5 sections. In the following circuit we have three connectors as mentioned in the figure a, b and c. First one “a” is for first channel labeled as section “2”. Second one “b” is for second channel labeled as section “3”. The section 1 is the button for ON/OFF purpose connected with the battery. Section 4 is the rectifier circuit. Section 5 is the STM32F4xx discovery board. Connector “C” is used to connect the Robotic Gripper with the Control circuitry.

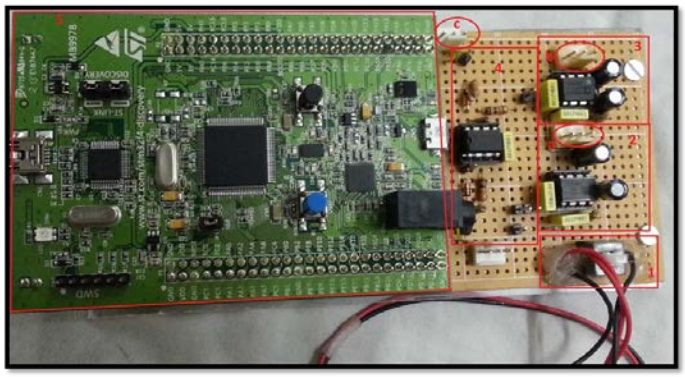

Figure 8. Labeled Sections of Experimental Setup

EMG signals have acquired from SEMG electrodes placed on the right arm of the test subject and it is instructed to perform the hand gestures without creating any flickering of eyes and other muscles contraction. Recorded EMG signals are fed directly to the filtration circuitry where all the undesirable artefacts are removed and signals are amplified according to the readable range of the controller. Once the signals are filtered they are fed to the analogue to digital conversion circuit where recorded continuous EMG signals are digitized and then digitized EMG signals are fed to the STM discovery board controller, where they are analyzed and recognized into multiple hand gesture classes and command signals are generated according to stratified classes to control the motors of robotic gripper [11].

Hand gestures we have detected are as follows and some of them can be seen in the figure below.

- Open
- Close
- Normal
- Normally Close
- Wrist downward movement

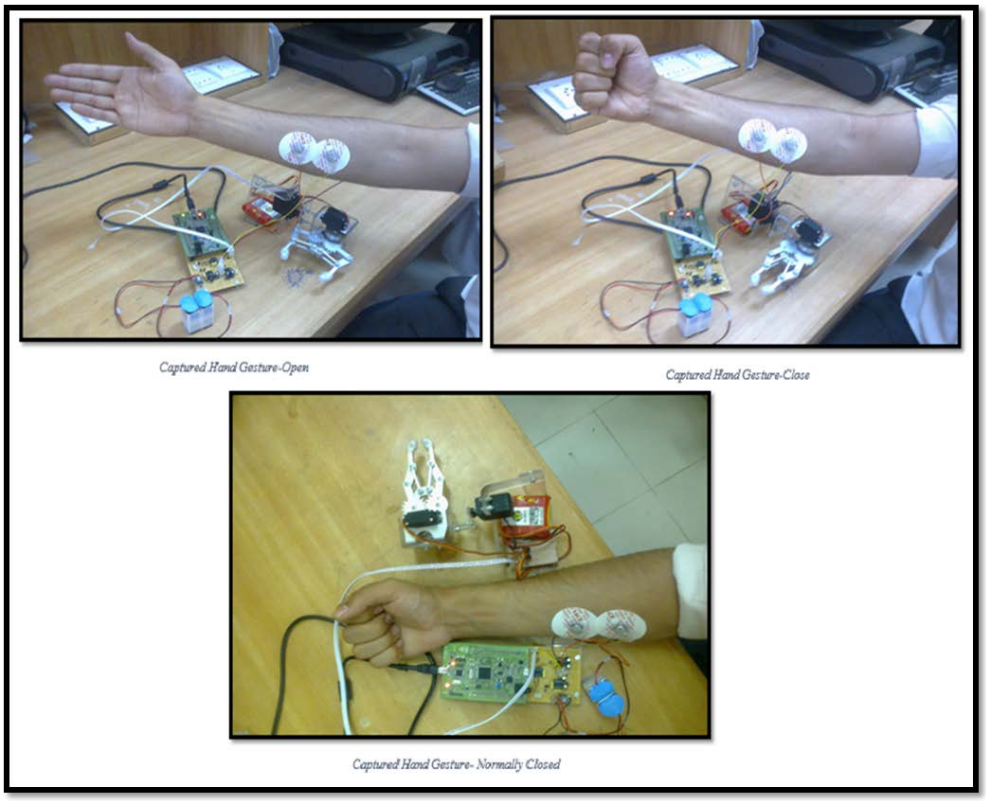

Figure 9. Results of different gestures detected

6 Conclusion

Electromyographic signal contains valuable information regarding the nervous system so the main objective of this study was to give a brief information about EMG signals acquisition, analysis and interfacing methodologies with exoskeleton/robotic gripper. This study clearly differentiated gestures of upper limb (open, close, normally close and wrist downward movement) and interfaced successfully with the robotic gripper using STM32F40xx discovery board controller. While implementing the hardware interface it has been observed that use of other reconfigurable devices like FPGA and PLDs will enhance the results in more efficient way. Future work will comprise of enhancing signal processing techniques and lower limb prosthetics interfacing with SEMG electrodes.

REFERENCES

[1] Shahid S. Higher Order Statistics Techniques Applied to EMG Signal Analysis and Characterization. Ph.D. thesis, University of Limerick; Ireland, 2004.

[2] Nikias CL, Raghuveer MR. Bispectrum estimation: A digital signal processing framework. IEEE Proceedings on Communications and Radar. 1987; 75 (7):869–891.

[3] Basmajian JV, de Luca CJ. Muscles Alive - The Functions Revealed by Electromyography. The Williams & Wilkins Company; Baltimore, 1985.

[4] Cram JR, Kasman GS, Holtz J. Introduction to Surface Electromyography. Aspen Publishers Inc.; Gaithersburg, Maryland, 1998.

[5] Thexton AJ. A randomization method for discriminating between signal and noise in recordings of rhythmic electromyographic activity. J Neurosci Meth. 1996; 66: 93 –98.

[6] Bornato P, de Alessio T, Knaflitz M. A statistical method for the measurement of the muscle activation intervals from surface myoelectric signal gait. IEEE Trans Biomed Eng.1998; 45: 287–299. doi: 10.1109/10.661154.

[7] Merlo A, Farina D. A Fast and Reliable Technique for Muscle Activity Detection from Surface EMG Signals. IEEE Trans Biomed Eng. 2003; 50 (3):316–323. Doi: 10.1109/TBME.2003.808829.

[8] Gabor D. Theory of communication. J Inst Elect Eng.1946; 93:429–457.

[9] Hefftner G, Zucchini W, Jaros G. The electromyogram (EMG) as a control signal for functional neuro-muscular stimulation part 1: Autoregressive modeling as a means of EMG signature discrimination. IEEE Trans Biomed Eng.1988; 35:230–237. doi: 10.1109/10.1370.

[10] Christodoulou CI, Pattichis CS. A new technique for the classification and decomposition of EMG signals. Proceedings in IEEE International Conference on Neural Networks.1995; 5:2303–2308.

[11] H. Arieta, R. Katoh, H. Yokoi, Y. Wenwei, 2006Development of a multi-DOF electromyography prosthetic system using the adaptive joint mechanism, ABBI 2006, 32110.

SOCIETY FOR SCIENCE AND EDUCATION UNITED KINGDOM

JBEMi JOURNAL OF BIOMEDICAL ENGINEERING AND MEDICAL IMAGING

ISSN: 2055-1266
VOLUME 3 ISSUE 1

Techniques for Detection and Analysis of Tumours from Brain MRI Images: A Review

Saurabh Shah[1] and N.C. Chauhan[2]

[1]*Department of Computer Science and Engineering, Babaria Institute of Technology, Vadodara and R.K. University, Rajkot, Gujarat, India.*

[2]*Department of Information Technology, A D Patel Institute of Technology, Anand, Gujarat, India.*

saurabh_er@rediffmail.com; narendracchauhan@gmail.com

ABSTRACT

Analysis of MRI images and extraction of brain tumours from MRI images are challenging tasks in medical image processing. Researchers have contributed in segmenting and analysing brain tumour by applying varieties of the techniques and different hybrid approaches, however, due to diversity in appearance of tumour from patient to patient and also due to different tumour types, it has still been a challenge to exactly and correctly identify tumours from brain MRI image. Analysing brain MR images manually for finding exact boundaries of tumour by physicians is very time consuming and challenging due to low contrast MRI image and similarities of intensities between brain tissues. Many semi-automated and automated approaches have been developed to analyse MRI images and to delineate desired regions, such as tissues and tumour, and analyse their properties. This paper presents a comprehensive review of the state of the art methods for analysis of MRI images and methods for detection tumour from it. The review focuses, specifically, on important phases of MRI image analysis like feature extraction, segmentation and classification techniques. The challenges while processing brain MRI images as well as merits and demerits of existing methods for tumour analysis have been discussed.

1 Introduction

Magnetic Resonance Imaging (MRI) has been widely used as one of popular imaging techniques to visualize tumour region by physicians as it gives high soft tissues contrast compared to other technique like Computed Tomography (CT), Positron Emission Tomography (PET) [1,**6**]. To study various properties of tumours, its presence and to correctly separate out tumour from other healthy tissues, multiple MRI sequences like T1-weighted, T1c-weighted, T2-weighted and FLAIR images are used where each sequence provides different information and helps to locate tumour, edema or necrotic regions [1].

Major tasks during analysis of brain MRI images are to study abnormalities in brain, to separate out healthy tissues of brain mainly into Grey Matter (GM), White Matter (WM) and Cerebro Spinal Fluid (CSF), to detect presence of tumour, necrotic region, edema or lesion and to study pathological area like

DOI: 10.14738/jbemi.31.1696
Publication Date: 14th January 2016
URL: http://dx.doi.org/10.14738/jbemi. 31.1696

cancer for diagnostic purpose [2,3]. It also includes finding size of tumour, location of tumour and different categories of tumours.

Brain tumours are mainly classified based its degree of aggression and location of origin. Tumours which originate from brain are called primary brain tumours while tumours which originate from other part of body are called metastatic brain tumours. As per guidelines of WHO, grading of brain tumour ranges from I(lowest) to IV(highest) based on aggression of tumour. Grade III and IV tumours are malignant and chances of survival are very less while grade I and II are semi-malignant and better prognosis is possible [1]. Gliomas are most common primary brain tumour seen in human brain. Brain tumours are of different types which are (1) Lymphoma (2) Gliomas (3) Meningioma (4) Medulloblastoma (5) Pituitary adenoma and (6) Craniopharyngioma [2]. Based on analysis of healthy tissues also relation with specific disease can be predicted. The analysis also helps in surgical planning, predicting growth of tumour and aggression of tumour.

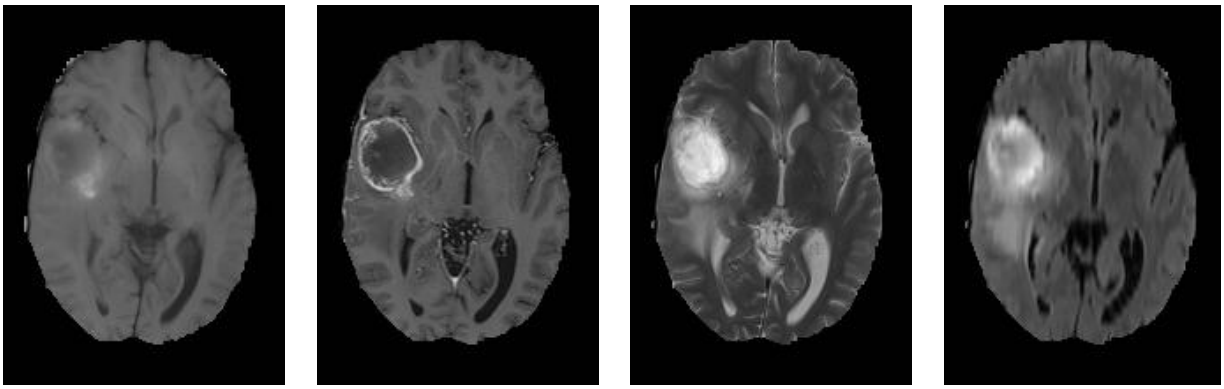

(a) (b) (c) (d)

Figure 1: (a) T1-weighted (b) T1- weighted with contrast enhanced (T1c) (c) T2- weighted and (d) FLAIR MRI real image sequence of brain of single person with high grade tumour collected from BRATS 2012 dataset [4]

Different MRI sequences have capability to separate different tissues which are generally highlighted in specific sequence based on tissue properties, e.g. T1-weighted image is good at separating healthy tissues in brain, T1c (Contrast enhanced with gadolinium-DTPA) helps in separating tumour boundaries which appear brighter because of contrasting agent, edema surrounded by tumour is detected well in T2-weighted images, while FLAIR images are best specifically in differentiating edema region from CSF [1,5]. Different sequences of brain MRI images of single patient are shown in Fig. 1 where we can notice different appearance of tissues in different sequences.

Brain tumour segmentations techniques mainly fall into three categories namely manual, semi automated and fully automated depending upon the human interaction required with the system. Various soft computing techniques have contributed a lot in the field of research for semi automated and fully automated segmentation of brain MRI images and many techniques have given promising solutions for image segmentation [3].

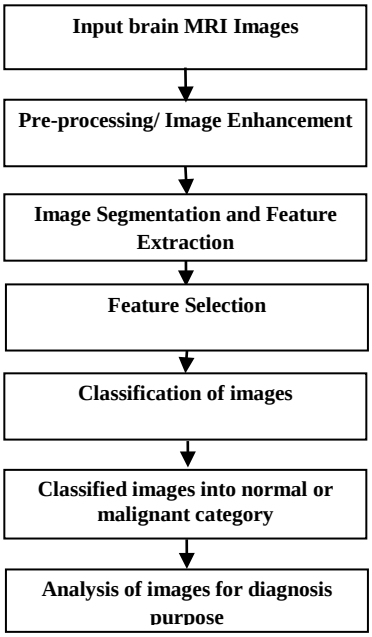

Figure 2: Block diagram of brain MRI image classification and analysis

Detection and correct segmentation of brain tumour is very difficult and challenging task due to low contrast image, unknown noise, unknown shape and size of tumour which varies from patient to patient, partial volume effect caused because of artefacts and uneven texture of tumours which appear differently for different patients [6].

Analysis of brain MRI images includes various phases as shown in Fig.2 where images are first pre-processed and enhanced mainly to remove noise, to normalize intensity values, to improve contrast and to extract brain from skull. Pre-processing helps in separating desired regions more accurately and also improves classification accuracy. After pre-processing, images are divided into homogeneous regions with similar properties called segmentation and features are extracted in feature extraction step. Most commonly seen Pattern Recognition problem in the domain of medical image analysis is finding discriminating features from a set of medical images and classifying them into set of classes. Feature extraction and feature selection plays very important role for detecting and classifying brain tumours [7]. Features are extracted mainly based on intensity values, texture properties, intensity gradients and edge detection.

Important features are selected in the feature selection phase by applying algorithms and based on these selected features, finally images are classified into various categories like normal or malignant by applying classifiers like SVM, ANN, kNN, Naïve Bayes and others which are discussed in subsequent sections.

This paper focuses on review of state of the art techniques from the literature which could be applied in each phase of brain MRI image analysis to achieve desired task. The paper is organized as follows. Section 2 presents review on pre-processing methods for enhancement of MRI images. Section 3 focuses on review of segmentation methods. Section 4 presents review of feature extraction and classification techniques. Section 5 concludes and summarizes the literature review.

2 Review of Pre-processing methods for enhancement of MRI images

MRI images are of poor quality [6, 8] for human visualization to understand finer details of tissue structures of brain. Also because of poor quality it is challenging to be processed by computational algorithms for further analysis. So, before algorithms are applied on images for further processing like segmentation or classification, images should be pre-processed and enhanced so as to improve segmentation and classification results. Researchers have proposed state of the art noise removal techniques which include linear and nonlinear filtering methods, wavelet based models, MRF (Markov Random Fields), NL-means (non-local means), anisotropic diffusion filtering and analytically correction schemes, and other advanced filters [2]. During noise removal it is very important to preserve edges and structure details without degrading image quality otherwise it degrades performance.

MRI images are of low contrast and many techniques are available that improve the contrast of the image and enhance the image that finally helps in improving visual appearance. Kharrat et. al. [8] presented mathematic morphology method for image enhancement which outperformed other well known methods like Contrast Limited Adaptive Histogram Equalization (CLAHE) and Beghdadi one. Anisotropic Wiener filter has shown good results in [9] for denoising as well as pre-processing of MRI images where it does not only reduce noise but also enhances image by preserving edges compared to other versions of wiener like isotropic and orientation where performance is measured not only in terms of MSE but also in terms of memory used, computational cost and performance. Basic wiener approach was similar to other popular wavelet based approaches as reported in literature but anisotropic property in wiener filter improved performance [9].

Gabor filters have been used for edge detection and texture based feature extraction but Veni et. al. [10] proposed Gabor filter based approach on Hexagonal Sampled Grids of x-ray images for image enhancement and obtained results of high quality in terms of the visualization of images and edges which were also well preserved. Best results obtained for texture images and approach found to be ideal for generating medical atlas from MRI images. Brain atlas reflects common anatomical map and structure of a brain which is prepared from different subjects before segmentation process is carried out. Atlas is used as prior knowledge and found to be useful when contrast between brain tissues is poor. So, to take advantage of atlas in segmentation, image is first registered with an atlas in a process called image registration [6].

Mainly for analysis of brain tissues from MRI images, non-brain region like skull is removed in pre-processing step. Chan-Vese algorithm of active contour used in [11] is known approach to separate brain region from skull by applying thresholding where threshold value is calculated based on intensity of skull region (non tissue) which is nearly zero and appears as black.

Techniques for segmentation of medical images are reviewed in the following section.

3 Review of Segmentation Methods for Brain MRI Images

Segmentation divides an image into set of segments or regions based on similar properties like similar intensity values, texture properties or based on given threshold values. Researchers have proposed many segmentation approaches which are generally classified as threshold-based, pixel classification based, region-based and model based techniques [3].

Many methods are proposed for segmentation of brain tumour which can be classified as (1) Machine learning and computational intelligent techniques like Artificial Neural Network (ANN), Fuzzy c-means (FCM), Support Vector Machine (SVM), k-Nearest Neighbour (kNN), Self-organizing map (SOM), k-means (2) Statistical models like Maximum Likelihood (ML), Gaussian Mixture Model (GMM), Expectation Maximization (EM) (3) Contour based techniques like active contours, deformable models, level set and (4) Thresholding, edge detection and region based techniques. Each category of methods has their own strength and weaknesses, hence proper selection of a method depends on background knowledge and suitable conditions to get best results from that method.

3.1 Machine learning and Computational intelligence based methods

From decades many methods are proposed by researchers for medical image analysis but with emergence of computational intelligence and machine learning methods in medical image processing, promising results have been obtained.

Gliomas tumour on the scale of grade IV are also referred as Glioblastoma Multiforme (GBM) [1]. Jason Corso et al. proposed Bayesian model based segmentation approach which is faster compared to other state of the art segmentation approaches to segment GBM brain tumour and edema. It is a novel approach of extending Segmentation by Weighted Aggregation (SWA) algorithm and incorporating model based affinities calculation which was model free conventionally. The Proposed approach was fully automated, faster in execution and achieved comparatively good segmentation accuracy than few existing techniques. Nearly 70% segmentation accuracy was achieved and a few failure cases were also reported with scope of improvement [12].

Fuzzy c-means (FCM) clustering method has been widely used for segmenting medical images [13,14,15]. Bing, et al. presented fuzzy level set based automated approach of segmenting medical images. After initial segmentations by FCM, controlling parameters of level sets are estimated and it further evolves to find object boundaries and results into robust segmentation. It achieved good segmentation results to separate WM, GM tissues in brain MRI and tumour in CT scan images [13].

Bidirectional Associative Memory (BAM)-type Artificial Neural Network (ANN) based method for segmentation and classification of medical images, proposed by Sharma, et al. [16] performed good even in presence of noise and achieved 100% classification rate. In this method, only for selecting texture features, supervision is required, but no training is required then after. The larger size object may increase computational time for segmentation.

Khotanlou, et al. [14] proposed and compared two methods for 3D brain tumour segmentation from MRI, one based on Fuzzy and deformable models, and other based on symmetry analysis and deformable models. Also, both methods were compared with manual segmentation and found comparable results. The first method based on symmetry analysis showed improved results in segmentation quality, while the other fuzzy based method was faster and unsupervised. Deformable models refined segmentation by imposing spatial constraints.

Nanthagopal, et al. [17] presented texture feature extraction method based on Wavelet, segmentation and classification by SVM and Probabilistic Neural Network (PNN). The SVM reported highest classification and segmentation accuracy, better than PNN, and was comparable with the ground truth. The texture features based on co-occurrence and dominant run length improved segmentation

accuracy. The limitation of the method was that it was applicable to CT scan images only, and needed new training during new dataset [17].

K-Nearest Neighbour (kNN) classifier was used to segment white matter lesion (WML) from brain MRI images in [18]. The performance of kNN was improved by incorporating spatial tissue type priors (TTPs), and by normalizing intensities. The proposed method reported good results with reference segmentation. TTPs helped to segment WML more accurately.

Demirhan, et al. [19] presented Self-Organizing Map (SOM) and Learning Vector Quantization (LVQ) based method for segmenting brain MRI images into grey matter, white matter and other background regions. LVQ was used to optimize and fine tune weights of SOM. Method reported good results for gray matter, while reported average results to segment white mater.

3.2 Statistical Methods

The applications of Gaussian Mixture Model (GMM) have been reported in [20, 21, 22] to estimate the distribution of intensities for the target classes. A comprehensive review of Gaussian mixture model based methods was presented by Balafar et al. for segmenting brain MRI images. They presented comparative analysis of methods as per reported results in [20]. The proposed segmentation methods were used to separate WM, GM and CSF from brain MRI where Markov Random Field (MRF) based methods have been reported in comparison with other approaches.

Hybrid approach of Markov Random Field and social algorithms comprising of ant colony optimization (ACO) and a Gossiping algorithm proposed by Yousefi, et al. was used to separate WM, GM and CSF regions of brain MRI. Their method improved computational time compared to classical MRF and hybrid method of MRF and ACO. Nearly equal or slightly improved Dice coefficient achieved by hybrid approach compared to two existing approaches. No significant improvement was found in the dice coefficient [23].

Multiple Gaussian components when used to represent multiple brain tissues, helped to produce smooth segmentation [21]. Greenspan, et al. proposed constrained Gaussian Mixture Model with multiple Gaussian components for segmenting brain MRI images. Expectation Maximization (EM) was used to learn parameters of GMM. The results were better and comparable with the state of the art algorithms like KVL algorithm, Marroquin algorithm and other reported results. Their method was completely automated and unsupervised approach where registration and atlas are not required. The results were compared based on Dice metric, Tanimoto metric and the mean absolute surface distance metric. It can be used as an alternative to the MRF model [21].

Saurabh et al. presented a novel approach of brain tumour segmentation from brain MRI using GMM based HRMF and Expectation Maximization method. Their hybrid approach of GMM and HRMF ensured smooth segmentation by incorporating spatial constraints. Their approach reported better results than FCM in terms of the smoothness of the segmentation. Multiple Gaussian components approximated brain tissues better than single Gaussian component [22].

A generative probabilistic model for segmenting brain tumour has been used in [24]. The proposed automated approach segmented tumour based on prior-atlas to study characteristics of healthy tissues and tumours from multimodal images. The method performed better than multivariate EM method for

segmentation. The use of MRF to incorporate spatial prior helped in identifying tumour with similar characteristics.

3.3 Contour based methods

Active contour models such as Fluid Vector Flow (FVF), Gradient Vector Flow (GVF) and Magneto Static Active Contour (MAC) which are intensity-based have been proposed by Sachdeva et al. to segment tumours from medical images [25]. To incorporate texture features along with intensity values, content-based active contour (CBAC) has been proposed. Volume segmentation is achieved which is termed as 2.5-D, extension of 2D. CBAC has given better results compared to GVF, MAC, FVF for segmenting homogeneous, heterogeneous tumours with varying background conditions [25].

Rajendran et al. [15] proposed fuzzy clustering and deformable models based brain tumour segmentation. Initial segmentation is performed using fuzzy clustering which gives initial contour and final contours are determined using deformable model using GVF which gives exact tumour boundary. Proposed method is found to be accurate and robust for segmenting brain tumours [15].

Li et al. presented hybrid method of Watershed and level set for segmenting MRI images [26]. Initial segmentation is done based on watershed method and then level set method is applied to detect boundaries of objects from initial segments. Proposed method is fast and efficient. Region boundaries are easily identified by level set method as their edges are already detected by watershed method. Obtained results are better than C-V model which is important region based segmentation technique [26].

3.4 Threshold based methods and other methods

Threshold based methods mainly selects intensity values as threshold from given image and then it divides image into set of classes or segments based on this threshold value. Many methods are presented by researchers for automated selection of threshold value and Otsu method of global thresholding is a known method but it is not suitable for brain tumour segmentation [2, 27]. Also, only thresholding method generally fails to segment the tumour and researchers have suggested hybrid approach with thresholding to improve results [22].

Brain symmetry and Bhattacharya coefficient based fully automated approach proposed by Dvorak, et al. [28]. could separate edema of different size, shape and at different location from FLAIR MRI images. Edema was identified based on comparison of histogram of blocks from left and right hemispheres. Asymmetry between histogram of blocks is compared based on Bhattacharya coefficient and most asymmetric block is expected to contain edema [28]. With same principle of brain symmetry, Baidya Nath Saha et al. presented fast bounding box approach to detect tumour or edema. Average dice coefficient achieved are 0.57 and 0.52. To find out exact boundaries of tumour, other algorithms need to be applied [29].

4 Review of Feature Extraction and Classification Methods for Brain MRI Image Analysis

Tumour tissues from other tissues of brain as well as different categories of tumours can be separated from MRI images based on specific characteristics of tumour which are represented by their features. Hence feature extraction techniques play key role in extracting tumour as well as for classifying medical

images into various categories based on extracted features. Most commonly used features for brain tumours are based on intensity values, texture properties, edge detection and intensity gradient [1]. Different tumours have different texture properties which represent different local image patterns, so texture based features can help in separating tumours. Also, texture based feature extraction methods have shown promising and reliable results than working with only intensity values of an image [30].

Many unsupervised and supervised techniques have been proposed by researchers using clustering as well as classification methods which are used for segmentation as well as for classification of medical images. Performance of classification algorithms are measured in terms of accuracy, specificity and sensitivity but their performance highly depends on initial pre-processing, segmentation and feature extraction techniques used. So, it is very important to optimize all phases of image analysis to achieve desired results.

Liu, et al. proposed hybrid approach of Gabor wavelet used for feature extraction, SVM used for tumour segmentation and LDA used for classification. Major goal was to separate different categories of tumour like PCNSL and GBM from T1c brain MRI images based on texture features and tumour shape. Proposed method achieved 100% sensitivity, 98% specificity and 98.9% accuracy in 3-fold cross-validation experiments. It was manual approach. Tumour-area and non-tumour selected to train the SVM [30].

Hybrid method of Gabor Wavelet and SVM was compared with other hybrid method of different DWT-Discrete Wavelet Transform (Daubechies-4) and SVM in [31] to classify MRI brain images. Gabor Wavelet was used for feature extraction and SVM was used for classification. Combination of different scales and orientations of Gabor filters and Linear, Sigmoid and RBF kernels of SVM were experimented. To reduce dimension, all Gabor filtered images were combined into one. They achieved 100% classification accuracy with proposed method with 3 scales, 8 orientations of Gabor and Sigmoid kernel of SVM [31].

Performance of Daubechies, Haar and Gabor wavelets was compared by Joohyun, et al. for extracting scale-invariant features. Salient image features were extracted with all the three wavelets, but Gabor wavelets outperformed other two. Haar had bad localization, Daubechies was not symmetric. Gabor wavelet performed well, but dimension of feature vector was very high [32].

Texture features from Lung CT scan images and other datasets extracted using Segmentation-based Fractal Texture Analysis (SFTA) in [33]. Performance compared with widely used methods like Haralick and Gabor filter banks and found better in case of SFTA. SFTA achieved higher precision and accuracy for both CBIR and image classification. Based on execution time, SFTA was faster than Gabor and Haralick with respect to feature extraction time. Gabor had equal accuracy for one dataset and less but nearly equal accuracy for other two datasets [33].

Feature extraction techniques like Scale Normalized Laplacian (SNL), Speeded-Up Robust Features (SURF), Shift Invariant Feature Transform (SIFT) were compared in [34] with newly introduced Brain Blob Detector and Descriptor (BBDD). All the techniques were applied on brain MRI images, where proposed BBDD method performed better than other mentioned algorithms like SNL, SURF and SIFT to discriminate sulcal blobs and gyral blobs [34].

Aminul, et al. proposed Multi-fractral feature extraction method from MRI images and modified AdaBoost to improve classification [35]. Multi-fractral feature extraction helped to extract important texture features, while modified AdaBoost algorithm changed weights of classifier based on different parameters which improved performance. It was used to segment low grade glioma tumour. No atlas registration was required. The method performed better to segment low grade glioma tumour compared to other state of the art methods reported in literature performed on BRATS dataset [35].

El-Dahshan, et al. [7] presented hybrid approach of Artificial Neural Network (ANN) for segmentation and classification, Discrete Wavelet Transform (DWT) for feature extraction and Principal Component Analysis (PCA) for dimensionality reduction. Also presented state of the art brain tumour segmentation and classification methods applied on MRI images. Achieved good results compared to recent machine learning techniques. The proposed hybrid approach reported 99% accuracy, 92% specificity and 100% sensitivity, which is comparable with other approaches and found better in some cases.

Manually segmented white matter lesion features were given to SVM classifier for training in [36] and AdaBoost was used to further improve the performance by focusing and learning from misclassified results. The AdaBoost method reduced false positive rate by focusing more on similar samples. The segmentation was challenging, because of smaller size of lesion compared to other region [36].

5 Summary and Discussion

This paper presents a comprehensive review of state of the art methods reported in literature for brain tumour detection and analysis. The literature contains methods for brain MRI image analysis to achieve different objectives like segmentation of GM, WM and CSF, detection of tumours, analysis of tumours like its type, location and size, segmenting necrotic area, edema alongwith tumour, etc. A major problem observed is that the quantification of results reported by different authors in their proposed methods are tested on different datasets and testing on common single standard dataset is missing. Also, standard parameters to measure and compare accuracy of algorithms are also missing. Different authors have tried to prove their algorithms based on their own parameters. However, some authors have tried to validate their results based on some known performance parameters like Dice metric, mean absolute surface distance metric and Tanimoto metric for measuring accuracy of segmentation but they are not gold standard for comparing performance of segmentation algorithms. It has been studied and can be summarized that different methods have been demonstrated with their performances for different cases, different performance measures and on different database. As feature extraction methods, literature review of Gabor, Wavelet transform, Discrete Wavelet Transform (Daubechies-4), Haar, Bhattacharya coefficient based approach, SFTA, Haralick, SURF, SIFT, SNL, GMM, multi fractal techniques has been presented in this paper. Out of many diverse features, the Gabor filters and Wavelet transform based methods have been widely used and reported in literature. Texture based features have also shown good applications for identification of tumour and its categories. In this paper, the methods of segmentation grouped and reviewed in four categories: machine learning and computational intelligence methods, statistical methods, contour based methods, threshold based, and other methods. As segmentation methods, a review of Neural network based methods (like BAM, PNN, SOM, LVQ), MRF based methods, fuzzy classification, deformable models, GMM, GMM with EM, GMM with HMRF and EM, watershed with level set, SVM, Active contour model, and kNN based methods have been presented. It is observed during the review that SVM, ANN and kNN have been widely used

as classifiers, while sometimes the Adaboost has been used to improve classification accuracy. Because of large intensity variations in MRI images, only thresholding based approaches do not provide desired results. Hence, in many works, the hybrid approach is suggested with thresholding method. However, it is also observed that the thresholding based methods are computationally fast and easy to implement. FCM has advantage of soft clustering, where it assigns membership values to each class. However, methods like FCM, Thresholding, deformable models and region growing are sensitive to noise. Hence, proper noise removal techniques should be applied in order to get desired results otherwise methods giving best results may also fail when noise levels present in different images vary. Sometimes, noise removal algorithms even though remove noise, but do not preserve edges of objects in an image which result into poor segmentation at later stage. On the other hands, methods exists which are robust and not influenced by noise like MRF which imposes strong spatial constraint, ANN and brain symmetry based on bhattacharya coefficient which compares histogram of block between left and right hemispheres based on assumption of brain symmetry. GMM based methods are computationally efficient and have capability to model complex problem. MRF imposes strong spatial constraint and has ability to represent complex dependency of data based on neighbourhood property. Because of this characteristic of MRF, it has been widely used for segmentation of tumour. In case of ANN, even though it performs well in learning and segmenting brain tumour, however trained network gives good results for patient specific dataset used for training and may not give expected results on different datasets because of different appearance and properties of tumour for different patient. On the other hand, SVM has got good generalization capability to produce good results even for previously unseen data of different patients. So, hybrid approach by combing strength of each individual method may give better results.

REFERENCES

[1] Stefan Bauer, Roland Wiest, Lutz-P Nolte and Mauricio Reyes , “A survey of MRI-based medical image analysis for brain tumour studies”, Journal of PHYSICS IN MEDICINE AND BIOLOGY, June 2013

[2] Roy, Sudipta, et al. "A Review on Automated Brain Tumor Detection and Segmentation from MRI of Brain." arXiv preprint arXiv:1312.6150 (2013).

[3] Gordillo Nelly, Eduard Montseny and Pilar Sobrevilla. "State of the art survey on MRI brain tumor segmentation." Elsevier, Magnetic resonance imaging 31.8 (2013): 1426-1438.

[4] MRI Brain Datasets available on http://www2.imm.dtu.dk/projects/BRATS2012/

[5] J. Mikulka and E. Gescheidtov, “An Improved Segmentation of Brain Tumour, Edema and Necrosis”, Progress In Electromagnetics Research Symposium Proceedings, Taipei, March, 2013

[6] Balafar, M. A., Ramli A. R., Saripan M. I., & Mashohor S., "Review of brain MRI image segmentation methods."Artificial Intelligence Review 33.3 (2010): 261-274.

[7] Jason J. Corso, Eitan Sharon, Shishir Dube, Suzie El-Saden, Usha Sinha and Alan Yuille, "Efficient multilevel brain tumor segmentation with integrated bayesian model classification." Medical Imaging, IEEE Transactions on 27.5 (2008): 629-640.

[8] Bing Nan Li , Chee Kong Chui , Stephen Chang , S.H. Ong,"Integrating spatial fuzzy clustering with level set methods for automated medical image segmentation." Computers in Biology and Medicine 41.1 (2011): 1-10.

[9] Khotanlou, Hassan, Olivier Colliot, Jamal Atif and Isabelle Bloch. "3D brain tumor segmentation in MRI using fuzzy classification, symmetry analysis and spatially constrained deformable models." Elsevier, Fuzzy Sets and Systems 160, no. 10 (2009): 1457-1473.

[10] Rajendran A. and R. Dhanasekaran. "Fuzzy clustering and deformable model for tumor segmentation on MRI brain image: a combined approach." Elsevier, Procedia Engineering 30 (2012): 327-333.

[11] Neeraj Sharma, Amit K. Ray, Shiru Sharma, K. K. Shukla, Satyajit Pradhan, Lalit M. Aggarwal, "Segmentation and classification of medical images using texture-primitive features: Application of BAM-type artificial neural network", Journal of Medical Physics, Jul-Sep; 33(3): 119–126, 2008.

[12] Nanthagopal A. Padma and R. Sukanesh. "Wavelet statistical texture features-based segmentation and classification of brain computed tomography images." IET image processing 7.1 (2013): 25-32.

[13] Steenwijk Martijn D., Petra JW Pouwels, Marita Daams, Jan Willem van Dalen, Matthan WA Caan, Edo Richard, Frederik Barkhof, and Hugo Vrenken. "Accurate white matter lesion segmentation by k nearest neighbor classification with tissue type priors (kNN-TTPs)." Elsevier, NeuroImage: Clinical 3 (2013): 462-469.

[14] Demirhan Ayşe, and İnan Güler. "Combining stationary wavelet transform and self-organizing maps for brain MR image segmentation", Elsevier, Engineering Applications of Artificial Intelligence 24.2 (2011): 358-367.

[15] Balafar, M. A. "Gaussian mixture model based segmentation methods for brain MRI images." Springer, Artificial Intelligence Review 41, no. 3 (2014): 429-439.

[16] Greenspan Hayit, Amit Ruf and Jacob Goldberger. "Constrained Gaussian mixture model framework for automatic segmentation of MR brain images." IEEE Transactions on Medical Imaging, 25.9 (2006): 1233-1245.

[17] Shah Saurabh A. and Narendra C. Chauhan. "An Automated Approach for Segmentation of Brain MR Images using Gaussian Mixture Model based Hidden Markov Random Field with Expectation Maximization." Journal of Biomedical Engineering and Medical Imaging 2.4 (2015): 57.

[18] Yousefi Sahar, Reza Azmi, and Morteza Zahedi. "Brain tissue segmentation in MR images based on a hybrid of MRF and social algorithms.", Elsevier, *Medical image analysis* 16, no. 4 (2012): 840-848.

[19] Menze B. H., Van Leemput K., Lashkari D., Weber M. A., Ayache N., & Golland, P., "A generative model for brain tumor segmentation in multi-modal images", In Medical Image Computing and Computer-Assisted Intervention–MICCAI 2010 (pp. 151-159),Springer Berlin Heidelberg.

[20] Sachdeva, Jainy, Vinod Kumar, Indra Gupta, Niranjan Khandelwal, and Chirag Kamal Ahuja. "A novel content-based active contour model for brain tumor segmentation." Magnetic resonance imaging 30, no. 5 (2012): 694-715.

[21] Li, Ning, Miaomiao Liu, and Youfu Li. "Image segmentation algorithm using watershed transform and level set method." IEEE International Conference on Acoustics, Speech and Signal Processing, 2007, ICASSP 2007, Vol. 1. IEEE, 2007

[22] N. Otsu, "A Threshold Selection Method from Gray Level Histograms", IEEE Transactions on Systems, Man, and Cybernetics, SMC-9 (1979) 62- 66.

[23] Dvorak P., K. Bartusek,and W. G. Kropatsch. "Automated Segmentation of Brain Tumour Edema in FLAIR MRI Using Symmetry and Thresholding.", PIERS Proceedings, Stockholm, Sweden, Aug. 12-15, 2013

[24] N Costa, Alceu Ferraz, Gabriel Humpire-Mamani, and Agma Juci Machado Traina. "An efficient algorithm for fractal analysis of textures." Graphics, Patterns and Images (SIBGRAPI), 2012 25th SIBGRAPI Conference on IEEE, 2012.

[25] Razlighi, Qolamreza R. and Yaakov Stern. "Blob-like feature extraction and matching for brain MR images." Engineering in Medicine and Biology Society, EMBC, 2011 Annual International Conference of the IEEE, 2011.

[26] Islam Aminul, Syed Reza, and Khan M. Iftekharuddin. "Multifractal texture estimation for detection and segmentation of brain tumors." IEEE Transactions on Biomedical Engineering, 60, no. 11 (2013): 3204-3215.

[27] Zhiqiang Lao, Dinggang Shen, Dengfeng Liu, Abbas F. Jawad, Elias R. Melhem, Lenore J. Launer, R. Nick Bryan, Christos Davatzikos, "Computer-Assisted Segmentation of White Matter Lesions in 3D MR Images Using Support Vector Machine", Academic Radiology, Vol 15, No 3, March 2008

SOCIETY FOR SCIENCE AND EDUCATION UNITED KINGDOM

JBEMi JOURNAL OF BIOMEDICAL ENGINEERING AND MEDICAL IMAGING

ISSN: 2055-1266
VOLUME 3 ISSUE 1

Detection and Classification of Focal Liver Lesions using Support Vector Machine Classifiers

[1]Deepti Mittal, [2]Anju Rani and [3]Ritambhara

Department of Electrical and Instrumentation Engineering, Thapar University, Patiala, Punjab, India.

[1]deeptimit@gmail.com; [2]anju.yaduvanshi@yahoo.com; [3]ritambhara3939@gmail.com

ABSTRACT

In the present work, two computer aided diagnostic systems are designed to detect and classify focal liver lesions such as Cyst, Hemangioma, Hepatocellular carcinoma and Metastases. The work evaluates clinically acquired ultrasound image database. Database contains 111 liver images comprising 95 images of focal lesions and 16 images of normal liver. Images are enhanced and manually segmented into 800 non-overlapping segmented-regions-of-interest. Afterwards, 208 textual features are extracted from each segmented-regions-of-interest. First diagnostic system is designed with one-against-one multiclass support vector machine classification approach showing 93.1% (512/550) overall accuracy on test dataset. Second system is designed with tree structured approach using four binary support vector machine classifiers showing 86.9% (478/550) overall accuracy on test dataset. Out of these two, one-against-one approach based diagnostic system outperforms the neural network based diagnostic system designed for the same purpose by providing 96.6% classification accuracy for typical cases and 85.3% for atypical cases.

Keywords: Ultrasound; Focal liver lesions; Feature extraction; Classification; Support vector machine classifier.

1 Introduction

Focal liver diseases constitute an important public health issue having very high incidence in Asian countries. Among a variety of focal liver diseases, liver cancer is one of the severe liver diseases. Liver cancer is the sixth most common focal malignant tumor in the world and the third most common cause of cancer-related deaths worldwide [1]. Imaging is an effective tool for early detection of liver abnormalities because in many cases it can detect even before they are palpable. Worldwide, ultrasound is always the first preference among various imaging modalities for screening focal liver lesions. Focal liver lesions are mostly found incidentally during ultrasound examinations, especially when it is performed as a part of the follow-up of patients with tumor, abdominal ache or cancer staging. Further, focal liver lesions with their atypical appearances may lead to misdiagnosis and confusion with other lesions even for the expert radiologists.

Present study is performed to design computer aided diagnostic (CAD) system to detect and classify focal liver lesions such as Cyst, Hemangioma (HEM), Hepatocellular carcinoma (HCC) and Metastasis

DOI: 10.14738/jbemi.31.1821
Publication Date: 08th February 2016
URL: http://dx.doi.org/10.14738/jbemi. 31.1821

(MET) using support vector machine (SVM) classifiers. Review of literature reveals that neural network (NN) had been used as a classifier in several studies to design CAD system for detection and classification of focal liver lesions [2-5]. Further, a NN based diagnostic system to classify among five liver tissue categories, viz., four above mentioned focal lesion tissue categories and normal (NOR) liver tissue category, has presented by Mittal *et. al.* [12] showing 86.5% test accuracy. It has also revealed by literature review that SVM classifier had not been used to develop the CAD systems for these focal liver tissue categories in spite of the fact that SVM classifier had been preferred in many other clinical applications, such as breast cancer detection, thyroid nodule detection, liver fibrosis identification, cervical lymph nodes, liver cancer detection using CT images, retinal exudates detection showing good test accuracies [6-11]. Another reason to opt SVM classifier is that the generalized performance of NN based diagnostic system was not found as excellent as its performance on the training and validation sets [12]. The reason for such performance of NN based diagnostic system may be the curse of dimensionality. The curse of dimensionality arises when number of features and that of available training samples are unbalanced. For a classification problem with d features, it is estimated that a minimum of $10d$ samples per training class is necessary for reliable statistical estimates [13]. This requirement is usually not feasible due to constraints of data collection, such as dependency of data collection on frequency of occurrence of patients having specific diseases and so on. Therefore, powerful learner such as NN having small number of training samples with 208 features may cause overfitting especially when performing intensive search for the best system model. On the other side, SVM has the potential to produce high classification accuracy with limited number of training samples having hundreds of features. It is a good candidate for image classification showing its lower sensitivity to the curse of dimensionality. Therefore in the present study SVM classifiers are used in diagnostic system designing.

Furthermore, SVM formulation is originally designed for two class problems therefore it performs well in binary classification. Yet, most of the real life diagnostic problems are not binary. There are some feasible strategies that can extend the formulation of SVM to solve a multi-class classification problem. To solve the multiclass problem, many multiclass SVM methods have already been developed, differing from each other in the definitions of the binary SVMs and in the combining strategy of the binary SVMs [14-25]. These methods can be divided into two types. One, called single machine approach, modifies the binary class objective function and allows simultaneous computation of multiclass classification by directly considering all classes to solve a single optimization problem [16, 20], whereas the other is to construct and combine several binary classifiers. The latter strategy based on the combination of many binary classifiers has been proved to be more efficient than the single machine approach. There are a good number of approaches, which consider a multi-class classification strategy from the combination of many binary SVM classifiers, such as one-against-all (OAA) [14], one-against-one (OAO) [15] and all-and-one (AAO) [22], direct acyclic graph SVM (DAGSVM) [18], the hierarchical tree structure based methods [21, 23, 25], and error correcting output codes (ECOC) methods [17, 19, 24]. Rifkin and Klautau [26] did many carefully controlled experiments and proposed that a simple scheme such as OAA and OAO is preferable to a more complex ECOC methods or single machine schemes, once the best binary classifier available is used. Hsu and Lin [27] suggested that OAO and DAGSVM may be more suitable for practical use after comparing the single machine approaches with OAA, OAO, and DAGSVM. OAO and DAGSVM perform very similar, which is due to the fact that both multiclass SVM methods use the same type of

binary SVM classifiers. DAGSVM and OAO have the fastest training time. The OAO can use in training many more binary SVMs than the OAA, even then OAO may require much lesser training time than the OAA. Moreover, OAO can achieve comparable or even lesser test computational complexity compared with OAA due to the large number of shared support vectors between binary SVMs of OAO [28]. These detailed experiments and comparative studies have suggested that OAO is useful and more practical among the mentioned approaches for real application in term of accuracy and computational cost. As a result, OAO is used as a SVM multiclass classification method in this work.

The OAO multiclass classification approach has to solve too many binary decision functions when the multi-class problem has a large number of classes. Also too many binary tests are required to be conducted before a final classification is made. The hierarchical tree-based SVM methods, which combine support vector machine and binary tree architecture, have the characteristics, such as lower number of binary classifiers required to be trained and faster decision speed. These advantages of tree based approach become more and more prominent as the number of the class increases. In multiclass classification problem of N classes, the OAO approach requires $N(N-1)/2$ binary classifiers to be trained, whereas tree structured SVM approach requires only $(N-1)$ binary classifiers to be trained. Therefore, finally one-against-one and hierarchical tree structured based SVM approaches are selected to implement the multiclass classification problem.

Therefore, two CAD systems are designed using two different multiclass SVM classification approach, one is one-against-one (OAO) approach and other is tree structured approach. In the end, both systems are compared with their test performances. Finally, CAD system with best performed multiclass SVM classification approach is compared with NN classification system that was designed previously for the same purpose [12].

2 Materials and Methods

2.1 Subjects

Ultrasound image database is acquired from the patients who underwent a medical examination at the Department of Radio diagnosis, Postgraduate Institute of Medical Education & Research (PGIMER), Chandigarh, India during the period March 2008 to May 2009. After ultrasound examinations on 88 patients, a total of 111 US images comprising 95 focal liver lesion images (17 Cyst, 15 HCC, 18 HEM and 45 MET) and 16 normal liver images were acquired.

2.2 Image Enhancement

Ultrasound image database is enhanced by the regularized MSRAD-template 9 method proposed by Mittal *et. al*. [29]. This image preprocessing is used in order to improve the overall visual quality and contrast of ultrasound images.

2.3 Segmentation of Region-of-Interest

Regions-of-interest marked by an expert radiologist in each ultrasound image are segmented into maximum possible number of non-overlapping 25×25 sized regions and these regions are termed as segmented-regions-of-interest (SROIs). A SROI is used as texture sample representing a liver tissue category. The use of SROI for feature extraction reduces the complexity and calculation time. Non-overlapping SROIs are taken in order to design an accurate and robust system.

The 800 SROIs are segmented within the regions of interest in the acquired liver image database of 111 ultrasound images. A collection of SROIs is termed as dataset. The dataset having 800 SROIs is divided into training and testing sets. Training set contains 250 SROIs whereas remaining 550 SROIs are used for testing the classification systems.

2.4 Feature Extraction and Selection

The five texture based feature extraction methods from first, second and higher order statistics, along with spatial filtering and multi-resolutional approaches are used to achieve good classification accuracy. The methods chosen from these approaches are (i) first order statistics [30, 31], (ii) spatial gray level dependence matrix [32-34], (iii) gray level run length matrix [35, 36], (iv) texture energy measures [37] and (v) Gabor wavelet [38, 39] respectively.

All possible diagnostically important features are considered from the methods and an exhaustive set of 292 (9 of FOS, 80 of SGLDM, 11 of GLRLM, 72 of TEM and 120 of Gabor) features are extracted. The feature set is reduced further with the aim to retain only effective and discriminating features. The feature selection strategy, termed as sensitivity analysis, is designed to identify the features with significant information content from the extracted feature set and to discard the features those are not important from classification point of view. In sensitivity analysis, mean-range plot of each feature is studied to measure the sensitivity in providing discrimination among various liver tissues. Thus, the extracted features were reduced to a set of 208 sensitive features [12].

2.5 Classification

In the present work, two CAD systems are designed using two different multiclass SVM classification approach, one is one-against-one (OAO) approach and other is tree structured approach.

In OAO approach, SVM classifiers for all possible pairs of classes are created from the training set of N classes, each classifier being trained on only two out of N classes, giving a total of $N(N-1)/2$ classifiers. Applying each classifier to the test data gives one vote to the winning class. The data is assigned the label of the class with most votes.

In tree structured SVM approach (N-1) binary classifiers are trained, and each classifier separates a pair of classes at each node of the tree. The performance of tree structured SVM classifier depends on the structure of the binary tree. The closer the occurrence of classification error to the root node, the greater is the overall classification error. Schematic of the designed tree structure for focal lesion detection and classification is shown in Fig. 1.

Figure 1 demonstrates the tree structure with four nodes to detect abnormal (focal diseased) tissues and then classify them into four liver lesion categories. Four-binary SVM classifiers, one at each node, are used for this purpose. The binary-SVM at first node (N1) discriminates SROIs into normal and focal diseased liver tissues. According to pathology, focal diseased liver tissues can be classified into four major categories i.e. Cyst, HCC, HEM and MET. Ultrasound is especially useful in distinguishing Cysts (major category of fluid lesion) from solid lesions. Therefore, binary-SVM at the second node (N2) tries to discriminate all detected SROIs of focal tissues into the fluid lesion and solid lesion. Solid lesion tissues can be further categorized as solid benign and solid malignant.

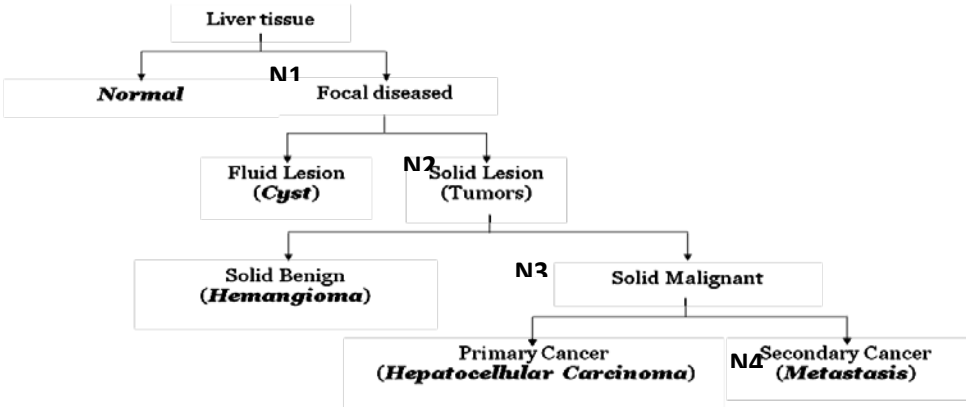

Figure. 1. Schematic of the designed tree structure for multi-class classification using binary SVM classifiers.

HEM is major category of solid benign and it can be detected easily on ultrasound with its typical appearance in comparison to the solid malignant lesions. Therefore, binary SVM at the third node (N3) is used to classify these lesions. Finally binary-SVM at the forth node (N4) is used to classify solid malignant lesions into primary malignant and secondary malignant. HCC is major category of primary malignant and MET is major category of secondary malignant. These liver tissue categories are not comfortably detected on ultrasound in comparison to the rest other mention liver tissues, therefore classified at the last node of the tree. Accordingly, liver tissues can be separated into five categories using the four-binary SVMs in tree structure.

In the designed CAD systems, SVM classifiers are implemented using LIBSVM tool, version 2.6. Radial basis kernel is applied in each SVM classifier. The parameters, i.e., penalty for errors (C) and RBF kernel width (σ), of each SVM classifier are adjusted properly for the optimized results. Selection of proper parameter settings of each binary classifier of the classification system is done with train dataset using cross validation procedure. Proper parameter setting is needed to optimize classification performance and to avoid over fitting and under fitting problems. In the experiments, the performance of a classifier is presented either in terms of confusion matrix with overall accuracy (in percentage) or the area under the ROC curve.

Finally, the performance of the two CAD systems is compared on the basis of their overall accuracy for liver tissue classification using ultrasound data.

3 Results

The results of designed CAD systems are presented in this section. First, the results of designed CAD system using OAO multiclass classification approach are studied. The performances of binary SVM classifiers, which are used in the implementation of this system, are evaluated initially. There are ten different binary classification tasks which can be performed by taking any two liver image categories at a time. Each binary classifier is first trained to get the best classification accuracy with the set of 208 sensitive features, and then the performance of this designed classifier is evaluated on test dataset. Evaluation is performed to assess whether any two liver image categories are adequately differentiated by the designed system or not.

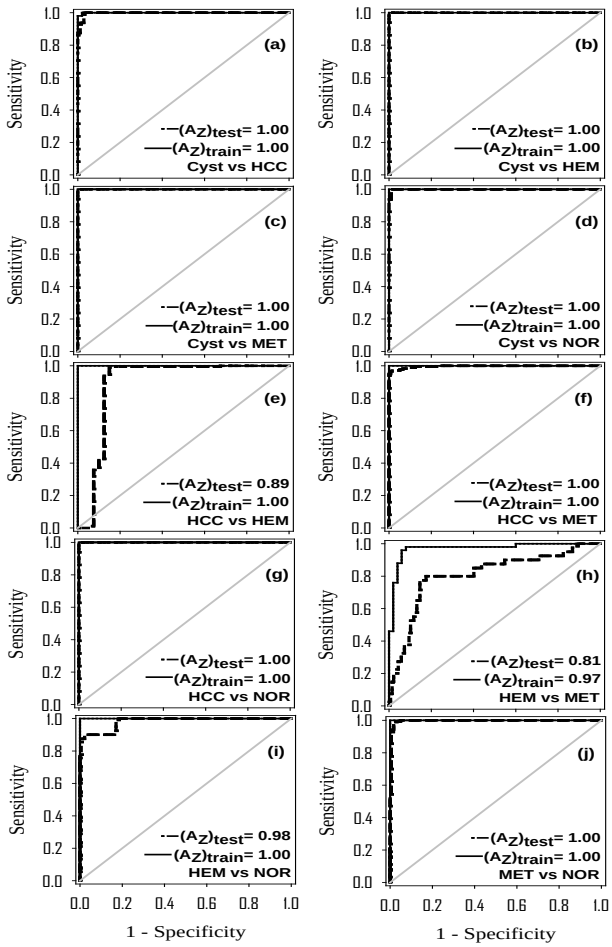

Figure 2. Training and test ROC curves for ten binary classification tasks performed with OAO approach based SVM classifiers.

Figures 2(a)-(j) show ROC curves with train and test datasets for different SVM based binary classification tasks. The results as shown in Fig. 2(a)-(d) depict that Cyst is clearly differentiated from rest other liver image categories having ideal performances ($(A_Z)_{test}$=1.00 and $(A_Z)_{test}$=1.00)) with train and test datasets. In Figure 2(e), the differentiation capability of designed SVM classifier for HCC vs. HEM is ideal on train dataset and A_Z value on test dataset is 0.89 which is reasonably high for classification. Further, HCC is ideally differentiated from MET and NOR liver image categories as shown in Fig. 2(f) and (g). Differentiation provided by the SVM classifier in between HEM and MET is not ideal even on training dataset as can be seen in Fig. 2(h). Still both, training and testing performances are impressively high ($(A_Z)_{train}$=0.97 and $(A_Z)_{test}$=0.81)). Finally, the rest two classification tasks, HEM vs. NOR and MET vs. NOR, depict high performances as shown in Fig. 2(i) and (j) respectively. Hence, it can be said that OAO approach based SVM provides sufficiently high discrimination on almost all two class classification tasks.

Table 1. Confusion matrix on the test results of OAO approach based multi-class SVM classifier.

Known class	Test results of OAO approach based multi-class SVM classifier					Class	Overall
	CYST	HCC	HEM	MET	NOR	Accuracy (%)	Accuracy (%)
CYST	15	1	0	0	0	93.8(15/16)	93.1(512/550)
HCC	2	170	3	1	1	96.0(170/177)	
HEM	0	0	33	7	0	82.5(33/40)	
MET	0	1	18	116	0	85.9(116/135)	
NOR	1	1	1	1	178	97.8(178/182)	

Table 1 shows the test results in the form of confusion matrix when above mentioned binary SVM classifiers are used for multiclass classification using OAO approach. Classification of Cyst is fairly high with one misclassified case out of sixteen. Out of 177 SROIs of HCC, 170 are detected correctly that yields 96% of class accuracy. Similarly high class accuracy for NOR liver tissues is obtained with the correct detection of 178 out of 182 SROIs. Further, the detection rate for HEM is comparatively low as only 32 SROIs out of 40 are detected correctly. Similarly, in case of MET, there is only 116 out of 135 tested SROIs are detected correctly. Finally, the overall accuracy of this CAD system is 93.1% as out of 550, 512 SROIs are classified correctly.

Tree structured multiclass SVM classification system first detects SROIs of diseased class and subsequently distinguishes among different lesion types. Train and test performances of classifier at each node in tree-structured multiclass SVM classification system are presented in form of ROC curves. These curves are shown in Fig. 3.

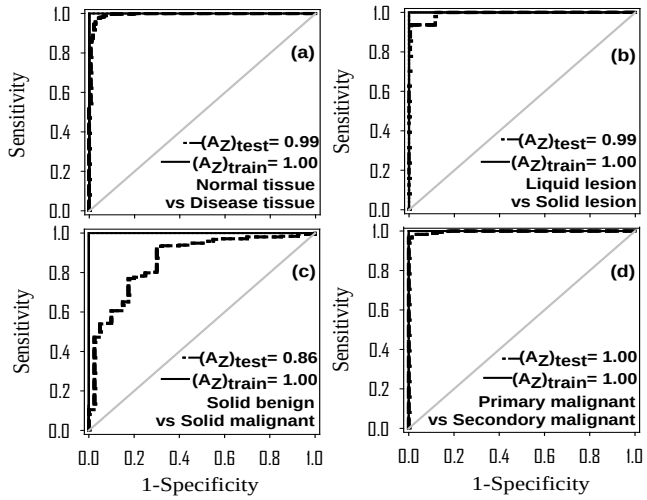

Figure 3. Training and test ROC curves of four binary SVM classifiers for the tasks performed at nodes of the tree structure.

In Figure 3(a), the differentiation capability of classification system in between normal and diseased tissues is ideal on train dataset and near to ideal ($(A_Z)_{test}$=0.99) on test data set. After the excellent performance at detection stage, all detected lesion SROIs are classified into liquid lesion and solid lesion. It can be observed from Fig. 3(b) that the A_Z values for the classification between liquid and solid lesions are 1.00 and 0.99 with the training and testing datasets, respectively. Further the classification of the detected solid lesion into solid benign (non-cancerous) and solid malignant (cancerous), is 100% on

training dataset having A_Z value of 1.00. This classification stage proves to be more challenging on test set with A_Z value of 0.86 as shown in fig. 3(c). The last stage is classification of solid malignant SROIs into primary and secondary cancer. The results of this classification step as appeared in fig. 3(d) depict that ideal performances ($(A_Z)_{train}$=1.00 and $(A_Z)_{test}$=1.00)) are achieved by the system on train and test datasets and suggest perfect separation in between primary and secondary malignant. The performance of tree structured multiclass classification system is also evaluated in terms of class accuracy and overall accuracy and these results are listed in Table 2.

Table 2. Test performance of tree structured multiclass SVM classifier.

Tree structured multiclass SVM classifier		Accuracy	Overall accuracy
N1(first stage)	Normal/ Diseased	96.9% (533/550)	86.9%
N2(second stage)	Liquid lesion/Solid lesion	98.6% (363/368)	(478/550)
N3(third stage)	Solid benign/Solid malignant	87.5% (308/352)	
N4(last stage)	Primary malignant/Secondary malignant	98.1% (306/312)	

Table 3. Confusion matrices for all four stages of the designed tree structured SVM classification approach based CAD system.

	Focal diseased	**Normal**
Focal diseased (368)	361	7
Normal (182)	10	172
	Solid lesion	Liquid lesion
Solid lesion (352)	348	4
Liquid lesion (16)	1	15
	Solid Malignant	Solid Benign
Solid Malignant (312)	280	32
Solid Benign (40)	12	28
	Secondary Malignant	Primary Malignant
Secondary Malignant (135)	135	0
Primary Malignant (177)	6	171

Table 3 shows the confusion matrices reporting these results. The first stage of classification system is mass screening for lesion detection. At this stage, 96.9% (533/550) test SROIs are correctly classified as either normal or diseased. The specificity is 94.5% (172/182), while the sensitivity is 98.1% (361/368). In the next stage the accuracy achieved for the classification of detected lesions in between liquid lesions and solid lesions is 98.6% (363/368). System specificity and sensitivity to classify solid lesions are 93.8% (15/16) and 98.9% (348/352) which are high values in performances.

The results of confusion matrix for solid benign and solid malignant show that the test accuracy of this important stage is 87.5% (308/352). Solid malignant SROIs are classified with sensitivity 89.7% (280/312) and specificity 70% (28/40). Last stage is another important classification stage as here designed system is evaluated for distinction in between cancer classes, as primary malignant and secondary malignant. At this stage, system accuracy is 98.1% showing sensitivity in detection of primary lesion as 96.6% and sensitivity in detection of secondary malignant lesion as 100%. Finally, out of 550 SROIs, 478 are classified correctly and the overall accuracy comes out to be 86.9%.

The test results of OAO and tree structured multiclass SVM classification approaches are compared in terms of overall accuracy. Both of the CAD systems are designed and evaluated with same database and the set of 208 sensitive features, therefore the nature of the problem is same. The overall correct decisions with OAO approach based multiclass SVM classifier are 512 out of 550 SROIs yielding 93.1% overall accuracy. On the other hand, overall correct decisions with tree structured approach based CAD system are 478 out of 550 yielding 86.9% overall accuracy. Therefore OAO approach based CAD system is better as compared to tree structured based CAD system in terms of overall accuracy.

Table 4. Confusion matrix on the test results of CAD system based on OAO multi-class SVM classification approach for typical cases.

Known class	Test results of CAD system based on OAO multi-class SVM classification approach (Typical cases)					Class accuracy (%)	Overall accuracy (%)
	CYST	HCC	HEM	MET	NOR		
CYST	13	0	0	0	0	100.0(13/13)	96.6(367/380)
HCC	0	115	2	1	1	96.6(115/119)	
HEM	0	0	7	0	0	100.0(7/7)	
MET	0	1	4	54	0	91.5(54/59)	
NOR	1	1	1	1	178	97.8(178/182)	

Table 5 Confusion matrix on the test results of CAD system based on OAO multi-class SVM classification approach for atypical cases.

Known class	Test results of CAD system based on OAO multi-class SVM classification approach (Atypical cases)					Class accuracy (%)	Overall accuracy (%)
	CYST	HCC	HEM	MET	NOR		
CYST	2	1	0	0	0	66.7(2/3)	85.3(145/170)
HCC	2	55	1	0	0	94.8(55/58)	
HEM	0	0	26	7	0	78.8(26/33)	
MET	0	0	14	62	0	81.6(62/76)	
NOR	0	0	0	0	0	0	

The performance of OAO approach based CAD system is also evaluated by examining class accuracies of typical and atypical SROIs in test set with separate confusion matrices as shown in Tables 4 and 5 respectively. As given in Table 4, the class accuracies for typical SROIs of Cyst, HCC, HEM, MET and NOR are 100% (13/13), 96.6% (155/119), 100.0% (7/7), 91.5% (54/59) and 97.8% (178/182) respectively with the overall accuracy of 96.6% (367/380). Table 5 shows the test results from atypical set of SROIs. The overall accuracy of 85.3% (145/170) is observed for atypical cases. The class accuracies for atypical SROIs of Cyst, HCC, HEM and MET are 66.7% (2/3), 94.8% (55/58), 78.8% (26/33) and 81.6% (62/76) respectively.

Finally test results of OAO approach based CAD system are compared with the NN based CAD system [12]. This comparison is made to decide which CAD system out of these two shows the better performance in classification among liver tissues with the selected set of 208 sensitive features. It is needed to mention that a validation set is used in process of development of NN based CAD system [12]. By definition, validation set is the test set that is used to evaluate the performance of neural network model during training process for the best model selection and to control the over-fitting problem of designed system. Therefore, the results of NN based CAD system on validation set and test set are put together for the comparison of these results with the results of SVM based CAD system. A confusion

matrix is compiled with the test results of 550 test SROIs to show the exact performance comparison in between NN and SVM based CAD systems.

Table 6 Confusion matrix representing the comparison of the test results on the set of 550 SROIs with NN and SVM based CAD systems

Known class		Test results on the set of 550 SROIs					Class accuracy (%)	Overall accuracy (%)	
		CYST	HCC	HEM	MET	NOR		NNM	SVM
CYST	NN-CAD	15	1	0	0	0	93.8(15/16)	87.6	93.1
	SVM-CAD	15	1	0	0	0	93.8(15/16)	(482/550)	(512/550)
HCC	NN-CAD	2	165	6	3	1	93.2(165/177)		
	SVM-CAD	2	170	3	1	1	96.0(170/177)		
HEM	NN-CAD	0	2	33	5	0	82.5(33/40)		
	SVM-CAD	0	0	33	7	0	82.5(33/40)		
MET	NN-CAD	2	4	25	100	4	74.1(100/135)		
	SVM-CAD	0	1	18	116	0	85.9(116/135)		
NOR	NN-CAD	0	0	5	8	169	92.9(169/182)		
	SVM-CAD	1	1	1	1	178	97.8(178/182)		

Table 6 shows the confusion matrix with the combined test results of these two CAD systems. The result analysis of both the systems reveals that one SROI of Cyst is misclassified as HCC, yielding equal class accuracy for both systems. The class accuracy of HCC with SVM system is 2.8% higher than that with NN based CAD system. The results of HEM classification are same for both the systems. Out of 135 SROIs of MET, 100 and 116 SROIs are correctly classified by NN and SVM NN based CAD systems respectively, thus yielding 11.9% higher class accuracy with SVM system. Similarly the class accuracy of NOR liver tissue with SVM system is 7% higher than that with NN system. Thus the OAO approach based SVM system outperforms the NN system with their overall accuracy of 93.1% and 87.6% respectively. Finally as SVM system is better in performance with 30 more correct decisions in comparison with NN system, it can be said that the test results obtained by SVM classifier are more robust as compared to the NN system for the same feature set and dataset used.

4 Discussions

Ten binary classifiers are designed and tested to implement OAO approach based CAD system. There is the limitation in providing clear differentiation in between HEM and MET in the designed binary classifier with given feature set which can be seen in Fig. 2(h) showing no ideal performance on training dataset. Still in the case, both training and testing performances are imposingly high to accept the designing of this classifier. Table 1 shows the performance of OAO approach based CAD system using these binary classifiers for Cyst, HCC, and NOR liver tissues are sufficiently high with class accuracy of 93.8%, 96.0%, and 97.8% respectively. This SVM classification approach shows reasonable accuracy of 80.0% and 85.9% for HEM and MET respectively.

The performance of tree structured based CAD system depends on the designing of binary classifiers at tree nodes. Binary classifiers at tree nodes are trained to separate SROIs into the desired classes. Tree structured based CAD system for mass screening is highly promising with high sensitivity in lesion detection on test dataset missing only 1.9% (7/361) of SROIs from diseased category. Further, system sensitivity for solid lesion classification form diseased cases is quite high missing only 1.1% (4/352) cases. However, system performance is limited at the third stage of the tree structured CAD system. The

results of confusion matrix, as shown in Table 3, reflect that solid benign (non-cancerous) and solid malignant (cancerous) are particularly hard to separate for the system. The test accuracy of this important stage is 87.5% (308/352) which shows performance degradation in comparison to the previous stages, but still this accuracy is satisfactory as images of these classes appear most of the time with overlapping characteristics on ultrasound images and create confusion even to the expert radiologist during visual evaluation. The ability to correctly identify cancer SROIs within the testing set is promising, considering the difficulty of the task. Finally, at the last stage system performance is excellent with accuracy and sensitivity values on test dataset.

Further, the choice for a multiclass approach depends on the problem in hand and it needs the consideration of the accuracy requirement along with the computational time, the resources available and the nature of the problem in hand. In classification problem with large number of classes, the number of binary SVM classifiers in OAO approach are much higher than those in tree structured based approach and therefore the processing time in OAO approach based multi-class classification would be higher than that in tree structured based approach. However, in classification problem with small number of classes like the present one where the number of classes is five, only ten binary classifiers are needed in OAO approach, so difference of processing time in both the types of approach is not significant and therefore one should go for the approach which gives the better results.

Finally, it can be concluded that one-against-one approach based CAD system provides higher overall accuracy, with correct decision on 34 more SROIs showing an improvement of 6% in correct decisions. Moreover, overall accuracy and class accuracies, all are sufficiently high to demonstrate the effective performance of the designed CAD system with typical cases. The test performances of atypical cases are lesser than that of typical cases; still these results are promising for the application of OAO approach based CAD system with atypical cases too.

Results of SVM system are better than that of NN system even after improvement of NN classifier by introducing two-step classification concept. Thus it can be said that as compared to NN system, the SVM system has high anticipation level in the diagnosis of focal liver disorders. The test results of each SROIs from both the systems are further analyzed to go in more details. It can be seen that there is one misclassification case out of 16 SROIs of Cyst by both the systems. But the SROI that is misclassified by NN system is different from the SROI that is misclassified by SVM system. That means the SROI that is misclassified by SVM system is correctly classified by the NNM system. Several similar instances have been observed on analyzing the test results of each SROIs. Thus it can be said that NN system has a potential to detect those cases which are not correctly detected by the SVM system, therefore importance of NN system cannot be ignored. Even, the problems of overfitting likely occur because the complexity of the diagnostic model is not controlled in empirical risk minimization on which neural network is based. To be useful in practice where only limited training examples are available, the non-asymptotic analysis of the quality of empirical risk minimization is necessary. To address these issues, structural risk minimization has been suggested in SVM theory. Structural risk minimization minimizes the upper bound on the generalization error, as against empirical risk minimization which minimizes the error on the training data

5 Conclusion

The results leads to the conclusion that SVM-CAD system with tree structured approach can produce a high accuracy rate of 86.9% in focal liver lesion detection and classification. The approach is valuable to improve the accuracy of the diagnosis of liver cancer and to reduce the number of biopsies. CAD system with OAO approach based multi-class SVM classification in comparison to that of tree structured approach based multi-class SVM classification provides the better results in terms of overall accuracy of 93.1% with the selected set of 208 sensitive features. The proposed OAO-SVM system outperforms the system designed with neural network using the same database. The overall classification accuracy with this system has been achieved as 96.6% for typical cases and 85.3% for atypical cases.

ACKNOWLEDGMENTS

Author acknowledges the Prof. Vinod Kumar, Indian Institute of Technology, Roorkee, India and Department of Radiodiagnosis and Imaging, Postgraduate Institute of Medical Education and Research, Chandigarh, India for their support in carrying out this research work.

REFERENCES

[1] Herszenyi, L., Tulassay, Z., 2010. Epidemioligy of gastrointestinal and liver tumors. European Review for Medical and Pharmacological Sciences 14, 249-258.

[2] Sujana, H., Swarnamani, S., Suresh, S., 1996. Application of artificial neural networks for the classification of liver lesions by image texture parameters. Ultrasound in Medicine and Biology 22, 1177-1181.

[3] Yoshida, H., Casalino, D.D., Keserci, B., Coskun, A., Ozturk, O., Savranlar, A., 2003. Wavelet-packet-based texture analysis for differentiation between benign and malignant liver tumors in ultrasound images. Physics in Medicine and Biology 48, 3735–3753.

[4] Balasubramanian, D., Srinivasan, P., Gurupatham, R., 2007. Automatic classification of focal lesions in ultrasound liver images using principal component analysis and neural networks. In: Proceedings of 29th International Conference IEEE EMBS, Lyon, France, pp. 2134-2137.

[5] Poonguzhali, S., Ravindran, G., 2008. Automatic classification of focal lesions in ultrasound liver images using combined texture features. Information Technology Journal 7, 205-209.

[6] Krishna, M.M.R., Banerjee, S., Chakraborty, C., Chakraborty, C., Ray, A.K., 2010. Statistical analysis of mammographic features and its classification using support vector machine, Expert Systems with Applications 37, 470-478.

[7] Tsantis, S., Cavouras, D., Kalatzis, I., Piliouras, N., Dimitropoulos, N., Nikiforidis, G., 2005. Development of a support vector machine-based image analysis system for assessing the thyroid nodule malignancy risk on ultrasound. Ultrasound in Medicine and Biology 31, 1451-1459.

[8] Cao, G., Shi, P., Hu, B., 2005. Liver fibrosis identification based on ultrasound images. In: Proceedings of 27th IEEE Annual Conference on Engineering in Medicine and Biology, Sanghai, China, pp. 6317-6320.

[9] Zhang, J., Wang, Y., Dong, Y., Wang, Y., 2007. Ultrasonographic feature selection and pattern classification for cervical lymph nodes using support vector machine. Computer Methods and Programs in Biomedicine 88, 75-84.

[10] Krishan, A., Mittal, D., 2015. Detection and Classification of Liver Cancer using CT Images.International Journal on Recent Technologies in Mechanical and Electrical Engineering 2, 93-98.

[11] Mishra, S. K., Mittal., D., sunkaria, R. K., 2015. Designing of Computer Aided Diagnostic System for the Identification of Exudates in Retinal Fundus Image. Journal of Biomedical Engineering and Medical Imaging 2, 29-40.

[12] Mittal, D., Kumar, V., Saxena, S.C., Khandelwal, N., Kalra, N., 2011. Neural network based focal liver lesion diagnosis using ultrasound images. Computerized Medical Imaging and Graphics 35, 315–323.

[13] Jain, A.K., Duin, R.P.W., Mao, J., 2000. Statistical pattern recognition: a review. IEEE Transactions on Pattern Analysis and Machine Intelligence 22, 4–37.

[14] Bottou, L., Cortes, C., Denker, J., Drucker, H., Guyon, I., Jackel, L., LeCun, Y., Muller, U., Sackinger, E., Simard, P., Vapnik, V., 1994. Comparison of classifier methods: A case study in handwriting digit recognition. In: Proceedings of International Conference on Pattern Recognition, pp. 77–87.

[15] Friedman, J., 1996. Another approach to polychotomous classification. Stanford, CA: Department of Statistics and Stanford Linear Accelerator Center, Stanford University, available at http://www-stat.stanford.edu/~jhf/ftp/poly.pdf.

[16] Vapnik, V.N., 1998. Statistical Learning Theory. Wiley, New York.

[17] Allwein, E.L., Schapire, R.E., Singer, Y., 2000. Reducing multiclass to binary: A unifying approach for margin classifiers. Journal of Machine Learning Research 1, 113–141.

[18] Platt, J.C., Cristianini, N., Shawe-Taylor, J., 2000. Large margin DAGs for multiclass classification, in: Sollam, S.A., Leen, T.K., Mu¨ller, K.-R. (Eds.), Advances in Neural Information Processing Systems, MIT Press, Cambridge, MA, pp. 547–553.

[19] Dietterich, T.G., Bakiri, G., 1995. Solving multiclass learning problems via error-correcting output codes. Journal of Artificial Intelligence Research 2, 263–286.

[20] Crammer, K., Singer, Y., 2001. On the algorithmic implementation of multiclass kernel-based vector machines. Journal of Machine Learning Research 2, 265–292.

[21] Chen, Y., Crawford, M.M., Ghosh, J., 2004. Integrating support vector machines in a hierarchical output space decomposition framework. In: Proceedings of International Geoscience and Remote Sensing Symposium, pp. 949–952.

[22] García-Pedrajas, N., Ortiz-Boyer, D., 2006. Improving multiclass pattern recognition by the combination of two strategies. IEEE Transactions on Pattern Analysis and Machine Intelligence 28, 1001-1006.

[23] Fei, B., Liu, J., 2006. Binary tree of SVM: A new fast multiclass training and classification algorithm. IEEE Transactions on Neural Network 17, 696–704.

[24] Pujol, O., Radeva, P., Vitià, J, 2006. Discriminant ECOC: A heuristic method for application dependent design of error correcting output codes. IEEE Transactions on Pattern Analysis and Machine Intelligence 28, 1007-1012.

[25] Chen, J., Wang, C., Wang, R., 2008. Combining support vector machines with a pairwise decision tree. IEEE Geoscience and Remote Sensing Letters 5, 409–413.

[26] Rifkin, R., Klautau, A., 2004. In defense of one-vs-all classification. Journal of Machine Learning Research 5, 101–141.

[27] Hsu, C., Lin, C., 2002. A comparison of methods for multiclass support vector machines. IEEE Transactions on Neural Network 13, 415–425.

[28] Chen, J., Wang, C., Wang, R., 2009. Using stacked generalization to combine SVMs in magnitude and shape feature spaces for classification of hyperspectral data. IEEE Transactions on Geoscience and Remote Sensing 47, 2193-2205.

[29] Mittal, D., Kumar, V., Saxena, S.C., Khandelwal, N., Kalra, N., 2010. Enhancement of the ultrasound images by modified anisotropic diffusion method. Medical & Biological Engineering & Computing 48, 1281–1291.

[30] Golemati, S., Tegos, T.J., Sassano, A., Nikita, K.S., Nicolaides, A.N., 2004. Echogenicity of B-mode sonographic images of the carotid artery. Journal of Ultrasound in Medicine 23, 659–669.

[31] Sonnad, S.S., 2002. Describing data: statistical and graphical methods. Radiology 225, 622–628.

[32] Haralick, R.M., Shanmugam, K., Dinstein, I., 1973. Texture features for image classification. IEEE Transactions on Systems Man and Cybernetics SMC-3, 610-621.

[33] Soh, L.-K., Tsatsoulis, C., 1999. Texture analysis of SAR sea ice imagery using gray level co-occurrence matrices. IEEE Transactions on Geoscience and Remote Sensing 37(2), 780-795.

[34] Clausi, D.A., 2002. An analysis of co-occurrence texture statistics as a function of grey level quantization. Canadian Journal of Remote Sensing 28, 45-62.

[35] Galloway, M.M., 1975. Texture analysis using gray level run lengths. Computer Graphics and Image Processing 4, 172-179.

[36] Tang, X., 1998. Texture information in run-length matrices. IEEE Transactions on Image Processing 7(11), 1602-1609.

[37] Laws, K.I., 1980. Rapid texture identification. SPIE 238, 376-380.

[38] Arivazhagan, S., Ganesan, L., Priyal, S.P., 2006. Texture classification using Gabor wavelets based rotation invariant features. Pattern Recognition Letters 27, 1976-1982.

[39] Manjunath, B.S., Ma, W.Y., 1996. Texture features for browsing and retrieval of image data. IEEE Transactions on Pattern Analysis and Machine Intelligence 18, 837–842.

SOCIETY FOR SCIENCE AND EDUCATION UNITED KINGDOM

JBEMi JOURNAL OF BIOMEDICAL ENGINEERING AND MEDICAL IMAGING

ISSN: 2055-1266
VOLUME 3 ISSUE 1

Development of Plantar-Pressure Estimation Method Based on Continuous Plantar Images

Yuka Iijima, Koji Imai, Takeshi Yamakoshi, Hiroshi Mizoguchi, and Hiroshi Takemura
Department of Mechanical Engineering, Faculty of Science and Technology,
Tokyo University of Science, Tokyo, Japan
7514604@ed.tus.ac.jp

ABSTRACT

We propose a novel plantar-pressure estimation method using high-resolution plantar images. The proposed method can calculate the plantar-pressure distribution, ground reaction force, and center-of-pressure (COP) trajectory based on the weight of a subject, contact-area size, and brightness distribution of a plantar image captured by a high-speed camera. Four experiments are conducted to evaluate the proposed method. First, the relationship between the contact area/pressure condition and brightness distribution of the image is investigated. The result shows that the brightness increases according to the area size under the same pressure condition. Second, the plantar-pressure distribution calculated by the proposed method is compared with that of commercial pressure sensors. The results demonstrate that the plantar-pressure characteristics of the subject even in a small region are unambiguously represented. Third, the ground reaction force estimated by the proposed method is compared with that of the commercial force plate. The root mean square error (RMSE) is 16% of the maximum ground reaction force. The COP trajectory calculated by the proposed method is compared with the result obtained using the force plate. The averages of COP.x and COP.y RMSEs are calculated as 6.0 and 28.6 mm, respectively, which suggest that the proposed method can calculate the pressure distribution, ground reaction force, and COP trajectory. We apply the proposed method to a developed caterpillar-type transparent treadmill and demonstrate that the proposed method can be used for continuous plantar-pressure distribution measurement.

Keywords: Plantar image; Plantar pressure; Brightness distribution; Image processing; CaTTaP

1 Introduction

Plantar-pressure distribution is one of the well-known parameters that many researchers and therapists have been measuring and using for gait evaluation. Many types of plantar-pressure measurement systems have been proposed. The major systems are classified into three types according to the sensing method such as ink, image, or electronic sensor. The ink-type system measures the plantar pressure using the intensity of the static data obtained by walking over a paper with the soles covered with powder [1, 2]. The ink-type system cannot measure dynamic data. The image-type system calculates the plantar-pressure distribution based on the brightness of the grayscale plantar image captured by a camera located under a “barograph device” with a plain glass plate covered with a thin seat of white

DOI: 10.14738/jbemi.31.1866
Publication Date: 22nd February 2016
URL: http://dx.doi.org/10.14738/jbemi. 31.1866

deformable plastic [3]. In spite of the active research in the 1980s, the use of this type did not widely spread because of the spatial/time resolution and camera cost at that time. However, information derived from plantar images serves as a useful, reliable, and objective component in gait analysis. Currana et al. reported the differences between the joint angles of the ankle based on dynamic and static plantar images [4]. Lin et al. constructed a system to investigate the relationship between static balance and foot structure of children using a footprint image [5]. Hawes et al. measured the foot arch from the ratio of a plantar bearing area to the area of the foot arch [6]. Nakajima et al. proposed a method for personal identification based on plantar shape [7]. Shiina et al. suggested a relationship between plantar skin deformation and gait stability based on plantar images [8]. Form the above studies, although plantar image has great potential for analyzing and understanding the gait, methods to obtain the plantar image are seldom used in clinical applications. Today, almost all researchers who analyze plantar-pressure data use electronic sensors. These sensors come in many types such as mat [9], treadmill [10], insole [11], and small three-seal types [11]. However, conventional sensors do not have sufficient resolution to estimate the pressure of small regions such as the toes.

We focus on the resolution of a captured image and propose a new method that clearly estimates the high-resolution plantar-pressure distribution based on a plantar image.

2 Imaging Plantar-Pressure Estimation Method

2.1 Plantar image

We propose a new method that estimates the plantar-pressure distribution using the brightness distribution of a grayscale plantar image “directly” captured during walking (Figure 1) without any seat, in contrast to the conventional methods [3]. The captured image clearly shows the change in the brightness distribution.

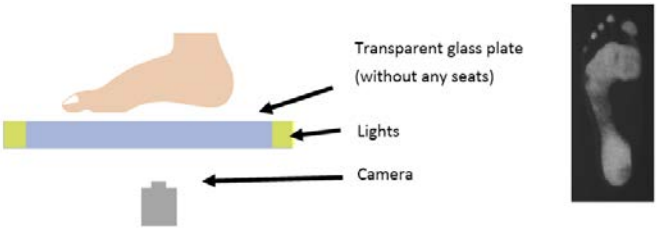

Figure 1 Capture method and the captured image

In the plantar image, the high-pressure area of the heel displays high brightness, whereas the low-pressure area in the arch area displays low brightness. This brightness change occurs because greater pressure causes closer contact between the skin and the glass plate, and the total internal reflection within the glass and the rough skin surface increases (Fig. 2). In a previous research [12], the correlation between pressure and brightness of the plantar contact area was high ($R > 0.9$), and the brightness increased according to the pushed vertical force according to a quadratic function.

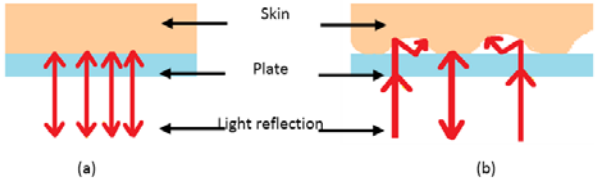

Figure 2 Light reflection of two types. (a) High pressure. (b) Low pressure

2.2 Image processing

To clearly show the brightness distribution of the plantar image, the grayscale images are converted to pseudo colors, as shown in Figure 3.

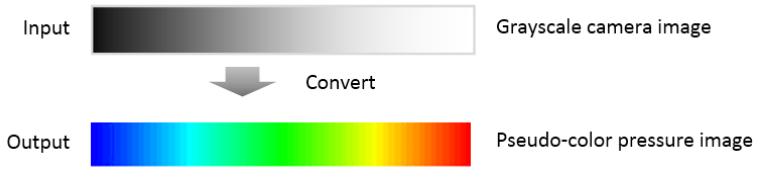

Figure 3 Conversion diagram of the proposed method

To generate a clear pseudo-color image, the brightness of the plantar image is normalized by Equation (1). *Max* and *Min* denote the maximum and minimum brightness of all images. Figure 4 shows the brightness change parameter from the input brightness value to the pseudo-color pressure image.

$$\text{Normalized brightness} = \text{Brightness} * 255/(Max - Min) \quad (1)$$

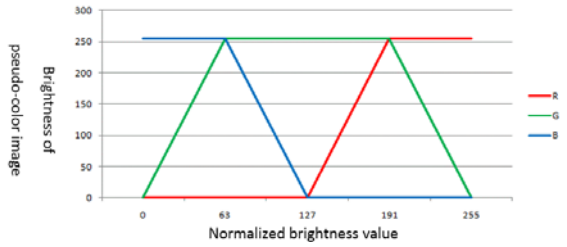

Figure 4 Diagram of the changing RGB channel to generate a pseudo-color image

The pressure on each pixel is calculated as $P(x,y)$ using Equations (2) and (3). (x,y) denotes the coordinate in the anterior–posterior and the medial–lateral axes. *Area* denotes the contact area [pixel], and *Normalized area* denotes the contact area normalized by the maximum size of all data [*Max area* (pixel)]. α and β are weighting parameters to correct the influence of the normalized area and brightness size on the pressure. The total vertical force on the whole sole is calculated using the sum of $P(x,y)$ [expressed by Equation (4)]. *Fz.pm* denotes the force estimated by the proposed method. *Width* and *Height* denote the width and height of the image. The ground reaction force during walking shows bimodal peaks (Fig. 5); two peaks show approximately 110% of the body weight, and the nadir shows approximately 80% of the body weight [13]. By using these characteristics, each of the weighting parameters (α and β) in the first and second terms (shown in Fig. 5) are calculated.

$$p(x,y) = brightness^2 \times \frac{(1 - \alpha \times Normalized\ area)}{\beta} \quad (2)$$

$$Normalized\ area = Area\ /\ Max\ area \quad (3)$$

$$Fz.pm = \sum_{0}^{width} \sum_{0}^{height} brightness^2 \times \frac{(1 - \alpha \times Normalized\ area)}{\beta} \quad (4)$$

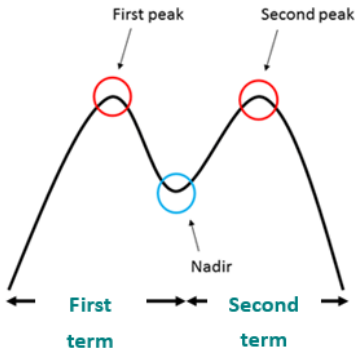

Figure 5 Two terms of the ground reaction force

The center-of-pressure (COP) coordinates are calculated by Equations (5) and (6). (*x*,*y*) denotes the coordinate in the anterior–posterior and the medial–lateral axes.

$$COP.x = \frac{\sum_0^{width} x \times p(x,y)}{\sum_0^{height} \sum_0^{width} p(x,y)} \quad (5)$$

$$COP.y = \frac{\sum_0^{height} y \times p(x,y)}{\sum_0^{height} \sum_0^{width} p(x,y)} \quad (6)$$

3 Estimation Experiments of the Proposed Method

3.1 Experimental device

Figure 6 shows the measurement device to capture the plantar image and measure the force. This device is composed of a camera (Point Grey Research, Inc., GZL-CL-41C6M-C, 2048 × 2048 [pixel], 150 fps), a transparent glass plate, and the force sensors (Tec Gihan Co., Ltd., TF-4060-G, 5000 fps).

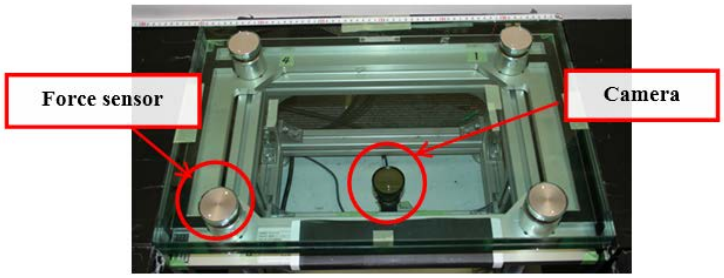

Figure 6 Measurement device (top view)

3.2 Evaluation of the relationship between brightness and contact area

The relationship between the contact area/pressure condition and brightness distribution of the image under the same pressure condition is determined. Three seats made of polyvinyl chloride, whose stiffness is similar to a human heel, are used for the measurement, instead of a human foot. Three types of brightness distribution in same pressure conditions are compared, as shown in Fig. 7, i.e., brightness in the contact area of the following: (1) 10-kg weight on a seat (25 × 66 × 14 mm^3), (2) 20-kg weight on a seat (50 × 66 × 14 mm^3), and (3) 30-kg weight on a seat (75 × 66 × 14 mm^3). The pressed images are captured by the camera located under the plate.

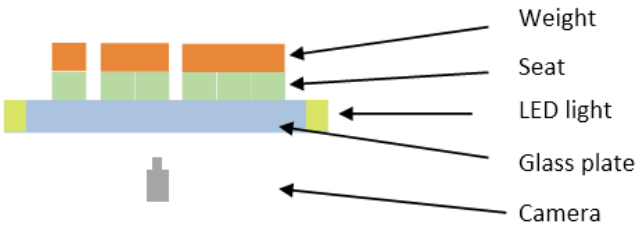

Figure 7 Experimental conditions under the same pressure distribution

Figure 8 shows the trimmed images (size: 50 × 50 pixels) of the seat subjected to the three weight patterns. The brightness averages are calculated as 91, 114, and 128. This result shows that the brightness under the same area pressure increases according to the size of the area.

Figure 8 Part of each seat image

3.3 Evaluation of the plantar-pressure distribution

The plantar-pressure distribution calculated by the proposed method was compared with that of the commercial pressure distribution sensors. Fig. 9 shows the data of the captured images (a), the results of the proposed method (b), and the results of the conventional sensors (LL sensor, Xiroku Inc.) (c).

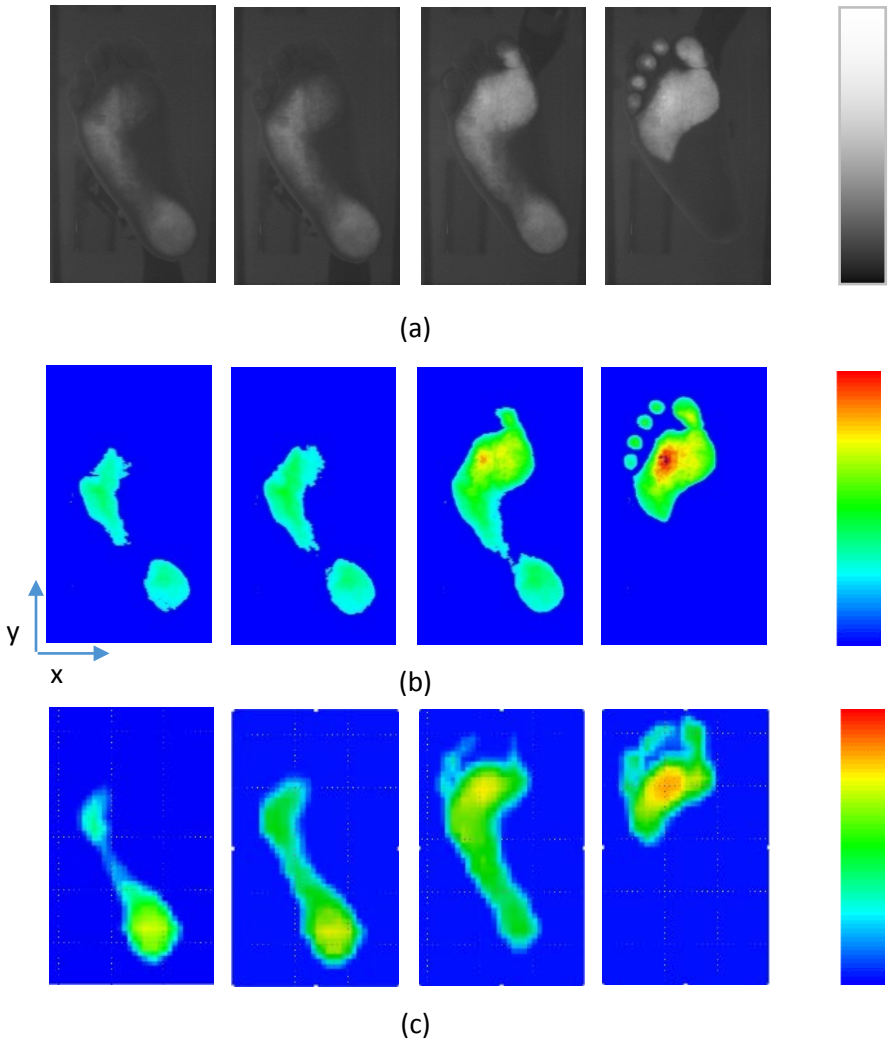

Figure 9 Data of the (a) captured images, (b) results of the proposed method, and (c) results of the conventional sensors

3.4 Accuracy of the ground reaction force

The ground reaction force estimated by the proposed method was compared with that of the commercial force plate. In this experiment, four healthy subjects (Ave. 23.0 $\pm$ 2 years old) were recruited, and 5400 clear plantar images were obtained during walking. Fig. 10 shows the ground reaction force measured by the force sensor (*Fz.fp*) and the proposed method (*Fz.pm*) for a subject. *Fz.pm* indicates the characteristic of bimodal peaks for *Fz.fp*. The average root mean square error (RMSE) calculated by comparing *Fz.pm* and *Fz.fp* is 16%.

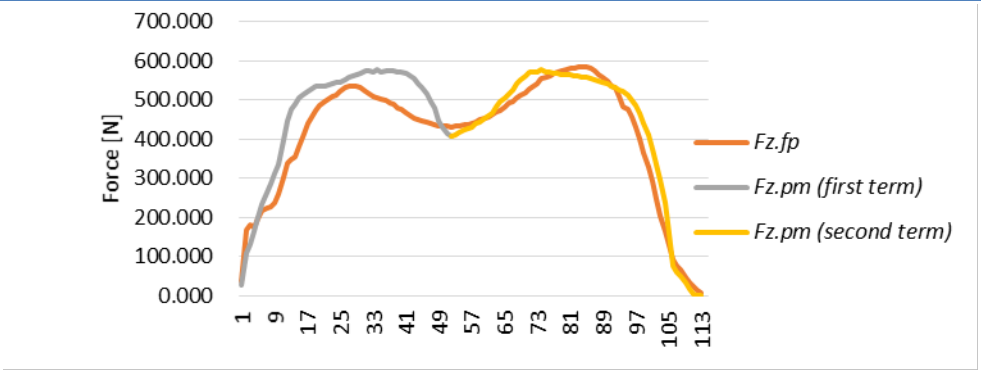

Figure 10 Forces measured by the force plate and the proposed method

3.5 Accuracy of COP

The COP trajectory calculated by the proposed method was compared with that calculated using the force plate. Fig. 11 shows the RMSEs and standard deviation of the COP calculated using the force sensors and the proposed method. The average *x*-axis RMSE is 6.0 mm, and the average *y*-axis RMSE is 28.6 mm. These results show that the accuracy of the COP calculation does not depend on the arch type.

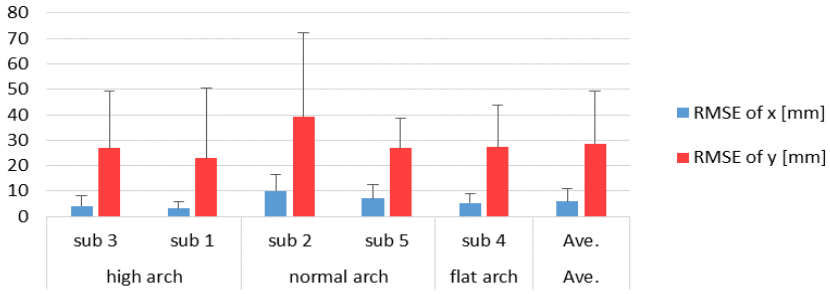

Figure 11 RMSEs of the COP for each subject

Figure 12 shows the plantar image in the high-accuracy (a) and low-accuracy (b) groups of the calculated COP. The contact area in the image in the high-accuracy group is clearer than that in the low-accuracy group. These images suggest that the accuracy of the proposed method depends on the condition of the sole.

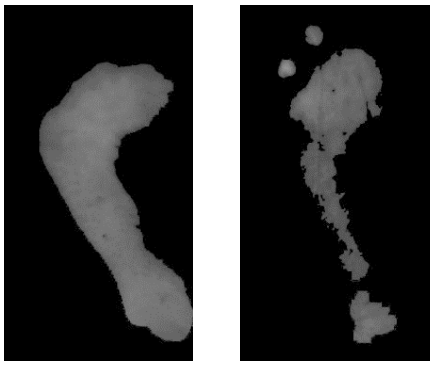

Figure 12 Plantar images of the (a) high- and (b) low-accuracy groups

4 Discussion

The first experiment proved the necessity of correcting the pressure expression by the normalized area. The second experiment showed that the pressure distribution calculated by the proposed method is quantifiably similar to that calculated by the conventional electronic sensor system. The image provided higher resolution data (approximately 4900 pixels/cm^2 depending on the image sensor of the camera) than the pressure distribution sensor (one sensing detector/cm^2). The results show that the pressure distribution in the small region such as toes, which cannot be calculated by the existing sensor [the highest resolution of commercial pressure distribution sensing system: four sensing detector/cm^2 (F-scan II, Nitta Co.)] can be calculated by the proposed method. Such high resolution makes the analysis of a floating-toe walk easier. The third experiment showed that the average RMSE in calculating the force is 16% of the maximum force. Compared with the 10% accuracy of the force plate, the proposed method needs further improvement. However, the contact area and plantar pressure, which cannot be measured by the force plate, can be measured by the proposed method. The last experiment showed that the average RMSE of the COP does not depend on the arch but on the condition of the sole of the subject. According to the experimental results, images in a normal condition and a changed condition (such as soft skin by bathing the sole of the subject in tepid water for 5 min) are captured and compared in terms of the contact area. Fig. 13(a) shows the image in a normal condition, and Fig. 13 (b) shows the image in a soft condition. In Fig. 13(c), the light blue, dark blue, and pink regions show each area listed in Table 1. Fig. 13(c) and Table 1 show that the soft sole is captured much clearer than the hard one because the accuracy of the proposed method also depends on the sole condition of the subject. This result suggests that softening the sole of the subject by footbath is one of the best ways to make the proposed method more accurate.

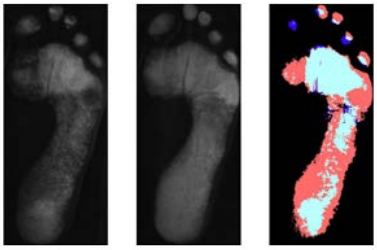

Figure 13 Plantar images of (a) normal condition, (b) soft condition, and (c) comparison result

Table 1 Area ratio in each region

	A contact and B contact	49.6 %
	A contact and B non-contact	3.3 %
	A non-contact and B contact	51.5 %

In addition, we developed a new system to analyze the gait using a new treadmill—the caterpillar-type transparent treadmill (CaTTaP) [14] (as shown in Fig. 14)—that continuously captures plantar images

during walking. Using the CaTTaP, gait parameters such as step length, step width, plantar skin deformation, contact area, and sole shape are calculated based on the clear dynamic plantar images at any steps, which are difficult to obtain using other devices. Application of the proposed method to CaTTaP (as shown in Fig. 15) makes the estimation of continuous plantar-pressure distribution available for any steps.

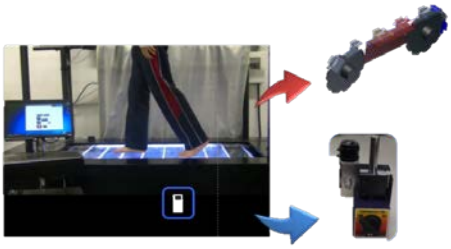

Figure 14 CaTTaP

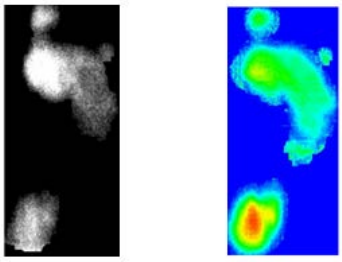

Figure 15 Images by CaTTaP. (a) Original image and (b) pseudo-color pressure image by the proposed method

5 Conclusion

This paper presented a novel plantar-pressure estimation method using high-resolution plantar images. The proposed method can calculate the plantar-pressure distribution, ground reaction force, and COP trajectory based on the weight of a subject, size of the contact area, and brightness distribution of the plantar image captured by a high-speed camera located under a transparent glass plate. Four experiments were conducted to evaluate the proposed method, and the results suggested that the proposed method can potentially calculate the pressure distribution, ground reaction force, and COP trajectory with high accuracy. We applied the proposed method to the developed CaTTaP and demonstrated that it is available for continuous plantar-pressure distribution measurement. We confirmed that CaTTaP is one of the best gait analysis systems available for clinical use.

REFERENCES

[1] Masahito, A., et al., *A gait analysis system using foot path images*, Journal of the Japan Society for Precision Engineering, 2008. 74(12). p. 1318–1324.

[2] Silvino, N., et al., *The Harris and Beath footprinting mat: Diagnostic validity and clinical use*, Clinical Orthopaedics and Related Research, 1980. 151: p. 265–269.

[3] Betts, R.P., et al., *Critical light reflection at a plastic/glass interface and its application to foot pressure measurements*, Journal of Medical Engineering and Technology, 1980. 4(3) : p. 136-142.

[4] Currana, S.A., et al., *Dynamic and static footprints: Comparative calculations for angle and base of gait*, The Foot, 2005. 15(1): p. 40–46.

[5] Lin, C.H., et al., *Development of a quantitative assessment system for correlation analysis of footprint parameters to postural control in children*, Physiological Measurement, 2006. 27(2): p. 119–130.

[6] Hawes, M.R., et al., *Footprint parameters as a measure of arch height*, Foot Ankle, 1992. 13(1): p. 22–26.

[7] Nakajima, K., et al., *Footprint-based personal recognition*, IEEE Transactions on Biomedical Engineering, 2000. 47(11): p. 1534–1537.

[8] Shiina, T., et al., *Measurement of undetectable walking feature by appearance based on plantar skin deformation*, The 15th International Conference on Biomedical Engineering, 2013. p. 116–119.

[9] Middleton, L., et al., *A floor sensor system for gait recognition*, Automatic Identification Advanced Technologies, 2005. 5(7): p. 171–176.

[10] Alon, K., et al., *Quantifying gait impairment using an instrumented treadmill in people with multiple sclerosis*, Hindawi Publishing Corporation ISRN Neurology, 2013. Article ID 867575, 6 pages.

[11] Peter, R., et al., *In-shoe plantar pressure measurement: A review*, The Foot, 1992. 2(4): p. 185–194.

[12] Yuka, I., et al., *Measurement of plantar pressure distribution based on grayscale plantar images*, The 8th Asian-Pacific Conference on Biomechanics, 2015. PS8-1.

[13] Jacquelin P., et al., *Gait analysis: Normal and pathological function*, Slack Inc. (2010).

[14] Yuka, I., et al., *Development of gait analysis system based on continuous plantar images obtained using CaTTaP device*, Advanced Biomedical Engineering, 2015. 4(0): p. 119–125.

SOCIETY FOR SCIENCE AND EDUCATION UNITED KINGDOM

JBEMi JOURNAL OF BIOMEDICAL ENGINEERING AND MEDICAL IMAGING

ISSN: 2055-1266
VOLUME 3 ISSUE 1

In vivo Tumor Spatial Classification using PCA and K-means with NIR-Hyperspectral Data

[1]Mai Kasai, [2]Yuya Yasuda, [1]Hiroshi Takemura, [1]Hiroshi Mizoguchi, [2]Kohei Soga, and [3]Kazuhiro Kaneko
[1]Faculty of Science and Technology, Tokyo University of Science, Japan;
[2]Faculty of Industrial Science and Technology, Tokyo University of Science, Japan;
[3]National Cancer Center Hospital East, Japan;
7515613@ed.tus.ac.jp

ABSTRACT

This paper presents new method of spatial classification and wavelength bands reduction of near-inferred (NIR) hyperspectral imaging data for medical application. Hyperspectral imaging data have more than several hundred wavelength bands. However hyperspectral data have sometimes redundant information to detect region of interest. The aim of this research is to archive became possible that a region of interest is distinguished by observing the particular wavelength bands without any markers in order to develop a special application such as a surgery supporting system. NIR light with wavelengths of 800-2000 nm, called as the 'biological window,' has received particular attention given that water and biological tissues have minimal optical loss caused by scattering and absorption at these wavelengths. NIR light can penetrate/see through deep tissues. NIR endoscope have a great potential as the surgery supporting system, however wavelength bands needs to reduce according to the limitation of NIR endoscope hardware performance. To consider only several wavelength bands are sometimes much effective case than to consider all wavelength bands. In this paper, we proposed the method of spatial classification and reduction a number of wavelength bands simultaneously by combined PCA and k-means, and assessed the cancer-caring nude mouse. The experimental results demonstrate that the proposed method can select valuable wavelength bands to distinguish the region of interest with comparable accuracy of the conventional method.

Keywords: Spatial Classification, PCA, k-means, Hyperspectral data, Near-Infrared

1 Introduction

Hyperspectral imaging is a combination of imaging and spectroscopic technology [1]. Hyperspectral imaging data have more wavelength bands than RGB images taken by the ordinary RGB camera. Each pixel of hyperspectral imaging has a spectrum data. Differences that appear subtle to the human eye could be significant when looking at the detailed spectrum. Hyperspectral imaging data is utilized in several fields: remote sensing, biological engineering, agriculture, food engineering, and so on. In the medical field, a region of interest (ROI) means an image area required at a diagnosis [2-3]. If it became possible that ROI of a nerve or a lesion part is distinguished by observing the particular wavelength bands without any markers, a special application as a surgery supporting system is realized. Near-inferred light (NIR) imaging has such a potential. NIR light with wavelengths of 800-2000 nm, called as

DOI: 10.14738/jbemi.31.1892
Publication Date: 27th February 2016
URL: http://dx.doi.org/10.14738/jbemi. 31.1892

the 'biological window,' has received particular attention given that water and biological tissues have minimal optical loss caused by scattering and absorption at these wavelengths. NIR light can penetrate/see through deep tissues. NIR endoscope have a great potential as the surgery supporting system [4-5], however, hyperspectral data have sometimes redundant information to detect region of interest. To consider only several wavelength bands are sometimes much effective case than to consider all wavelength bands. And wavelength bands need to reduce according to the limitation of NIR endoscope hardware performance.

There are many analysis techniques to detect the ROI. These include Gabor filter, grey level co-occurrence matrix (GLCM), principle component analysis (PCA), minimum noise fraction (MNF), wavelet transform, etc. [6-10]. Multitude studies apply the analysis of a machine leaning method using all of wavelength bands, spectral peak and extracted features. To distinguish the ROI from enormous multidimensional data by using a conventional machine learning method, it is necessary to acquire a large amount of the dataset. However the collecting vast quantities of information on medical field such as rare intractable diseases is very hard. This is because that the conventional machine learning method is difficult to apply directory to the medical application. Additionally, hyperspectral images have redundant information about an object, and often require application of dimensionality reduction methods such as PCA to remove the redundant information. One example, Naganathan et al. [11] develop and test hyperspectral imaging system to predict tenderness of beef from hyperspectral images. This method combined PCA, GLCM and canonical discriminant analysis (CDA). Combined with these methods, this analysis technique is implemented to extract features from the hyperspectral images. However this method cannot be applied to unknown sample of composition and spectrum. On the other hand, k-means clustering [12-13] is the analysis to distinguish the ROI without the machine learning. Hyperspectral data, however, have sometimes redundant information not to enhance more accuracy using only k-means. To consider only several wavelength bands are sometimes much effective case than to consider all wavelength bands. The wavelength bands need to reduce according to an application of NIR endoscope, combined with the NIR-fluorescent imaging system [14].

We propose the method of spatial classification for a tumor and reduction a number of wavelength bands simultaneously. By combining PCA [15] and k-means clustering, we visualize the analyzed results and reduce wavelength bands based on a factor loading value of PCA. The proposed method applies the tumor region of the cancer-caring nude mouse distinguish experiments. In the experiments, the selected wavelength bands calculated by the proposed method is performed favorable behavior compared to original ROI calculated by all wavelength bands.

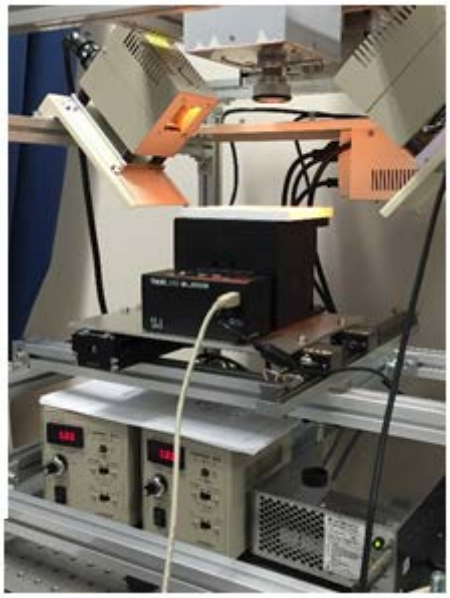

Figure 1. Compovision®(Sumitomo Electric Industries, Ltd., CV-N800HS).

2 Proposed Methods

Figure 1 shows the NIR-hyperspectral imaging camera, Compovision (Sumitomo Electric Industries, Ltd., CV-N800HS) using in this study. The wavelength resolution of the Compovision is approximately 6nm from 913.78 to 2522.44 nm, and this is a line scan camera, 320 pixel par line. Each pixel has 256 wavelength bands. The flowchart of the proposed method is shown in Figure 2. The proposed method is mainly composed of the following six process.

2.1 Preprocessing

The purpose of preprocessing is to calibrate and reduce noise of the captured hyperspectral imaging data. Each pixel of hyperspectral imaging data is converted to 234 wavelength bands from 256. The first 11 bands and the last 11 bands do not use for the analysis due to low signal to noise ratio. As a reflectance calibration, original data *V* is corrected from the dark and white data of the camera. The dark data *D*, obtained by turning off the light and covering the lens with a lens cap, is the background response of camera. The white data *W* is obtained with the standard reflector, which is not absorption in near-infrared wavelength bands to correct a wavelength sensitivity characteristic by the camera and light. Corrected reflectance value *f* is calculated as follows:

$$f = \frac{V - D}{W - D} * 65535 \quad (1).$$

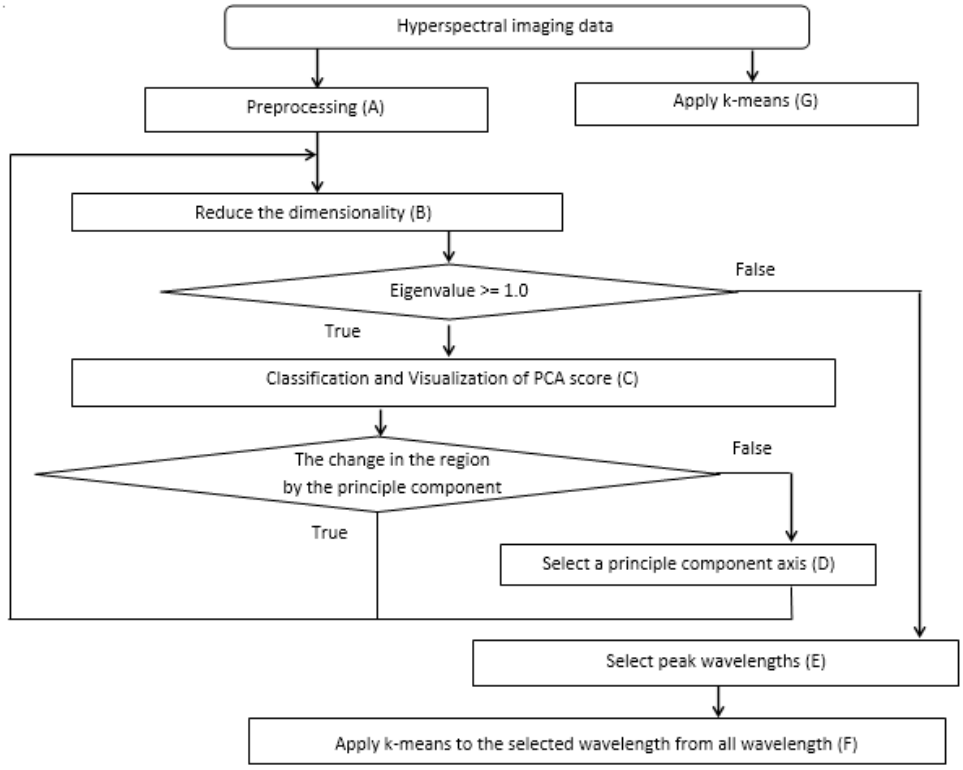

Figure 2 Flow chart of the proposed method

2.2 Reduce the dimensionality (by PCA)

The multi-dimensional wavelength bands are reduced by PCA as information content is maintained. PCA is a technique of multivariate analysis that reduces the dimensionality. PCA has been utilized to reduce dimension, extract feature, compress data, and identify key factor. If an eigenvalue of PCA is more than 1.0, the PCA score are classified and visualized as the result image calculated by using k-means clustering.

2.3 Classify and Visualize of PCA score (by k-means)

K-means clustering is a representative technique as a partitioned optimization clustering technique that search optimal partition by an evaluation function. PCA score is divided into some cluster by similarity on principle component axis. The evaluation function is defined by

$$E = \sum_{i=1}^{k} \sum_{x \in c_i} (dist(\boldsymbol{x}, \boldsymbol{c}_i))^2 \tag{2}$$

Where $\boldsymbol{x}$ is PCA score calculated by (B), k is number of clusters, $\boldsymbol{c}_i$ indicates centroid points of each cluster, and $dist(\boldsymbol{x}, \boldsymbol{c}_i)$ measures the Euclidean distance between a pattern $\boldsymbol{x}$ and its cluster centroid point $\boldsymbol{c}_i$. PCA score is partitioned into k clusters to minimize value of the function E. Each cluster is distinguished and described on the 2D image, which captured with the hyperspectral image data at the same time, by using different colors to visualize clustering results.

2.4 D. Select the principle component axis

The proposed method need to select a principle component axis to visualize k-means clustering results. PCA continues to apply to the captured hyperspectral image data until an eigenvalue of PCA is less than 1.0 or a cumulative contribution ratio of PCA are more than 99.98 %. An integer number of n is defined as maximum number of principal components at this time. The k-means clustering result images of PCA are calculated based on each principal component from 1 to n, respectively. If a different between the clustering result image of i th and $i+1$ st principal components is more than a threshold, $i+1$ st principle component that contained feature information to divide image region is selected. If the region of the result image does not change as a whole, all n th principle components are selected.

2.5 Select peak wavelength bands

The peak wavelength bands are selected as significantly peak values of respective axis according to a loading factor value as the following equation.

$$\begin{cases} \text{if} & (\sigma_m^2 > 0.8 * \sigma^2 \text{ or } \mu < 0.2 * max) \\ & \text{Select the wavelength bands.} \\ & \left(\text{satisfied the conditions that loading factor value takes more than max*0.95} \right) \\ \text{else} & \text{Don't select the wavelength band.} \end{cases} \quad (3)$$

Where σ^2 is the dispersion of loading factor, σ_m^2 is the dispersion of loading factor from the third-quartile to maximum value (*max*), and μ is average value of loading factor. In PCA, the loading factor indicates the correlation between the principle component and the identified the factor that affects each principle component. Loading factors value of the selected principle component is compared and extracted the peak wavelength bands as feature values. If the loading factor value does not show the significantly peak, the loading factor is regarded as no factor that concerned principle component strongly and extracted as no wavelength from this axis. Regarding the peak wavelength bands of the loading factor value in selected principle component axis by changed region, the required feature values are extracted to discriminate particular region from multidimensional and enormous informative data. The results are evaluated by an error between the correct answer data.

Figure 3. Pseudo-color image of the target. Orange area show the tumor area.

2.6 Apply k-means clustering to the selected wavelength bands from all wavelength bands.

This section describes visualizing evaluating of the proposed method. The reduced data only selected wavelength bands are applied k-means clustering. The analyzed results are visualized by the 2D image. The original data (234 wavelength bands) is applied k-means clustering similarly for comparison. The result using all wavelength bands (G) is compared with the result of the proposed method using the selected wavelength bands (F) for evaluation. The total number of pixels of a target ROI where is deciding comparison objective region manually calculated as the correct answer data. The visualized target ROI is calculated by the proposed method and compared in the result images.

3 Evaluation Experiment

3.1 Experimental Condition

The proposed method is applied to distinguish by the tumor of mains. The target is the cancer-caring nude mice. This study received ethics committee approval of Tokyo University of Science. We acquired the hyperspectral image data that is 320 (pixels per line) x 234 (wavelength bands per pixel) x 720 (number of lines) and the resolution is about 0.10[mm^2/pixel]. One image data is less than 2-3 [s] to scan. The mouse mask binary imaging data is generated by using the brightness value of 1394.64 nm. Pseudo-color image of the cancer-caring nude mouse shows in Figure 3. Orange area indicate the tumor area.

3.2 Cross-Validation Method

The proposed method selects the wavelength bands as feature values using changing area by visualize PCA score. The usability of selected wavelength bands from a mouse is assessed to apply the selected wavelength bands to other mouse data. The distinguished area that is acquired applying the data of selected wavelength bands to k-means clustering is compared with the ROI area in visible image and evaluated by Equation (2).

$$\text{Sensitivity} = \frac{distinguished\ area\ [pixel]}{target\ area\ [pixel]}$$
$$\text{Specificity} = \frac{not\ distinguished\ area\ [pixel]}{not\ target\ area\ [pixel]} \quad (2)$$

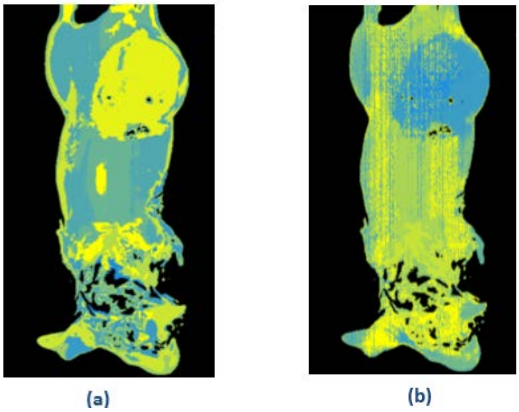

(a) (b)

Figure 4. Results of distinguished area by k-means. Result using all wavelength bands data (a), Result using only selected wavelength bands data (b)

4 Results

The results of distinguished area by k-means show Figure 4. The result using all wavelength data is Figure 4-(a) and using only selected wavelength bands data is Figure 4-(b). The sensitivity and specificity of the all results area are calculated by comparing with the visible image of tumor area (Figure 3). In Table 1, "Mouse 1" is target data used to select the wavelength bands and the sensitivity and specificity are calculated by using other mics. "ALL" is the results using all wavelength bands data, and "SELECT" is the results using only the selected wavelength bands data. The 2, 3, 5, 13, 18th principle components and seven wavelength bands are selected by the proposed method. The sensitivity and specificity of the selected wavelength bands data differs little from that of the all wavelength bands data. The original data are reduced to only seven wavelength bands from 234 wavelength bands. The selected wavelength bands as the feature values of each mouse by the proposed method are the same wavelength bands by coincidence.

Table 1. Error Identification Rate

		"Mouse 1"	"Mouse 2"	"Mouse 3"	"Mouse 4"	Average
Sensitivity	ALL	0.87	0.24	0.75	0.57	0.61
	SELECT	0.86	0.27	0.77	0.55	0.61
Specificity	ALL	0.77	0.86	0.93	0.94	0.88
	SELECT	0.85	0.81	0.83	0.87	0.84

5 Discussion

5.1 Reduce the wavelength bands

The approach of extracting feature value by PCA is the major method in data analysis research field. However the selected feature by PCA tend to extract the more salient and major difference feature.

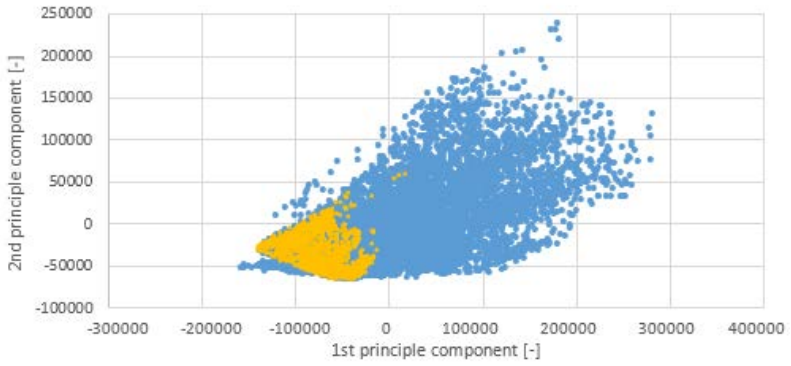

Figure 5. Distribution of principle component scores. The horizontal axis is 1st principle component and the vertical axis is 2nd principle component. Orange color plots show the tumor area and blue color plots show other area (Fig. 3.).

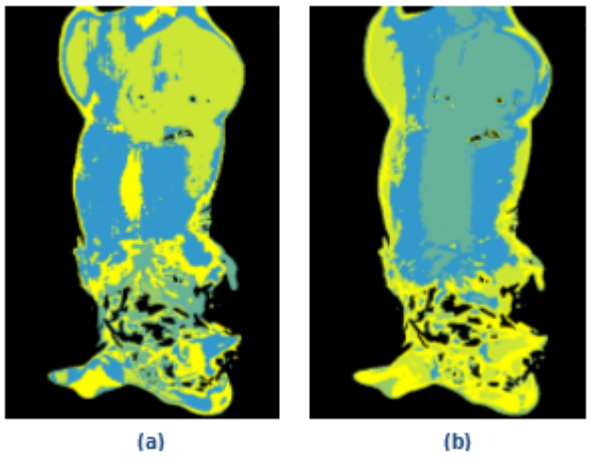

Figure 6. Result image only using the 1st (a) and 2nd (b) principle component data respectively.

Extracting the small/ minor difference in similar properties area, it is difficult to select the principle component axis only. Figure 5 shows the distribution of PCA score between 1st and 2nd principal component axis. The vertical axis is 1st and the horizontal axis is 2nd principle component axis. Orange dots indicate the tumor area and blue dots indicate other area every 10 [pixel]. Figure 5 shows that the tumor area is difficult to distinguish from other area of mouse using only the 1st and 2nd PCA scores. In particular, the tumor area is divided due to the 1st principle component. The distinguished results show at Figure 6 using only the 1st and 2nd principle component, respectively. The results indicate that the 1st and 2nd principle component has keep information (the cumulative contribution ratio of 1st and 2nd principal component is more than 99.98%), however, has redundant information to distinguish the tumor area.

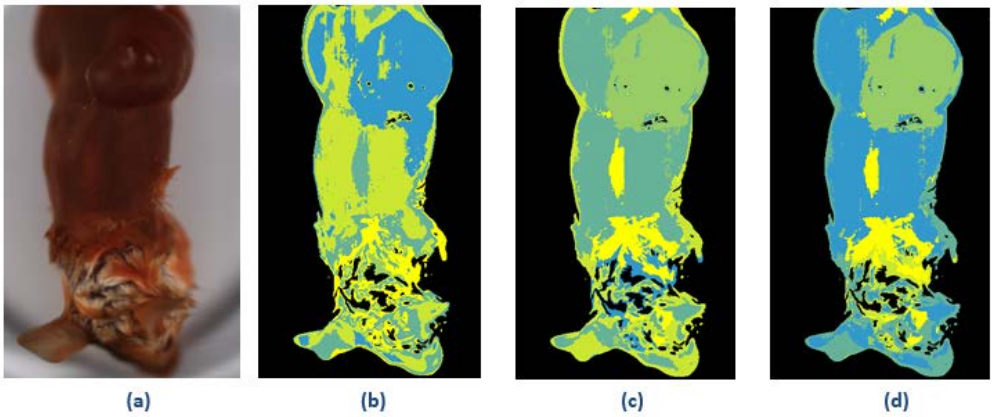

Figure 7. Images show changing the distinguished result by the number of reduced dimensions. (a) shows the Pseudo-color image, (b)~(d) show the result area 2th ~ 4th principle components.

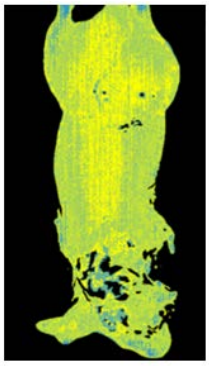

Figure 8. Result image using only the 3rd principle component axis

The proposed method can select the principle component axis focusing on the identification result area depend on small/minor difference feature, not salient/major difference feature. Changing the distinguished result by the number of reduced dimensions show in Figure 7-(b) ~ (d). When compared the result area between 2th ~ 4th principle components, 3th principle component axis is selected because the difference of area of Figure 7-(b) ~ (d) is depended on 3th axis. However change at area having no connection with ROI is ignored. The wavelength bands is selected to distinguish the ROI by the factor loading value of every principle component axis. However, when the dispersion of the factor loading value is more than 0.8, a wavelength bands is not selected. Figure 8 shows the factor loading of 3th principle component axis. The 2, 3, 5, 13, 18th principle component axis, and seven wavelength bands are selected. This result suggested that the 3th axis has useful information to distinguish of the tumor area. This flow is had done until satisfied the conditions that a cumulative contribution ratio of PCA takes more than 99.98% and the principal component axis is selected.

5.2 Investigate the selected wavelength bands

The selected wavelength bands is used to investigate for other mouse data. The imaging conditions is the same and target is other mouse's tumor. Table 1 shows the distinguished result using the selected wavelength bands data by the proposed method. The data of 2~4 mouse except the mouse used to select the wavelength bands is acquired, and same as "Mouse 2", "Mouse 3" and "Mouse 4," respectively. In the case of "Mouse 1" used to select wavelength bands, the result area is distinguished with high precision than using all of wavelength bands data. In the case of "Mouse 2", discrimination precision is low. However in the "Mouse 2~4", the difference of the sensitivity and specificity is small compared with the case of using all of wavelength bands. Necessary information can be extracted to distinguish the ROI.

6 Conclusion

This paper proposed the method of spatial classification and reduction a number of wavelength bands to distinguish the region of tumor by combined PCA and k-means. The proposed method can select the valuable principle component axis focusing on the identification result area depend on changing the number of dimensions reduced by PCA to extract the feature in resemblance area, not large /major difference feature. The proposed method also select the wavelength bands as the feature value using the factor loading value of the each selected principal component axis. The selected wavelength bands are assessed by data of four tumor mouse by compared with the all wavelength bands. Applying the

selected wavelength bands to the mouse average sensitivity is 0.61, and applying the all wavelength bands average sensitivity is 0.61. The specificity of seven wavelength bands distinguished is 0.84. Although there is not large difference comparing with using all of wavelength bands (0.88), the proposed method can reduce dimension and select only seven wavelength bands from 234 wavelength bands. The proposed method is effective for the situation that the composition and spectrum of the target is unknown. To select the wavelength bands has valuable information using the proposed method, learning analysis applies the hyperspectral data of unknown subject efficiently.

REFERENCES

[1]. Schultz R. A., Nielsen T., Zavaleta J. R., Ruch R., Wyatt R., Ganner H. R., Hyperspectral Imaging: A Novel Approach For Microscopic Analyasis, Cytometry, Vol. 43, Issue 4, 2001, pp. 239-247.

[2]. Guolan Lu, Baowei Fei, Medical hyperspectral imaging: a review, Journal of Biomedical Optics, Vol. 19(1), 2014, 010901.

[3]. Guolan Lu, Luma Halig, Dongsheng Wang, Zhuo Georgia Chen, and Baowei Fei, Hyperspectral Imaging for Cancer Surgical Margin Delineation: Registration of Hyperspectral and Histological Images, Proc SPIE. NIH Public Access Author Manuscript, 2014, No. 92036, pp.1-11.

[4]. Zako T., Ito M., Hyodo H., Yoshimoto M., Watanabe M., Takemura H., Kishimoto H., Kaneko K., Soga K., Maeda M., Extra-iluminal detection of assumed colonic tumor site by near-infrared laparoscopy, Surgical Endoscopy, 2015, pp. 1-7.

[5]. Zako T., Hyodo H., Tsuji K., Tokuzen K., Kishimoto H., Ito M., Kaneko K., Maeda M. and Soga K., Development of near infrared-fluorescent nanophosphors and applications for cancer diagnosis and therapy, Journal of Nanomaterials, 2010 , Vol. 2010, pp.1-7.

[6]. Amgren M., Hansen PW., Eriksen B., Larsen J., Larsen R., Analysis of Pregerminated Barley using Hyperspectral Image Analysis, Journal of Agricultural and Food Chemistrt, Vol. 59, 2011, pp. 11385-11394.

[7]. Yaguchi A., Kobayashi T., Watanabe K., Iwata K., Hosaka T., Out N., Cancer Detection From Biopsy Images using Probabilistic and Discriminative Features, 2011 18th IEEE International Conference on Image Processing (ICIP), 2011, pp. 1609-1612.

[8]. Serranti S., Cesare D., Marini F., Bonifazi G., Classification of oat and groat kernels using nir hyperspectral imaging, Talanta, Vol. 103, 2013, pp. 276-284.

[9]. Okamoto, H., Murata, T., Kataoka, T. and Hata, S., Plant classification for weed detection using hyperspectral imaging with wavelet analysis, Weed Biology and Management, 2007, Vol. 7, pp.31-37.

[10]. Jeng-Ren Duann, Chia-Ing Jan, Mnang Ou-Yang, Chia-Yi Lin, Jen-Feng Mo, Yung-Jiun Lin, Ming-Hsui Tsai, Jin-Chern Chiou, Separation spectral mixtures in hyperspectral image data using independent component analysis: validation with oral cancer tissue sections, Journal of Biomedical Optics, 2013, Vol. 18, No. 12, 126005.

[11]. Naganathan G. K., Grimes L. M., Subbiah J., Calkins C. R., Samal A., Meyer G. E., Visible/Near-infrared Hyperspectral Imaging for Beef Tenderness Prediction, Computers and Electronics in Agriculture, Vol. 64, 2008, pp. 225-233.

[12]. MacQueen J., Some methods for classification and analysis of multivariate observations, Proceedings of the fifth Berkeley Symposium on Mathematical Statistics and Probability, Vol. 1: Statistics, 1967, pp. 281-297.

[13]. Wagstaff K., Cardie C., Rogers S., Schroedl S., Constrained K-means Clustering with Background Knowledge, Proceedings of the Eighteenth International Conference on Machine Learning, 2001, pp. 577-584.

[14]. Komoriya K., Takemura H., Mizoguchi H., Soga K., Hyodo H., Kishimoto H., Kaneko K., NIR-fluorescent Imaging by Head-Scanning Mechanism for Near-Infrared Endoscope, Transaction of Japanese Society for Medical and Biomedical Engineering, Vol. 51, No. 2, 2013, pp.135-141.

[15]. Peason K., On lines and planes of closest fit to systems of point in space, Philosophical Magazine, Vol. 2, 1901, pp.559-572.

SOCIETY FOR SCIENCE AND EDUCATION UNITED KINGDOM

JBEMi JOURNAL OF BIOMEDICAL ENGINEERING AND MEDICAL IMAGING

ISSN: 2055-1266
VOLUME 3 ISSUE 1

Noise Removal and Contrast Enhancement for X-Ray Images

[1]Ren-You Huang, [2]Lan-Rong Dung, [3]Cheng-Fa Chu and [4]Yin-Yi Wu
[1]Institute of Electrical Control Engineering, National Chiao Tung University, Taiwan;
[2,3]Department of Electrical and Computer Engineering, National Chiao Tung University, Taiwan;
[4]National Chung-Shan Institute of Science and Technology, Taiwan;
hry76519@gmail.com; lennon@faculty.nctu.edu.tw; cfc310186.eed00g@nctu.edu.tw;
davidwu0801@gmail.com

ABSTRACT

X-ray image plays a very important role in the medical diagnosis. To help the doctors for diagnosis of the disease, some algorithms for enhancing X-ray images were proposed in the past decades. However, the enhancement of images will also amplify the noise or produce distortion of image, which are unfavorable to the diagnosis. Therefore, appropriate techniques for noise suppression and contrast enhancement are necessary. This paper proposed an algorithm including two-stage filtering and contrast enhancement for X-ray images. By using adaptive median filter and bilateral filter, our method is able to suppress the mixed noise which contains Gaussian noise and impulsive noise, while preserving the important structures (e.g., edges) in the images. Afterwards, the contrast of image is enhanced by using gray-level morphology and contrast limited histogram equalization (CLAHE). In the experiments, we evaluate the performance of noise removal and contrast enhancement separately with quantitative indexes and visual results. For the mixed noise case, our method is able to achieve averaged PSNR 39.89 dB and averaged SSIM 0.9449; for the contrast enhancement, our method is able to enhance more detail structures (e.g., edges, textures) than CLAHE.

Keywords: Medical Image Processing; Noise Reduction; Contrast Enhancement; X-ray images.

1 Introduction

X-ray imaging has been widely used in the real-world applications, for instance, medical diagnosis, customs inspection. The X-ray images are especially common way to aid the doctors in diagnosing the diseases of patients. The proper visual characteristics which determine the quality of X-ray images are density and contrast [1]. However, the contrast of X-ray images is usually low, which may influence the doctors' diagnosis. Besides, the noises that accompany the low contrast X-ray images will also degrade the image quality. In the following, we will briefly review the classical methods of noise removal and contrast enhancement.

The previous works applied different denoising methods for different noise types. For example, using Gaussian filter [2], anisotropic diffusion [3-5], or bilateral filters [6, 7], to deal with the Gaussian noise; or using median filters [8-11] to deal with the impulsive noises (like salt and pepper), which are produced by corrupted pixels. The Gaussian filter is a kind of mean filter with the Gaussian distributed weightings instead of equal ones. The anisotropic diffusion solves the partial differential equation iteratively. The

DOI: 10.14738/jbemi.31.1893
Publication Date: 29th February 2016
URL: http://dx.doi.org/10.14738/jbemi. 31.1893

bilateral filter computes the distance weight and similarity weight of the pixels in the filter window. Both the anisotropic diffusion and bilateral filter can preserve the edges while reducing the noise. The median filter is a non-linear filter which replaces the center pixel with the median value within the filter window.

To enhance the contrast of images, typical methods are based on the histogram equalization [12-22]. The histogram equalization enhances the contrast by remapping the intensity of the images from original distributions to the more uniform ones [12-14, 17, 18]. However, using histogram equalization may amplify the noise at the same time. Moreover, for some images with uniformly distributed histogram, the histogram equalization will show limited enhancement of the contrast. The adaptive histogram equalization can enhance the local contrast, which is more robust to the noise than the histogram equalization, and is able to obtain more visually satisfactory results [15, 19-22].

Recent works show impressive results of medical image enhancement [3, 23, 24]. Yang et al. [23] proposed an approach based on wavelet transform for medical image enhancement. Vibhakar et al. [24] applied five widely used techniques to enhance the medical images, including spatial domain filtering, frequency domain filtering, histogram processing, morphological filtering and wavelet-based filtering. Kurt et al. [3] proposed a hybrid algorithm which includes mathematical morphology, anisotropic diffusion filter and contrast limited adaptive histogram equalization (CLAHE).

This paper proposed an algorithm for X-ray image enhancement which can reduce the mixed noises and enhance the contrast. We first remove the impulsive noise by adaptive median filter, which are only applied to the pixels detected as impulsive noises. The bilateral filter is applied to the image to reduce the Gaussian noises. Then, we perform two gray-level morphology techniques (top-hat and bottom-hat transform) to the image, followed by the CLAHE algorithm, to enhance the contrast of the image.

2 The Proposed Method

Figure 1 shows the flow chart of the proposed algorithm, which includes: adaptive median filter, bilateral filter, mathematical morphology, and contrast limited histogram equalization. The details of each part are described in the following subsections.

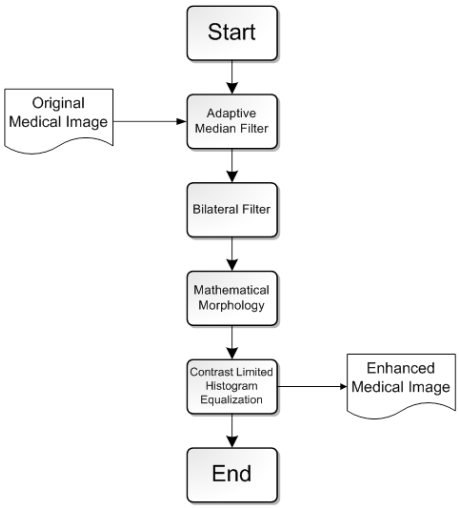

Figure 1. The processing flow of the proposed algorithm.

2.1 Adaptive median filter

The adaptive median filter [11] had been proposed as an improved version of traditional median filtering, which mainly contains two parts: noise detection and median filtering with adjustable window size. The noise detection determines whether a pixel is corrupted by impulsive noise or not. The median filter is then only applied to the noise pixel, which can reduce the computational cost. To determine the noise pixels, we defined a simple criterion as follows:

$$\left| I(x,y) - \bar{I}_{x,y} \right| > T_1 \tag{1}$$

where I(x,y) is an image pixel at (x, y), $\bar{I}_{x,y}$ is the mean value of the pixels within a n × n window centered at (x, y), and T_1 is the predefined threshold. With this simple noise detection, the further processing is only applied to the detected noise pixels, thus the computational cost can be reduced.

The traditional median filter is suitable for the impulsive noise (e.g., salt-and-pepper noise). However, it is possible that the median value of the pixels within a fixed window is still one of the noise pixels if the window size is small. On the other hand, one may lose the detail information or structure of an image if the window size is large. To avoid these problems, the window size should be adjustable according to the noise level and content of image. Figure 2 shows the flow chart of the adaptive median filter, where W_{xy} is the window centered at (x, y), T_2 is the predefined threshold, and I_{min}, I_{med}, I_{max} are minimum, median, maximum values within the window W_{xy}.

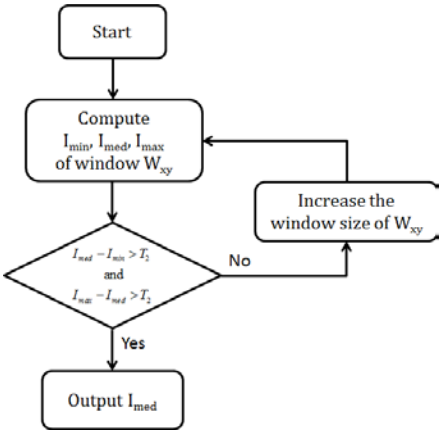

Figure2. The flow chart of the median filter with adjustable window size.

2.2 Bilateral filter

The adaptive median filter is able to handle the dense impulsive noise, however, it still shows limited success to handle the Gaussian noise. To reduce the Gaussian noise effectively, we applied the bilateral filter [7] as the complement part of adaptive median filter.

Bilateral filter is a non-linear filter which takes both the spatial distance and pixel similarity into considerations. The bilateral filtered result of a pixel I_c is computed as follows:

$$I'_c = \frac{\sum_{q \in W} f\left(|c-q|\right) g\left(\left|I_c - I_q\right|\right) I_q}{\sum_{q \in W} f\left(|c-q|\right) g\left(\left|I_c - I_q\right|\right)} \tag{2}$$

where W is the window centered at position c, f (.) is the spatial weighting function, and g(.) is the similarity weighting function. Typically, both the spatial and similarity weighting functions are Gaussian kernels, which are defined as follows:

$$f\left(\left|c-q\right|\right)=Ae^{-\frac{\left|c-q\right|^2}{2\sigma_f^2}} \tag{3}$$

$$g\left(\left|I_c-I_q\right|\right)=Be^{-\frac{\left|I_c-I_q\right|^2}{2\sigma_g^2}} \tag{4}$$

Where A and B are normalization constants, σ_f^2 and σ_g^2 are the variances of the Gaussian kernels.

Unlike the traditional spatial filter (e.g., Gaussian filter, mean filter) which may blur the edges of image, bilateral filter is able to effectively reduce the Gaussian noise while preserving the edges of image since it takes pixel similarity into consideration. The pixels which are dissimilar to the center pixel will have small weightings in Eq. (2), thus the edges will not be blurred.

2.3 Mathematical morphology

Mathematical morphology [25] is a branch of nonlinear filters, which is usually used to address the image sharpening problem [26]. We applied top-hat and bottom-hat transform in our morphological processing, which can extract the features of a gray scale image. The top-hat transform and the bottom-hat transform of an image can be defined as follows:

$$I_{top}=I-\left(I\circ b\right) \tag{5}$$

$$I_{bottom}=\left(I\bullet b\right)-I \tag{6}$$

where ◦ is the gray scale "opening" operator, • is the gray scale "closing" operator, and b is the structure element. The opening operation is used to emphasize the features with darker gray scales, while the closing operation is used to emphasize the features with brighter gray scales. Therefore, by taking the difference between the original image and its opening and closing versions in Eq. (5) and Eq. (6), it is clear that the top-hat transform can extract the brighter features and the bottom-hat transform can extract the brighter features.

After we obtained the top-hat and bottom-hat of the image, we combined the image and its top-hat and bottom-hat transformed versions to create an enhanced image:

$$I_{new}=I+I_{top}-I_{bottom} \tag{7}$$

The top-hat transform extracts the peaks and ridges which were removed by the opening operation, thus adding these features to the original image is able to enhance brighter structures; on the other hand, the bottom-hat transform extracts the valleys and troughs which were removed by closing operation, thus subtracting these features is able to enhance the darker structures (i.e., made the darker features even darker).

2.4 Contrast limited adaptive histogram equalization

Pizar et al. [15] proposed the "Contrast limited adaptive histogram equalization" (CLAHE) as the improved version of adaptive histogram equalization (AHE). The AHE computes the histogram of a local window centered to determine the mapping function for the local region, which results in local contrast enhancement. However, AHE may amplify the noise in homogeneous region due to the large slope of mapping function. On the contrary, the CLAHE restricts the slope of mapping function which is able to reduce the undesired amplification of noise in homogeneous region. Since there are many homogeneous regions in medical images, thus the CLAHE is suitable for enhancing medical images.

First, the image is divided into several non-overlapping regions with equal size, and the histograms of each region are then calculated. To restrict the slope of mapping function, the clip-limit β is defined as follows:

$$\beta = \frac{M}{256}\left(1+\frac{\alpha}{100}\left(s_{max}-1\right)\right) \tag{8}$$

where M is the number of pixels in a region, α is the clip factor within the range of [0, 100], and s_{max} is the maximum slope which is typically in the range of [1, 4]. The histogram bins with the pixel counts exceeding the clip-limit are redistributed to all bins equally, as shown in Figure 3. This process will repeat until there is no histogram bin with pixel count exceeding the clip-limit. Next, the redistributed histograms of each region are used to compute their own mapping functions for the traditional histogram equalization. Finally, each pixel of image is obtained by using bilinear interpolation based on its remapped values from mapping functions of neighbor regions. For more details of CLAHE, please refer to [15].

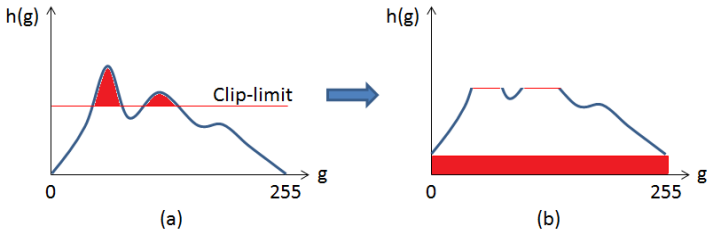

Figure 3. The illustration of histogram redistribution in CLAHE. (a) The original histogram. (b) The redistributed histogram.

3 Results and Discussions

3.1 Experimental setup

In the experiments, we test five X-ray images with low contrast, as shown in Figure 4, to evaluate the performance of different methods. We evaluated the performance of noise removal and contrast enhancement independently since the noise removal and contrast enhancement are two separate issues. To evaluate the performance of noise removal, we tested three cases: (1) adding the Gaussian noise with standard deviation 10 to the images; (2) adding the salt-and-pepper noise with probability 10% to the images; (3) adding both the noises to the images. We compared our method with adaptive median filter, bilateral filter, and the method proposed by Kurt et al. [3], in the experiments of noise

removal. Then we compared our method with AHE and CLAHE in the experiments of contrast enhancement. The parameters in our method are: T_1 = 8, T_2 = 3, σ_f = 2, σ_g = 12, s_{max} = 4, and α = 1, respectively. We fixed all the parameters for all the images in the experiments.

Figure 4. The test images used in the experiments.

3.2 Evaluation of noise removal

To evaluate the results objectively, we use two quantitative indexes, which are peak signal-to-noise ratio (PSNR) and structural similarity (SSIM), in the noise removal experiments. These two indexes are computed as follows:

$$PSNR(X,Y)=10\cdot\log_{10}\left(\frac{255^2}{MSE(X,Y)}\right) \tag{9}$$

$$SSIM(X,Y)=\frac{1}{N}\sum_{i=1}^{N}\frac{(2\mu_{x,i}\mu_{y,i}+c_1)(2\sigma_{xy,i}^2+c_2)}{(\mu_{x,i}^2+\mu_{y,i}^2+c_1)(\sigma_{x,i}^2+\sigma_{y,i}^2+c_2)} \tag{10}$$

where X is the denoised image and Y is the original image; MSE(·) is the mean square difference between two images; N is the number of pixels; i is the pixel index; $\mu_{x,i}$ and $\mu_{y,i}$ are the mean values of a local window centered at pixel i; $\sigma_{x,i}$ and $\sigma_{y,i}$ are standard deviations, and $\sigma_{xy,i}^2$ is the covariance; c_1 and c_2 are constants.

We first tested the images with Gaussian noise. Table 1 and Table 2 show the PSNR and SSIM of the images denoised by different methods. Bilateral filter is able to deal with the Gaussian noise, therefore, the PSNR and SSIM is higher than the other two. Our method combines the adaptive median filter and bilateral filter such that the results of our method are close to the results of bilateral filter.

Table 1. PSNR (dB) of the denoised images with Gaussian noise

Images	Adaptive median filter	Bilateral filter	[3]	Our method
1	35.04	41.72	36.81	41.40
2	35.22	42.10	40.16	42.11
3	35.10	41.95	40.36	41.96
4	35.70	38.87	36.19	38.66
5	35.29	39.61	35.63	41.73
Average	35.27	40.85	37.83	41.17

We then tested the images with impulsive noise, i.e., salt-and-pepper noise. Table 3 and Table 4 show the PSNR and SSIM of the images denoised by different methods. In this case, the adaptive median filter outperforms the other two. Since our method contains the adaptive median filter, therefore, in this case, the performance of our method is very close to the adaptive median filter.

Table 2. SSIM of the denoised images with Gaussian noise

Images	Adaptive median filter	Bilateral filter	[3]	Our method
1	0.8017	0.9683	0.9341	0.9686
2	0.7754	0.9315	0.9026	0.9339
3	0.8028	0.9602	0.9469	0.9617
4	0.8410	0.9165	0.8779	0.9145
5	0.8437	0.9661	0.9492	0.9662
Average	0.8129	0.9485	0.9221	0.9490

Table 3. PSNR (dB) of the denoised images with salt-and-pepper noise

Images	Adaptive median filter	Bilateral filter	[3]	Our method
1	52.32	24.57	26.44	51.42
2	55.36	25.40	31.96	52.80
3	55.70	25.12	29.43	53.40
4	46.11	24.77	29.15	45.71
5	43.15	25.34	31.21	43.01
Average	50.53	25.04	29.64	49.27

Table 4. SSIM of the denoised images with salt-and-pepper noise

Images	Adaptive median filter	Bilateral filter	[3]	Our method
1	0.9982	0.7240	0.8336	0.9973
2	0.9975	0.6881	0.9377	0.9955
3	0.9981	0.7129	0.9074	0.9966
4	0.9889	0.9165	0.8697	0.9870
5	0.9973	0.6959	0.9346	0.9961
Average	0.9960	0.7475	0.8966	0.9945

Finally, we tested the images with mixed noises. Table 5 and Table 6 show the PSNR and SSIM of the results of different methods. In this case, our method significantly outperforms the other three methods since we combine the adaptive median filters and bilateral filter such that even the mixed noise can be removed effectively without distorting the image structure. Our method obtained averaged PSNR 40.49 dB and averaged SSIM 0.9469, which outperforms the PSNR of adaptive median filter (35.92 dB) and the SSIM of [3] (0.8655). For visual evaluation, Figure 5 shows an example of the denoised results in the mixed-noise case. We can observe that our method obtain the result with least noise which is most similar to the original image.

Table 5. PSNR (dB) of the denoised images with mixed noise

Images	Adaptive median filter	Bilateral filter	[3]	Our method
1	36.06	24.70	26.87	41.22
2	36.28	25.41	31.32	42.05
3	36.19	24.92	30.04	41.83
4	35.68	25.10	30.04	37.80
5	35.41	25.53	31.66	39.55
Average	35.92	25.13	29.99	40.49

Table 6. SSIM of the denoised images with mixed noise

Images	Adaptive median filter	Bilateral filter	[3]	Our method
1	0.8395	0.7126	0.8216	0.9684
2	0.8144	0.6418	0.8692	0.9368
3	0.8408	0.6771	0.8882	0.9617
4	0.8417	0.6762	0.8329	0.9019
5	0.8481	0.6911	0.9158	0.9657
Average	0.8369	0.6798	0.8655	0.9469

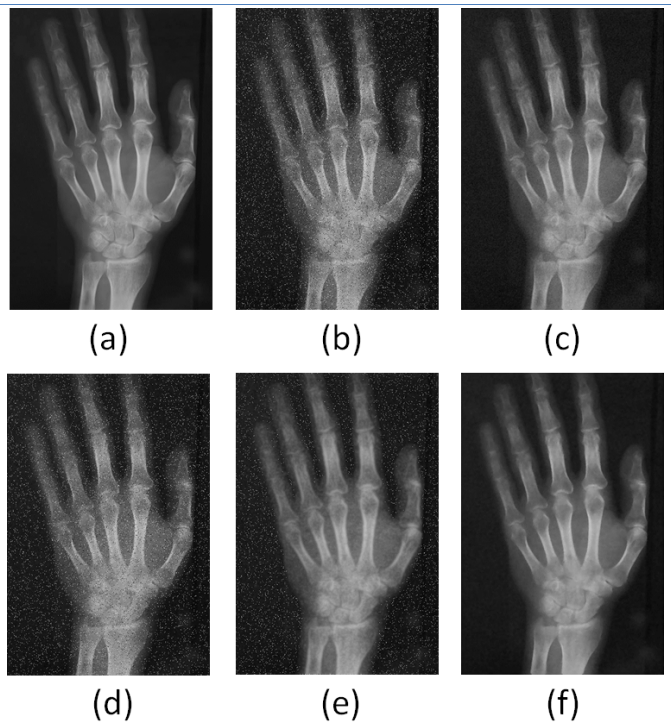

Figure 5. The denoised results. (a) The original image. (b) The image with mixed noise. (c) Image denoised by adaptive median filter. (d) Image denoised by bilateral filter. (e) Image denoised by [3] (f) Image denoised by our method.

3.3 Evaluation of contrast enhancement

A typical way to compare the contrast enhancement is visual evaluation. Figure 6 shows the enhanced images of different methods. We can observe that the AHE results in over-contrast images, which is not the desired results; on the contrary, CLAHE and our method are able to obtain visually satisfactory results. By applying the mathematical morphology before contrast enhancement, our method can obtain more details such as edges and textures than the CLAHE.

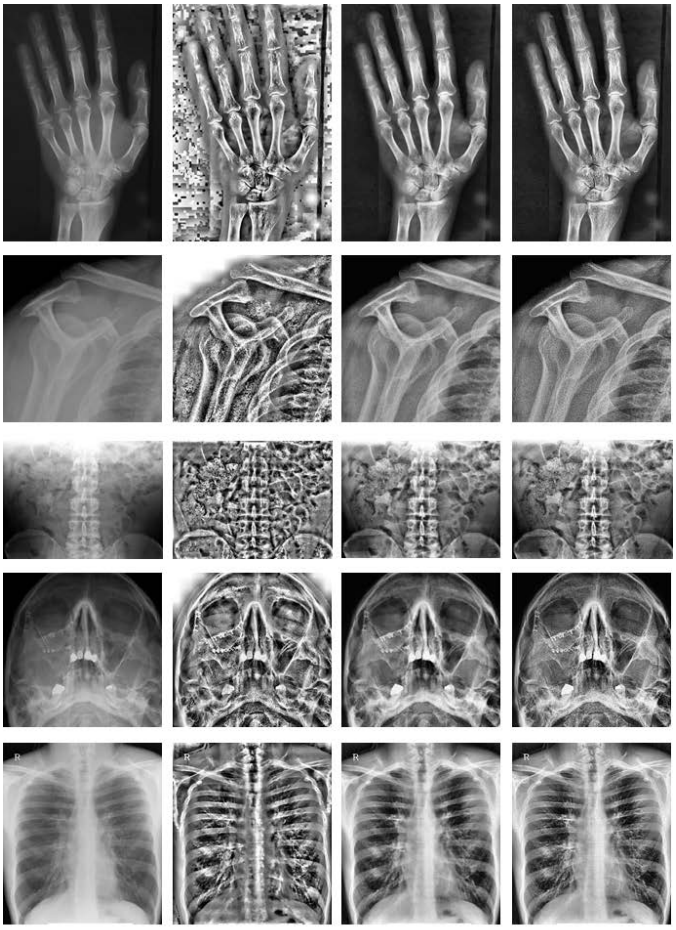

Figure 6. The images enhanced by different methods. (a) The original images. (b) The results of AHE. (c) The results of CLAHE. (d) The results of our method.

To evaluate the contrast enhancement objectively, we applied the "absolute mean brightness error" (AMBE) [22] as the quantitative index to compare the results of different methods. The AMBE is defined as follows:

$$AMBE = \frac{1}{N}\sum_{i=1}^{N}\left|\bar{I}_i - \bar{O}_i\right| \tag{11}$$

where N is the number of pixels in the image; $\bar{I}_i$ and $\bar{O}_i$ are the mean values of a local window with size 5 × 5 centered at i-th pixel in the enhanced image and original image, respectively. The AMBE computes the averaged difference of mean brightness between the original image and the enhanced one. Ideally, the contrast enhancement should preserve the same mean brightness of an image. Therefore, the lower AMBE represents less brightness bias. Table 7 shows that the AHE has much higher AMBE than the CLAHE and our method since the over-contrast problem in the homogeneous regions. Our method obtained only slightly higher AMBE than CLAHE, therefore, we need another index, EME, to compare the performance of contrast enhancement.

Table 7. AMBE of the different methods for contrast enhancement

Images	AHE	CLAHE	Our method
1	82.4412	22.3001	24.0573
2	59.5952	18.5297	19.2049
3	61.6608	27.9984	29.7133
4	62.9189	30.3828	32.5923
5	45.3140	19.0869	19.8624
Average	62.3860	23.6596	25.0860

Table 8. EME comparisons

Images	Original image	CLAHE	Our method
1	15.5255	28.5173	34.3282
2	12.2870	19.0951	24.1989
3	10.8004	23.4589	29.2741
4	22.5410	35.9354	46.9401
5	14.8050	26.7551	33.2626
Average	15.5255	28.5173	34.3282

The EME is defined as follows:

$$EME = \frac{1}{K}\sum_{i=1}^{K}\left(20\cdot\ln\left(\frac{I_{i,max}}{I_{i,min}}\right)\right) \tag{12}$$

where the image is divided into K non-overlapping blocks with equal size m × m (we set m = 32 in this paper), $I_{i,max}$ is the maximum value of the i-th block, and $I_{i,min}$ is the minimum value of the i-th block. The EME averages the contrast of all the local regions to represent the contrast of whole image, which means the higher EME, the better contrast of image. Table 8 shows that our method obtained the images with significantly higher EME than the original images and the images enhanced by CLAHE.

4 Conclusions

In this paper, we have proposed an algorithm with capability of noise reduction and contrast enhancement for X-ray images. The noise reduction part combines the adaptive median filters and bilateral filter to deal with the mixed noise. Then we apply the mathematical morphology followed by CLAHE to enhance the contrast with more details such as edges. The experiments show that our method is able to obtain averaged PSNR 40.49 dB and averaged SSIM 0.9469 in the mixed noise case; for the contrast enhancement, our method is able to obtain higher EME values than CLAHE, which means the images enhanced by our method have better contrast than the images enhanced by CLAHE.

REFERENCES

[1]. Langland, O.E., et al., *Principles of Dental Imaging*. Lippincott Williams & Wilkins, 2002.

[2]. Ito, K. and Xiong, K., *Gaussian filters for nonlinear filtering problems*. Automatic Control, IEEE Transactions on, 2000. 45(5): p. 910-927.

[3]. Kurt, B., et al., *Medical images enhancement by using anisotropic filter and clahe*. In Innovations in Intelligent Systems and Applications (INISTA), 2012 International Symposium On, 2012. p. 1-4.

[4]. Perona, P. and Malik, J., *Scale-space and edge detection using anisotropic diffusion*. Pattern Analysis and Machine Intelligence, IEEE Transactions on, 1990. 12(7): p. 629-639.

[5]. Yu, Y. and Acton, S.T., *Speckle reducing anisotropic diffusion*. Image Processing, IEEE Transactions on , 2002. 11(11): p. 1260-1270.

[6]. Paris, S., et al., *A gentle introduction to bilateral filtering and its applications*. In ACM SIGGRAPH 2007 Courses, 2007.

[7]. Tomasi, C. and Manduchi, R., *Bilateral filtering for gray and color images*. In Computer Vision, Sixth International Conference On, 1998. p. 839-846.

[8]. Lin, H.-M. and Willson Jr, A.N., *Median filters with adaptive length*. Circuits and Systems, IEEE Transactions on, 1988. 35(6): p. 675-690.

[9]. Ko, S.-J. and Lee, Y.H., *Center weighted median filters and their applications to image enhancement*. Circuits and Systems, IEEE Transactions on, 1991. 38(9): p. 984-993.

[10]. Tsai, C.-Y., *An adaptive rank-ordered median image filter for removing salt-and-pepper noise*. Master's thesis, National Cheng-Kung University, 2006.

[11]. Hwang, H., et al., *Adaptive median filters: new algorithms and results*. Image Processing, IEEE Transactions on, 1995. 4(4): p. 499-502.

[12]. Lehr, J. and Capek, P., *Histogram equalization of ct images*. Radiology, 1985. 154(1): p. 163-169.

[13]. Khalid, N.E.A., et al., *Cr images of metacarpel cortical edge detection-bone profile histogram approximation method*. In Intelligent and Advanced Systems (ICIAS), International Conference On, 2007. p. 702-708.

[14]. Wang, Y., et al., *Image enhancement based on equal area dualistic sub-image histogram equalization method*. Consumer Electronics, IEEE Transactions on, 1999. 45(1): p. 68-75.

[15]. Pizer, S.M., et al., *Adaptive histogram equalization and its variations*. Computer vision, graphics, and image processing, 1987. 39(3): p. 355-368.

[16]. Stark, J.A., *Adaptive image contrast enhancement using generalizations of histogram equalization*. Image Processing, IEEE Transactions on, 2000. 9(5): p. 889-896.

[17]. Sund, T. and Møystad, A., *Sliding window adaptive histogram equalization of intraoral radiographs: effect on image quality*. Dentomaxillofacial Radiology, 2014.

[18]. Kim, Y.-T., *Contrast enhancement using brightness preserving bi-histogram equalization*. Consumer Electronics, IEEE Transactions on, 1997. 43(1): p. 1-8.

[19]. Shoaib, M., et al., *Design and implementation of efficient information retrieval algorithm for chest x-ray images*. Journal of American Science, 5(4): p. 43-48.

[20]. Sund, T. and Eilertsen, K., *An algorithm for fast adaptive image binarization with applications in radiotherapy imaging*. Medical Imaging, IEEE Transactions on, 2003. 22(1): p. 22-28.

[21]. Noor, N.M., et al., *Fish bone impaction using adaptive histogram equalization (ahe)*. In Computer Research and Development, 2010 Second International Conference On, 2010. p. 163-167.

[22]. Ibrahim, H. and Kong, N.S.P., *Brightness preserving dynamic histogram equalization for image contrast enhancement*. Consumer Electronics, IEEE Transactions on, 2007. 53(4): p. 1752-1758.

[23]. Yang, Y., et al., *Medical image enhancement algorithm based on wavelet transform*. Electronics letters , 2010. 46(2): p. 120-121.

[24]. Shrimali, V., et al., *Comparing the performance of ultrasonic liver image enhancement techniques: a preference study*. IETE Journal of Research, 2010. 56(1): p. 4-10.

[25]. Gonzalez, R.C. and Woods, R.E., *Digital Image Processing (3rd Edition)*. Prentice-Hall, Inc., Upper Saddle River, NJ, USA, 2006.

[26]. Mahmoud, T.A. and Marshall, S., *Medical image enhancement using threshold decomposition driven adaptive morphological filter*. In 16th European Signal Processing Conference (EUSIPCO), 2008.

[27]. Agaian, S.S., et al., *Transform-based image enhancement algorithms with performance measure*. Image Processing, IEEE Transactions on, 2001. 10(3): p. 367-382.

SOCIETY FOR SCIENCE AND EDUCATION UNITED KINGDOM

JBEMi JOURNAL OF BIOMEDICAL ENGINEERING AND MEDICAL IMAGING

ISSN: 2055-1266
VOLUME 3 ISSUE 1

Enhancement of CT Images by Modified Object Based Contrast Stretching

Deepti Mittal, Kanika Sharma, Ritambhara Thakur, Abhay Krishan, Rishabh Singhal, and Anju Rani
Electrical and Instrumentation Engineering Department, Thapar University, Patiala (Punjab), India;
deepti.mittal@thapar.edu; kanika.3991@gmail.com; ritambhara3939@gmail.com;
abhaykrishan44@gmail.com; singhalrishabh21@gmail.com; anju.yaduvanshi@yahoo.com

ABSTRACT

The characteristic information of an organ lies in the texture of the image obtained by computed tomography imaging procedure. Therefore, enhancement of CT image aids a radiologist to better diagnose a disease which is a result of the enhanced/improved perceptibility and interpretability of the information present in the texture of the image. The present work proposes a method for texture enhancement of CT images by modifying Object-Based Multilevel Contrast Stretching method proposed by B. Xu et al. (IEEE Transaction on Consumer Electronics 3:1746-1754, 2010). In proposed method, a CT image is split into two images; (i) object approximation image and (ii) object error image. Object approximation image contains the overall structural information and object error image contains all the textural details of the CT image. The proposed method enhances the local contrast of object error image at an intra-object level, by greedy iterative stretch algorithm. Experimental results show that the proposed method enhances the textural details effectively, while maintaining the mean brightness of the image. Moreover, the quantitative results have verified that the proposed method outperforms the other methods.

Keywords: Intra-object;Texture, CT images; Enhancement; MOBCS.

1 Introduction

The computed tomography (CT) scan is one of the most common and important medical imaging modality. It is used, mostly, to evaluate the presence, size and location of the tumors present in a specific organ of the body. This evaluation is helpful in further diagnosis and confirmation of the disease. When a medical practitioner is involved in the diagnosis of a complicated case, such as detection and identification of liver cancer, texture contrast of a CT image plays an important role. Computed tomography images have good global contrast which can be further enhanced by adjusting window settings. Still, there is a limitation in the visualization of textural details in CT images. Improved visualization of texture may help to doctor in easy differentiation between various tumors, for example differentiation between liver cancer like Hepatocellular Carcinoma (HCC) and Metastasis [1-3]. This improvement in localized contrast of an image can make even small tumors or infections perceptible. A tumor is an abnormal growth of tissues, and there is a difference in the characteristic information of

DOI: 10.14738/jbemi.31.1828
Publication Date: 29th February 2016
URL: http://dx.doi.org/10.14738/jbemi. 31.1828

normal tissues and abnormal tissues. This characteristic information regarding tissues exists in the texture of CT images. Therefore, there is a need for an enhancement method for better texture visualization. This improvement in texture visualization will aid the doctor with improved perceptibility and interpretability of information enclosed by the image. Further, the enhancement of texture helps to doctor, in easy confirmation and better diagnosis of disease. Overall, the quality of CT images is of high significance to the doctor for better diagnosis with less fatigue. Further, the image quality depends on various parameters such as noise, spatial resolution, artifacts, contrast etc. In the present work, the quality of CT images is improved by enhancing contrast of the texture.

Among the various enhancement methods in literature on medical and non-medical images, global histogram equalization (GHE) is the most commonly used method for contrast enhancement [4]. The method enhances the contrast and dynamic range of an image by (i) stretching the grey levels of an image histogram over full intensity range and (ii) creating a uniform distribution of intensity levels. The limitation of GHE is that it occasionally introduces over enhancement and saturation artifacts. Local histogram equalization (LHE) is an extension of GHE, which helps in enhancement of the local details of an image [4, 5]. LHE method is implemented by moving a window of suitable size on the image and then transformation function of GHE is applied only to the part of image which is covered by the window. However LHE also enhances the noise alongwith details of the image. Zhu *et. al.* proposed a constrained local histogram equalization method to remove the drawback of LHE and preserve the overall appearance of the image [5]. In this method variational formulation of histogram equalization (HE) is extended directly to LHE and a constraint is added to preserve the original appearance of the image. Another approach for enhancement based on Histogram is Multi-peak generalized histogram equalization method [6]. The method enhances the texture alongwith the contrast of images. The enhancement is performed by piecewise partitioning and equalizing the image histogram according to the proposed generalized transformation function of histogram equalization. Constrained local histogram equalization and MPGHE methods have not been applied to medical images. Tsai *et. al.* proposed an adaptive enhancement algorithm which enhances the CT medical images by removing noise without considerably blurring the structures in the image [7]. Noise is removed by adaptive smoothing filter. The drawback of this method is that it loses the local textural details of the image due to the effect of smoothing filter. Jafar and Ying proposed a method based on the extension of GHE i.e., Constrained variational histogram equalization [8]. The method overcomes the shortcoming of GHE by preserving the mean brightness of the image while enhancing the contrast of the image. It is based on the variational approach of HE and a constraint added to transformation function of variational GHE preserves the mean brightness of the image. This method improves the drawback of GHE but it does not enhance the local details of the image. Another approach for contrast enhancement simultaneously preserving the overall appearance of the image is histogram modified local contrast enhancement [9]. This method involves the modification of histogram to control the enhancement levels and local contrast enhancement technique for local details enhancement of the image. This method has been tested on mammogram images and delivered effective results. Tan *et. al.* proposed extreme level eliminating adaptive histogram equalization method [10]. The method is used to enhance CT images of the brain for ischemic stroke detection. In this method, the image is first split into non overlapped sub-blocks, and then each sub block is equalized by extreme level eliminating equalization transformation function. This is an efficient method but it focuses mainly on enhancing the hypo-dense area in CT

images. An intensity adaptive nonlinear multi-scale contrast enhancement method is proposed to enhance the contrast and details of digital radiography [11]. This method has steps of enhancement including noise reduction, range compression, detail enhancement, contrast enhancement, tone scale-up manipulation. Another method, based on histogram manipulation, is proposed by Sharma and Mittal i.e., histogram equalization with constrained variational offset (HECVO) [12]. This method enhances the texture of the CT images and is based on the modification of histogram equalization. The modification is done by adding a constrained variational offset to the transformation function of HE, this offset helps in preserving the mean brightness and global appearance of the image. This method enhances the contrast of CT image effectively but is limited to global enhancement. Wang *et. al.* proposed a medical image enhancement method based on non sub-sampled contourlet transform and improved fuzzy contrast [13]. In this method, linear enhancement method is used to deal with low frequency coefficients and threshold function is used to handle the high frequency coefficients. Finally, improved fuzzy contrast is used for global enhancement and Laplace operator is used for local or detail enhancement. This method is suitable for detail enhancement of medical images but the enhanced results specifically for CT images shows some distortion from the original image. Another approach for contrast enhancement of CT images is tuned brightness controlled single-scale retinex proposed by Al-Ameen and Sulong [14]. This method is extension of the single-scale retinex (SSR), which includes tuning of SSR and inserting a normalized-ameliorated sigmoid function. This method enhances the contrast but it does not emphasize on the improvement of the textural detail. Object based multilevel contrast stretching (OBMCS) method is another approach for contrast enhancement [15]. It enhances the contrast of the image at two levels: inter-object and intra-object with different enhancement algorithms. Inter-object level enhances the structures of the image by greedy iterative stretch algorithm and intra-object level enhances the textural details of the image by linear contrast stretching. OBMCS method has been tested on consumer electronics images but it has not been applied to the CT images.

In present work the modified object based contrast stretching (MOBCS) enhancement method is proposed and applied on CT images. CT images have good structural and global details. Further processing on CT image at inter-object level creates over enhancement and it may lead to false interruption of structural details. Therefore, MOBCS is designed with intra-object enhancement principally to improve the visibility of textural details in CT images. Therefore, the method is implemented by (i) modification in OBMCS method with single level enhancement only at object error image for texture contrast enhancement of CT images and (ii) addition of a parameter to preserve the mean brightness of original image. The proposed research work is organized as follows: section-II includes background of the method with some basic definitions and methods used in the proposed method, brief description of OBMCS method, proposed method and performance measures. Section-III includes results and discussion and section- IV describes the final conclusion of the paper.

2 Methods

2.1 Background

In this section, the basic methods used in formation of the proposed method i.e., segmentation method and contrast stretching method, are discussed. Morphological watershed segmentation method is used for segmentation of the image to obtain the objects with homogenous intensities [4, 16, 17]. According

to the basic idea of watershed segmentation an image can be seen as a relief-map with intensity values denoting elevation of the map. Assume a hole is punched in the regional minimum and therefore relief-map is flooded with water from bottom of the catchment basin at uniform rate. When the two catchment basins are about to merge a short dam is constructed to prevent merging of water. These dams are interpreted as watershed lines and these lines are the desired segmentation result of the image. The watershed method is applied to the gradient image not on the original image directly.

Watershed segmentation method is very sensitive, even to small variation of intensities. Therefore, it sometimes generates over-segmentation. Over segmentation can be avoided by (i) pre-processing of the gradient image and (ii) and post-processing of the segmented image. The pre-processing is accomplished by gradient thresholding and the post-processing is implemented by region merging [4]. The implementation of gradient thresholding is shown in next sub-section. Region merging is applied to merge the segments created by watershed method and implemented by merging of the adjacent segments step by step with a merging criterion [16, 17]. In addition, the merging of adjacent segments can be arrested by adding a specific stopping condition. Further, the performance of the merging of segments is highly influenced by the merging criterion which is being used for region merging. In literature, a number of merging criteria have been proposed which are broadly dependent on (i) the features of segmented region and (ii) the dissimilarity function. Ward criterion, just noticeable difference criterion, mean criterion, ward-mean criterion, border criterion, linear luminance criterion etc are the examples of merging criteria based on the features of a segmented region [18]. Stopping condition δ_t for region merging can depend on the estimated standard deviation of noise σ of original image [19]. Finally, Region merging algorithm is implemented efficiently by region adjacency graph (RAG) [16].

Contrast stretching in the proposed method is done by greedy iterative stretching [20]. This method enhances the local contrast of the image. Here, the image is visualized as a grid of size M×N and intensity of the pixel as height of the grid. For each iteration a threshold plane is decided and non-zero connected components are calculated for the image grid pixels which are above the threshold plane. The set of connected components is known as hillock. All hillocks are scaled according to certain constraints. The threshold planes are swept iteratively between the lower and upper limits decided for image and accordingly hillocks are scaled. The image is inverted and the sweep and scaling process is applied to inverted image. The image is again inverted for getting the contrast enhanced image.

2.2 Object based multilevel contrast stretching method

Object based multi level contrast stretching method is proposed by Xu et al. The method first obtains the gradient magnitude image, $G(i, j)$ from the original image, $I(i, j)$ using sobel operator. The mathematical formula is as follows:

$$G(i, j) = \left|G_i(i, j)\right| + \left|G_j(i, j)\right| \tag{1}$$

where $G_i(i, j)$ and $G_j(i, j)$ are the gradient components in horizontal and vertical direction respectively.

On the acquired gradient magnitude image, the gradient threshold is applied to prevent over segmentation before watershed segmentation. Gradient thresholding is implemented as follows:

$$G_n(i,j) = \begin{cases} G_t & if\ G(i,j) < G_t \\ G(i,j) & otherwise \end{cases} \quad (2)$$

where G_n is new gradient image after thresholding, G_t is gradient threshold which helps in prevention of over segmentation. After thresholding, gradient magnitude image is served as an input to the watershed segmentation method. After applying watershed method, region merging is applied as post processing for prevention of over segmentation. Xu et al., applied mean criterion for region merging on segmented result obtained by watershed method. The dissimilarity function for mean criterion of region merging is:

$$\delta(S_i, S_j) = \left|\mu(S_i) - \mu(S_j)\right| \quad (3)$$

where $\mu(S)$ denotes the mean of the region S. The mean criterion merges pairs of adjacent region comprising value of dissimilarity function less than the assigned stopping condition δ_t. The image is further divided into two sub images, (i) object approximation image (OAI) and (ii) object error image (OEI). Object approximation image, denoted by $I_a(i,j)$ is obtained by replacing each pixel in the original image by mean intensity value of the corresponding region. Object error image, denoted by $I_e(i,j)$, is calculated by subtracting the OAI from original image. The mathematical representation of OAI and OEI is as follows:

$$I_a(i,j) = \mu(S_{(i,j)}) \quad (4)$$

$$I_e(i,j) = I(i,j) - I_a(i,j) \quad (5)$$

The original image $I(i,j)$ can be obviously obtained using eq. (4) and (5):

$$I(i,j) = I_a(i,j) + I_e(i,j) \quad (6)$$

In OBMCS method, the inter-object contrast enhancement of OAI is accomplished by greedy iterative stretching proposed by Majumder and Irani (2007) and intra-object contrast enhancement of OEI is done by linear contrast stretching. Finally, both enhanced images are combined to get the final enhanced result.

2.3 Proposed method

The proposed method comprises of single level of contrast stretching i.e. intra-object contrast enhancement because it leads to textural features enhancement, which is required for CT images. Since, CT images have good structural and global details; the inter-object contrast stretching is not performed for CT images as it may lead to false interpretation of structural detail. Flow chart of proposed method is shown in Figure 1 and the steps involved are explained in detail as follows:

STEP 1: Segmentation using watershed method

Watershed method produces stable close object contours in segmentation results. To avoid over segmentation produced by watershed pre and post processing is applied on the image. The pre-processing applied is gradient thresholding represented by eq. (1) and (2). The post- processing is similar to that of OBMCS method i.e., region merging, but there is a change in merging criterion used for region merging. Ward criterion is used in the proposed method because it is superior from mean criterion as it tends to minimize the total square error introduced by merging of two adjacent regions and it merges small regions not large ones. Ward criterion also eliminates noise and double edges [16, 21]. The dissimilarity function for ward criterion of region merging is:

$$\delta(S_i, S_j) = \frac{\|S_i\| \cdot \|S_j\|}{\|S_i\| + \|S_j\|} \left[\mu(S_i) - \mu(S_j)\right]^2 \tag{7}$$

where $\|S\|$ is the number of pixels in region S .

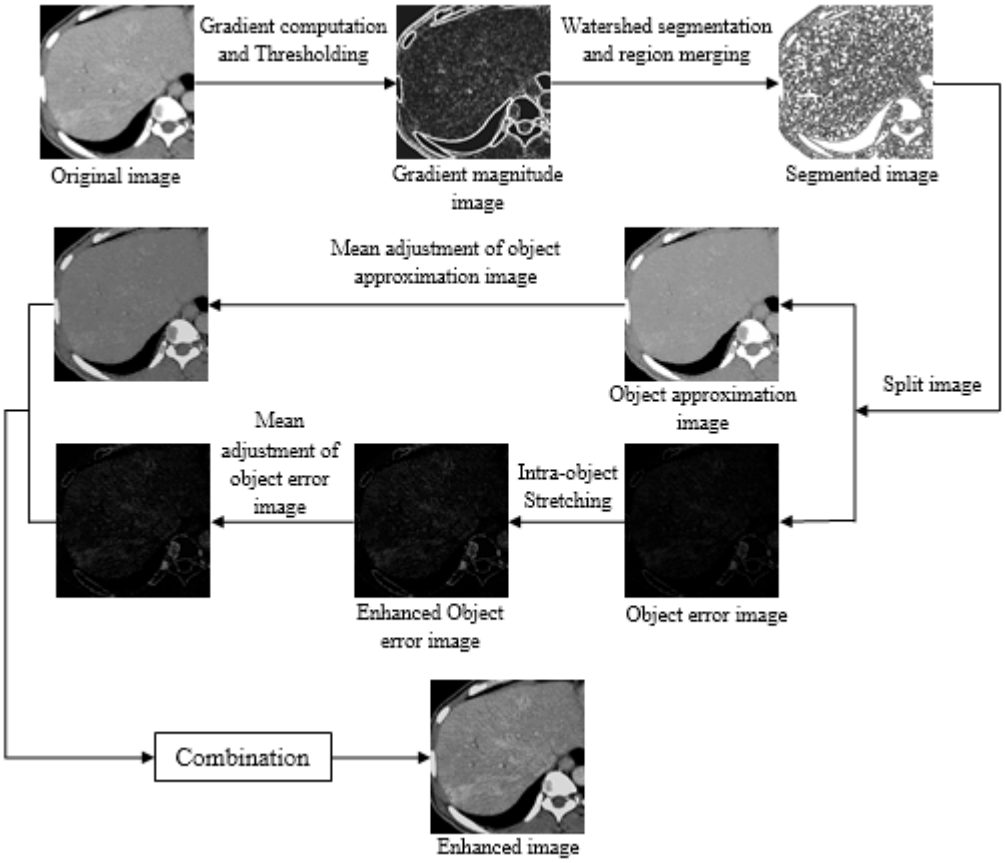

Figure 1. Flow chart of proposed method.

STEP 2: Intra-object contrast stretching

The object approximation image and object error image is constructed as shown in eq. (4) and (5). Intra-object contrast stretching is obtained by enhancing the contrast of the OEI. Object error image contains

the textural details and by enhancing it, textural details of CT images get enhanced. The OEI is enhanced using greedy iterative stretching unlike OBMCS where it is linearly stretched. The proposed method enhances the local contrast of texture part, so it uses greedy iterative stretching method for intra-object enhancement. The intra-object contrast stretching is carried out with the following constraints:

$$1 \le \frac{I'(i,j) - \mu'(S_{(i,j)})}{I(i,j) - \mu(S_{(i,j)})} \le (1+\lambda) \tag{8}$$

$$L \le I'(i,j) \le U \tag{9}$$

where $I(i,j)$ is original image, $I'(i,j)$ is enhanced image, $\mu(S_{(i,j)})$ is mean of region S of original image, $\mu'(S_{(i,j)})$ is mean of region S of enhanced image, λ is a parameter that controls the amount of enhancement, L and U are the lower (0) and upper (255) limit of gray scale intensity range, respectively. Constraints in eq. (8) and (9) are added to control the amount of contrast stretching and to eliminate the saturation effects in enhanced image. The greedy iterative stretching involves sweeping of threshold plane from L to U iteratively and stretching the hillocks (set of connected components in image matrix containing pixel values above threshold plane) greedily while taking the mentioned constraints into account. To further enhance the image, image is inverted and the same procedure of sweeping threshold plane is applied. After stretching the image is again inverted to obtain final enhanced OEI, $I'_e(i,j)$. Enhancement of OAI is not required in case of CT images.

STEP 3: Mean adjustment in OAI and OEI

The enhanced image obtained after combining the enhanced OEI with original OAI results in overall increment in brightness. To preserve the brightness of the image with enhanced textural details some mean adjustments are made. Before combining the two images, some percentage of mean of OAI is subtracted from the original OAI and similarly some percentage of mean of enhanced OEI is added to the enhanced OEI. This is implemented as follows:

$$newI'_e(i,j) = I'_e(i,j) + \alpha\%\ of\ \ \mu(I'_e(i,j)) \tag{10}$$

$$newI_a(i,j) = I_a(i,j) - \alpha\%\ of\ \ \mu(I_a(i,j)) \tag{11}$$

The value of α will decide the amount of global brightness of the image. Final enhanced image is obtained by combining the images calculated in eq. (10) and (11):

$$F(i,j) = newI'_e(i,j) + newI_a(i,j) \tag{12}$$

where $F(i,j)$ is final enhanced image.

2.4 Performance evaluation

The performance of enhanced CT images is evaluated by five performance parameters. The parameters are as follows:

2.4.1 Correlation Coefficient (ρ)

The correlation coefficient (ρ) measures the degree of linear correlation between the original and processed images [22]. ρ between original image $I(i,j)$ and enhanced image $F(i,j)$ of size $M \times N$ is expressed as given below:

$$\rho = \frac{\sum_{i=1}^{M}\sum_{j=1}^{N} F(i,j)I(i,j)}{\sqrt{\sum_{i=1}^{M}\sum_{j=1}^{N}(I(i,j))^2}\sqrt{\sum_{i=1}^{M}\sum_{j=1}^{N}(F(i,j))^2}} \tag{13}$$

2.4.2 Universal Image Quality Index (Q)

The universal image quality index measures the distortion between original and processed image [22, 23]. Mathematical representation is as follows:

$$Q = \frac{\sigma_{IF}}{\sigma_I \sigma_F} \cdot \frac{2\overline{F}\overline{I}}{(\overline{F})^2 + (\overline{I})^2} \cdot \frac{2\sigma_I \sigma_F}{\sigma^2{}_I + \sigma^2{}_F}, \quad -1 < Q < 1 \tag{14}$$

where $\overline{I}$ and $\overline{F}$ represent the mean of the original and processed images respectively. First component in the mathematical formula represents the linear correlation between the original and processed image, second component represent the local luminance and last component represents similarity of contrast between the two images. The higher values of Q show less distortion in the processed image.

2.4.3 Pratts's Figure of Merit (FOM)

The mathematical representation of FOM is as follows:

$$FOM = \frac{1}{\max(E, E_{ideal})} \sum_{i=1}^{E} \frac{1}{1 + d_i{}^2 \tau} \tag{15}$$

where E, E_{ideal}, d_i are the detected edges, ideal edges, Euclidean distance between i[th] detected pixel and its neighboring pixel respectively. τ is a constant mostly set to 1/9 [22, 24].

2.4.4 Feature Similarity Index ($FSIM$)

Feature similarity index measures the image local quality based on the low-level features of two images such as phase congruency and gradient magnitude [15]. Mathematical representation of $FSIM$ calculated between the original image $I(i,j)$ and enhanced image $F(i,j)$ is as follows:

$$FSIM = \frac{\sum_{i,j \in \Omega} Z_L(i,j) \cdot P_m(i,j)}{\sum_{i,j \in \Omega} P_m(i,j)} \tag{16}$$

where Ω is spatial domain image, $P_m(i,j)$ is maximum of phase congruency map of original and enhanced images and $Z_L(i,j)$ is given as:

$$Z_L(i,j) = [Z_P(i,j)]^x \cdot [Z_G(i,j)]^y \quad (17)$$

where Z_p is similarity measure for phase congruency of original and enhanced images, and Z_G is similarity measure for gradient magnitude of original and enhanced images. The higher values of FSIM show the better image quality.

2.4.5 Mean Structural Similarity Index ($MSSIM$)

Mean structural similarity index measures the similarity between structural information of original image and enhanced image [26]. The mathematical representation of $MSSIM$ is as follows:

$$MSSIM(I,F) = \frac{1}{R}\sum_{k=1}^{R} SSIM(I_k, F_k) \quad (18)$$

where I and F are original and enhanced images respectively, $SSIM(I_k, F_k)$ is structural similarity measure of original image and enhanced image at k[th] local window and R is the number of total local window.

3 Experimental Results and Discussion

The proposed MOBCS method is implemented in MATLAB version 7.10 on a PC with Intel core i5 (2.5 GHz) processor. In this research, 197 liver CT images, 20 out of which are images with HCC lesion, 82 with metastasis and 95 images of a normal liver were collected from Max Saket Hospital, New Delhi. These liver CT images were acquired from 4 different patients (male). The liver CT images were collected from the hospital in the form of DICOM format images and converted to portable network graphics (png) format and all images have their own clinical settings such as window width, window level, slice thickness etc. The proposed method is applied and tested on a data set of these liver CT images of size 514×514.

Subjective evaluation of performance of the method is examined by three different radiologists; one is an intern radiologist, a radiologist with the experience of less than five years and other with experience of more than 10 years. According to visual inspection of three radiologists, the proposed method is appropriate for enhancement of the texture of CT images and they suggest verifying the results with various objective evaluation procedures to validate the effectiveness of the method in general.

Objective evaluation is performed by correlation coefficient, Pratt's figure of merit, universal image quality index, feature similarity index and mean structural similarity index. These quantitative measures are also calculated for Contrast limited adaptive histogram equalization (CLAHE) and HEVCO method for comparison with proposed MOBCS method.

Table 1. Comparison of performance measures for enhancement methods.

Performance measures	CLAHE	HEVCO	MOBCS
ρ	$0.9871\pm6.5973\times10^{-06}$	$0.9872\pm3.1298\times10^{-05}$	$0.9929\pm5.5659\times10^{-06}$
Q	$0.9167\pm5.4600\times10^{-04}$	$0.9144\pm1.4550\times10^{-03}$	$0.9421\pm3.8845\times10^{-05}$
FOM	$0.5678\pm1.8169\times10^{-02}$	$0.5798\pm1.7507\times10^{-02}$	$0.6601\pm1.2709\times10^{-02}$
FSIM	$0.8467\pm2.6500\times10^{-04}$	$0.7942\pm2.1070\times10^{-03}$	$0.9378\pm2.9496\times10^{-05}$
MSSIM	$0.6989\pm6.7800\times10^{-04}$	$0.5091\pm2.1730\times10^{-02}$	$0.8378\pm9.0932\times10^{-04}$

Table-1 summarizes the results of these quantitative measures in the form of mean and variance to reduce sample bias. The first performance measure is correlation coefficient (ρ) that is used to find out the similarity between original and processed image. The dynamic range of correlation coefficient is [-1, +1], where +1 represents the images are positively correlated and -1 represents images are negatively correlated. The value of correlation coefficient for CLAHE method varies from 0.9815 to 0.9912 for data set of CT images and represented as the mean value i.e., 0.9871 in table 1. The value of ρ for HECVO method varies from 0.9702 to 0.9927 and the mean value is 0.9872, which is almost equal to that of CLAHE method. The value of ρ for proposed method varies from 0.9871 to 0.9951 and the mean value is 0.9929, which is highest among all of the three methods. This shows that MOBCS processed images comprise highest correlation with their corresponding original images. The second performance measures is universal image quality index (Q) and the range of Q is also [-1, +1], where value 1 shows that processed image is not at all distorted i.e., processed image is similar to the original image. Higher values of Q represent less distortion. Enhancement is an image processing strategy which sets changes in the intensity of the image, so that the processing that enhances the image may distort the information of the original image, but the changes occuring due to enhancement must not be so high that the processed image loses its original details. The minimum and maximum value of Q obtained by applying CLAHE method is 0.8854 and 0.9656 respectively also the mean value of Q is 0.9167. The value of Q for HECVO method varies from 0.8130 to 0.9692 and the mean value is 0.9144. The value of Q for proposed method varies from 0.9330 to 0.9575 and the mean value is 0.9421. The proposed method posses highest value of Q among all the three methods, which shows that Q is also improved for MOBCS method and there is less misrepresentation in enhanced images by proposed method than CLAHE and HEVCO method. The third performance measure is Pratt's figure of merit (FOM) which represents the edge preservation of the processed images. Its value lies in between 0 and 1, where 1 shows highest preservation of edges. The value of FOM for CLAHE method varies from minimum value 0.3883 to maximum value 0.8207 and the mean value of FOM is 0.5678. The value of FOM for HECVO method varies from minimum value 0.3627 to maximum value 0.8183 and the mean value is 0.5798. The value of FOM for proposed method varies from minimum value 0.4915 to maximum value 0.8672 and the mean value is 0.6601. The results confirm that the proposed method outperforms the other two methods. This shows that edge quality is also better for MOBCS method than other two methods. The fourth performance measure is feature similarity index (FSIM) and it is used to calculate the similarity of

local level features and local quality between original image and processed image and its value ranges between 0 and 1, value 1 shows the highest feature similarity between original and processed image. The value of FSIM for CLAHE method varies from 0.8258 to 0.8796 and the mean value is 0.8467. The value of FSIM for HECVO method varies from 0.6775 to 0.8520 and the mean value is 0.7942. The value of FSIM for MOBCS method varies from 0.9196 to 0.9452 and the mean value is 0.9378. The value of FSIM is highest for the proposed method, this shows that proposed method gives highest similarity between original and processed image. The last performance measure is mean structural similarity index (MSSIM) and its high values represent more structural similarity between original and processed image. The minimum value of MSSIM calculated for CLAHE method is 0.6722, the maximum value is 0.7635 and the mean value is 0.6989. The value of MSSIM calculated for HECVO method varies from minimum value 0.1189 to maximum value 0.6844 and the mean value is 0.5091. The value of MSSIM for proposed method varies from 0.7648 to 0.8759 and the mean value is 0.8378, which is highest among the compared methods. This shows that image enhanced by proposed method has better structural similarity with original image. The proposed method outperforms the other two methods for all the five performance measures. The box and whisker plot of five performance measures for the proposed method, CLAHE method and HECVO method are shown in Figure 2. The variability and distribution of performance measures calculated for CT image data set of proposed method are compared with other methods. From figure 2, it is clear that the ranges of all the performance measures for proposed method are narrow and variability from minimum to maximum value is quite less for the proposed method in comparison to other methods. This shows that the proposed method produces enhancement results that are stable for all CT images.

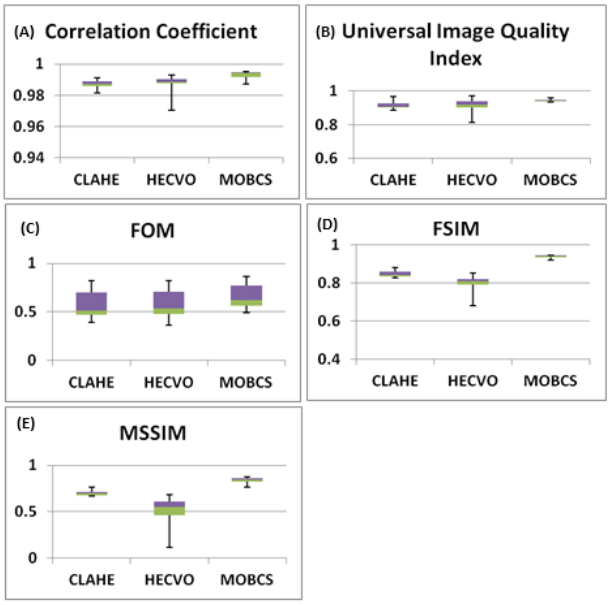

Figure 2. Box plot for comparison of performance measures results of proposed method with CLAHE and HECVO method. Plots (A), (B), (C), (D) and (E) show comparison of correlation coefficient, universal image quality index, figure of merit, feature similarity index and mean structural similarity index respectively

In figure 2, plots (A), (B), (C), (D) and (E) show the comparison of correlation coefficients, universal image quality index, figure of merit, feature similarity index and mean structural similarity index respectively

for the three methods. Figure 3 shows the original images with their corresponding enhanced image results obtained by the proposed method.

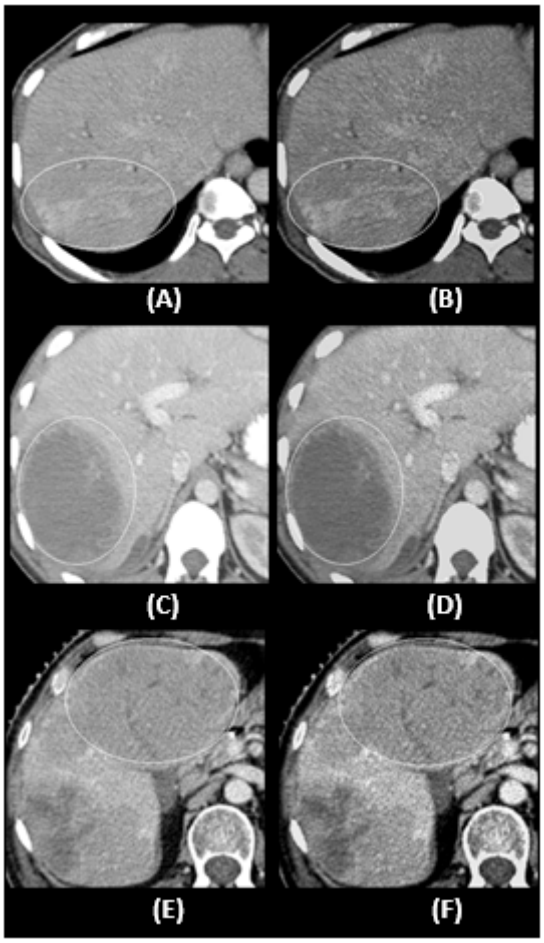

Figure 3. Image enhancement results by proposed method. Images (A), (C) and (E) are the original images with tumor and images (B), (D) and (F), are the corresponding enhanced images.

In Figure 3, images (A), (C), (E), are the original CT images of a patient suffering from liver cancer and the cancerous part is marked by white circular marker and images (B), (D), (F), are the corresponding enhanced images. Images (A) and (B), in Figure 3 contain HCC lesion and images (C), (D), (E) and (F) contain metastasis. The tumor part is clearly visible in the enhanced images and it is easier to differentiate between normal texture and tumor part in the enhanced images. The liver texture part of original image and enhanced image is shown in figure 4, where images (A) and (C) are the original images and images (B) and (D) are the corresponding enhanced images. From figure 4, texture enhancement is clearly visible.

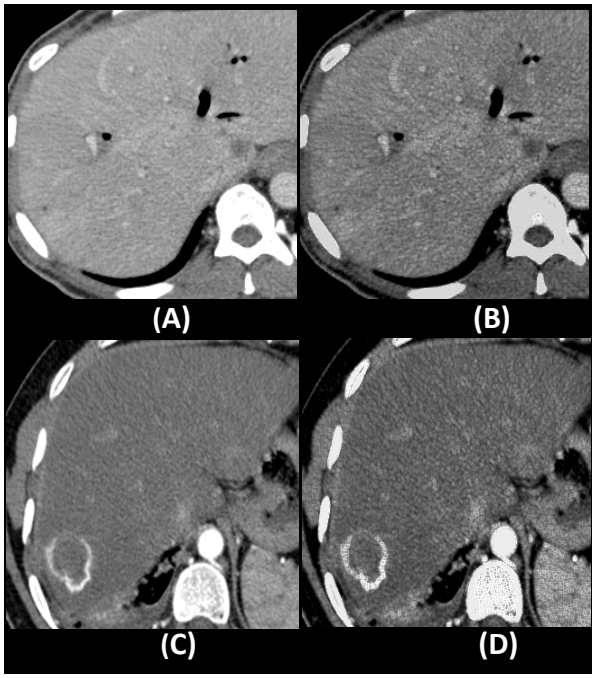

Figure 4. Comparison of texture of enhanced images with original images. Images (A) and (C) are original image and, images (B) and (D) are enhanced images.

The enhanced results obtained by varying the parameters i.e., gradient threshold G_t, stopping condition for region merging δ_t, threshold for contrast stretching λ, mean percentage α. Many experiments have been conducted to obtain the ideal values of parameters that can serve as the desired enhancement of texture of CT images. To accomplish this, first experiment is carried out by varying the gradient threshold G_t and it is tuned to 0.015 times of the estimated standard deviation of noise σ_e. The second experiment is conducted to obtain stopping condition δ_t for region merging. δ_t is varied to suppress the over enhancement and tuned to 5 times of σ_e for best enhanced results. Third experiment is done for λ, it is varied to obtain the required contrast enhancement of texture part. λ equal to 0.8 is the optimal observed value for enhancement. The values less than 0.8 give less contrast enhancement and values higher than 0.8 result in over enhancement. Final experiment is conducted to find the optimal value for mean percentage α. The mean percentage constant α is varied between 10% to 50% and tuned to 30% to preserve global look and textural details of the enhanced image.

4 Conclusion

Objective of this paper is to develop an enhancement method that aids in the enhancement of textural details of CT images. Enhancement of CT images is required to easily diagnose the infection, lesion or tumor. The proposed MOBCS method enhances the textural features and details of CT images effectively with preservation of the global outlook of the image. Performance of the proposed method is evaluated by various quantitative measures. The quantitative performance measures are compared with CLAHE and HECVO method and according to the results, it is observed that MOBCS outperforms other methods in terms of (i) edges preservation, (ii) distortion produced due enhancement and (iii) preservation of

structural similarity of enhanced image with original image. Therefore, it can be concluded that the textural detail enhancement by MOBCS method is quite efficient for better disease diagnosis.

ACKNOWLEDGMENT

The authors thank to Max Saket Hospital, New Delhi for supporting the research.

REFERENCES

[1] D. Mittal, V. Kumar, S. C. Saxena, N. Khandelwal and N. Kalra. Neural network based focal liver lesion diagnosis using ultrasound images. Computerized Medical Imaging and Graphics 2011; 35:315–323.

[2] A. Krishan and D. Mittal, 2015. Detection and Classification of Liver Cancer using CT Images. International Journal on Recent Technologies in Mechanical and Electrical Engineering 2, 93-98.

[3] Ritambhara and D. Mittal, 2015. Segmentation of Liver from Abdomen CT images and 3D Visualization. Journal of Biomedical Engineering and Medical Imaging 2, 46-55.

[4] R.C. Gonzalez, R.E. Woods. Digital Image Processing, 3rd edition. Prentice Hall, 2002.

[5] H. Zhu, F.H.Y. Chan, F.K. Lam. Image contrast enhancement by constrained local histogram equalization. Computer vision and image understanding 1999; 73:281-290.

[6] H.D. Chang and X.J. Shi. A simple and effective histogram equalization approach to image enhancement. Digital signal processing 2004; 14:158-170.

[7] D.Y. Tsai, N. Takahashi, and Y. Lee. An Adaptive Enhancement Algorithm for CT Brain Images. IEEE proceedings, Engineering in Medicine and Biology 27th Annual Conference 2005.

[8] I. Jafar and H. Ying. Image contrast enhancement by constrained variable histogram equalization. IEEE IET proceedings 2007; 120-125.

[9] M. Sundaram, K.Ramar, N. Arumugam and G. Prabin. Histogram modified local contrast enhancement for mammogram images. Applied soft computing 2011; 11:5809-5816.

[10] T. L. Tan, K. S Sim, C. P. Tso and A. K. Chong. Contrast Enhancement of Computed Tomography Images by Adaptive Histogram Equalization-Application for Improved Ischemic Stroke Detection. International Journal of Imaging System Technology 2012; 22:153–160.

[11] Ostojic, D. Starcevic and V. Petrovic. Artifact reduction in multi-scale contrast enhancement for digital radiography. 22nd Telecommunications forum TELFOR 2014; 513:516.

[12] K. Sharma and D. Mittal. Contrast enhancement technique for CT images. Journal of biomedical engineering and medical imaging 2015; 2:44-50.

[13] J. J. Wang, Z. H. Jia, X. Z. Qin, J. Yang and N. Kasabov. Medical Image Enhancement Algorithm Based on NSCT and the Improved Fuzzy Contrast. International Journal of Imaging Systems and Technology 2015; 25:7-14.

[14] Z. Al-Ameen and G. Sulong. A New Algorithm for Improving the Low Contrast of Computed Tomography Images Using Tuned Brightness Controlled Single-Scale Retinex. Scanning 2015; 37:116-125.

[15] B. Xu, Y. Zhuang, H. Tang, and L. Zhang. Object based multilevel contrast stretching for image enhancement. IEEE transactions on consumer electronics 2010; 56:1746-1754.

[16] K. Haris, S.N. Efstratiadis, N. Maglaveras and A.K. Katsaggelos. Hybrid image segmentation using watersheds and fast region merging. IEEE Transactions on image processing 1998; 7:1684-1699.

[17] X. C. He, R. H. Y Chung and N. H. C. Yung. Watershed segmentation with boundary curvature ratio based merging criterion. Proceedings of IASTED International Conference on Signal and Image Processing 2007; 7-12.

[18] T. Brox, D. Farin, P. H. N. de With. Multi-stage region merging for image segmentation. Symposium on Information and Communication Theory in the Benelux 2001; 189-196.

[19] S. Olsen. Estimation of noise in images: An evaluation. CVGIP: Graph. Models Image Process 1993; 55:319–323.

[20] Majumder and S. Irani. Perception Based Contrast Enhancement of Images. ACM Transactions on Applied Perception 2007; 4:1-22.

[21] J. H. Ward. Hierarchical grouping to optimize an objective function. Journal of American Statistical Association 1963; 58:236–245.

[22] D. Mittal, V. Kumar, S. C. Saxena, N. Khandelwal and N. Kalra. Enhancement of ultrasound images by modified anisotropic diffusion method. Medical and Biological Engineering and Computing 2010; 48:1281–1291.

[23] Z. Wang and A. C. Bovik. A universal image quality index. IEEE signal processing letters 2002; 9:81-84.

[24] E. Abdou and W. K. Pratt. Quantitative design and evaluation of enhancement/ thresholding edge detectors. Proceedings of the IEEE 1979; 67:753-763.

[25] L. Zhanga, Lei Zhang, X. Mou and D. Zhang. FSIM: A Feature Similarity Index for Image Quality Assessment. IEEE transactions on Image Processing 2011; 20:2378 – 2386.

[26] Z. Wang, A. C. Bovik, H. R. Sheikh and E. P. Simoncelli. Image Quality Assessment: From Error Visibility to Structural Similarity. IEEE Transactions on Image Processing 2004; 13:1-14.

